A Perspective on Perovskite Solar Cells

Saikat Bhaumik, Sudip K. Saha, and Arup K. Rath

1 Introduction

1.1 Global Energy Crisis

Global energy demand rises by 1.3% each year, and the empirical evidence points toward a steady increase in energy consumption until the year 2040 (International Energy Agency 2019). Almost one billion of the global population still do not have access to electricity, highlighting the need for additional energy. Electricity drives the modern civilization, and energy security is paramount to the sustainable development and prosperity of the human civilization. The over-reliance on fossil fuel to meet the growing energy demand has contributed in a major way to aggravate the current energy problem. Rapid consumption of fossil fuel severely depleted the global energy reserves and their combustion destroying our environment by pouring the harmful greenhouse gasses into it. To contain the global average temperature to increase below 2 °C rapid cut in greenhouse gasses has been suggested by multiple scientific and environmental forums.

S. Bhaumik (✉)
Institute of Chemical Technology-IndianOil Odisha Campus, Gajapati Nagar, Bhubaneswar 751013, India
e-mail: s.bhaumik@iocb.ictmumbai.edu.in

S. K. Saha
Diamond Harbour Women's University, South 24 Paraganas, Diamond Harbour, West Bengal 743368, India
e-mail: sudipsaha.dhwu@gmail.com

A. K. Rath
CSIR-National Chemical Laboratory, Pune 411008, India
e-mail: ak.rath@ncl.res.in

H. Tyagi et al. (eds.), *New Research Directions in Solar Energy Technologies*,
Energy, Environment, and Sustainability,
https://doi.org/10.1007/978-981-16-0594-9_4

1.2 Renewable Clean Energy Alternatives

The generation of energy from renewable energy sources with a minimum carbon footprint could be a possible way forward to the present energy crisis. Several renewable energy technologies have been explored over the years, among which most common technologies with large-scale production capabilities are wind, hydro, geothermal, biomass, and solar. These energy resources are intermittent, in terms of geographical positioning and duration of availability of the energy sources during a day; however, they can be complimentary to develop smart electricity grid to meet all the energy needs. For example, wind speed varies during a day, or the hydropower resource may not be available in all the places; similarly, solar light is inaccessible during the night time. A smart combination of renewable energy sources together with storage capacity (batteries, fuel production, and pumped-storage hydro) would meet most of the energy demands of our daily life.

Among all renewable energy sources, solar energy is particularly interesting as it provides an inexhaustible and universal source of energy. Annually earth receives around 1×10^9 TWh of solar energy with a typical intensity of around 1000 W/m^2 on the ground. Cumulative global annual energy consumption is merely 0.012% (124,290 TWh) (Morton 2006; https://www.iea.org/reports/world-energy-outlook-2019) of the annual solar irradiance. This is to say that the sun provides the earth with as much energy every hour as human civilization consumes every year. Though solar energy is ubiquitous, the conversion of solar energy to useful electrical energy is not as economical when compared to fossil fuel-based alternatives.

1.3 Solar Cell Technology

A solar cell device absorbs the incident light and converts it to the usable electrical power, known as the photovoltaic effect, discovered by French physicist Edmond Becquerel in 1839. Typically, a semiconductor of appropriate band-gap (E_G) is used in solar cells to absorb solar radiation. Photons having energies higher than E_G are absorbed by the semiconductor to create excited electrons in the conduction band and vacancy of electrons in the valance band. These negative and positive charge carriers are separated and extracted from the solar cells to achieve electrical power. Carrier selective contacts, on either side of the absorber layer, are used for the preferential collection of electron and hole at the terminal electrodes of a solar cell. Solar radiation is a panchromatic one and extends within the broad energy range of 3.5–0.5 eV. The wide bandwidth of the solar spectrum makes it challenging to harness in the solar cell devices. Semiconductor having a specific band-gap E_G is transparent to the photons having energy lower than E_G, which is accounted for transmittance loss in solar cells. Similarly, absorption of high energy photons ($>E_G$) excites the valance band electrons to deep inside the conduction band. The high energy photon releases their excess energy quickly ($\sim 10^{-12}$ s) through the emission

of phonon to reach the conduction band minimum. The loss of the excess energy for the high energy photons ($>E_G$) is known as thermalization loss for the solar cell. Additional losses in a solar cell are emission loss due to spontaneous emission of the photoexcited electron from the conduction band to valance band (Hirst and Ekins-Daukes 2011). Those losses are qualified as intrinsic loss, as they cannot be overcome by device and material optimization in the high-performing solar cells. The fundamental efficiency limit for single-junction solar cells is limited to 33.7%, formulated in 1961 by Shockley and Queisser (Shockley and Queisser 1961). The first actual solar cell was developed in 1954 at Bell laboratories using the silicon semiconductor to show the photoconversion efficiency of 6%. Over the last 60 years, research and development have pushed the PCE of silicon solar cells to record 26.7% (Yoshikawa et al. 2017), very close to its theoretical limit of 29% (Andreani et al. 2018). The silicon solar cell technology is already a proven technology with more than 90% accumulated share in the PV market (Andreani et al. 2018).

1.4 The Emergence of Perovskite Solar Cells (PSCs)

In last ten years, the organic–inorganic hybrid perovskite solar cells (PSCs) have emerged as a potential alternative to the existing photovoltaic technologies as their efficiency has improved from 3.8% in 2009 to 25.1% in 2019 as shown in Fig. 1 (Kojima et al. 2009; NREL solar energy chart: https://www.nrel.gov/pv/assets/pdfs/pv-efficiency-chart 2019). The unprecedented growth of the PSCs is associated with the fact that the perovskite materials can be synthesized from low-cost solution

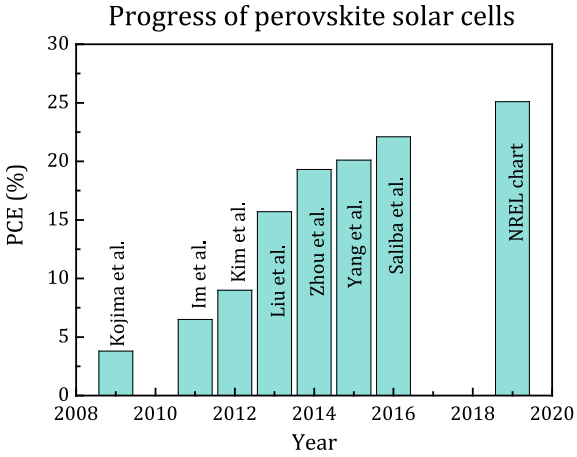

Fig. 1 Graphical representation of progress of PSCs (Kim et al. 2012; Yang et al. 2015a; Kojima et al. 2009; NREL solar energy chart: https://www.nrel.gov/pv/assets/pdfs/pv-efficiency-chart 2019; Im et al. 2013; Zhou et al. 2014b; Liu and Kelly 2014; Saliba et al. 2016a)

processing and can be made crystalline below 200 °C, promising for the cost competitiveness of the disruptive solar cell technology (Green et al. 2014; Zuo et al. 2016). The band-gap of the perovskite semiconductors can be tunable for a range of 2.2–1.2 eV through composition engineering. Hybrid perovskite systems possess the direct band-gap with the strong absorption coefficient ($>10^4$ cm^{-1}), which requires only 1-μm-thick perovskite layer to absorb the full solar radiation above their band-gap. Long-range crystallinity of solution-processed perovskite layer contributes significantly to achieve high carrier mobility (1–30 cm^2 V^{-1} S^{-1}) and long carrier lifetime (~100 ns) in their solid films (Johnston and Herz 2016). The carrier diffusion length in PSCs exceeds 10 μm as a result (Tainter et al. 2019), allowing efficient extraction of photogenerated carriers in solar cells. The aforementioned traits make hybrid perovskites unique for the solar cells (Grätzel 2014) as well as other optoelectronic applications, like light-emitting diodes (Tan et al. 2014; Zhang et al. 2017a), lasers (Chen et al. 2016a; Stylianakis et al. 2019), and photodetectors, (Hu et al. 2014a; Wang and Kim 2017).

Despite several advancements, there are concerns over the stability of the perovskite materials (Wang et al. 2019), which hinders their prospect for commercialization. The organic–inorganic hybrid perovskite materials suffer from poor stability when exposed to heat, oxygen, moisture, and even illumination (Lee et al. 2015a; Smecca et al. 2016; Aristidou et al. 2015). The instability of perovskite materials lies with the fact that the perovskite crystals are ionic, and there exits significant empty space within the perovskite unit cells which makes them soft crystals and the volatile nature of the organic component in the perovskite crystal. Significant progress has been made to improve the stability of perovskite semiconductor through compositional engineering to minimize the crystal strain, tuning the unit cell toward cubic structure, and replacement of the volatile component (Wang et al. 2019; Asghar et al. 2017). Development of the two-dimensionally confined perovskite layer, interlinked by long-chain organic molecules has been investigated to reduce the moisture induce degradation of the perovskite layer (Grancini et al. 2017; Tsai et al. 2016). However, the special confinement and insulating ligands have a detrimental effect on charge transport. Nevertheless, it is an interesting approach to improve the stability of perovskite semiconductors.

In this book chapter, a detailed overview of PSCs will be discussed. Progress in synthesis strategies in terms of composition engineering and structure–property correlation to attain the high photovoltaic efficiency will be explained. The evolution of device engineering for the PSCs to attain high photovoltaic efficiency and better stability will be summarized.

2 Intrinsic Properties of Perovskites

2.1 Structural Properties

Metal halide perovskites are known as the common cluster of compounds with general chemical formula of AMX_3, where A is organic or inorganic cations (typically $MA = CH_3NH_3^+$, $FA = HC(NH_2)_2^+$, Cs^+, K^+, Rb^+, etc.), M is metal cations (Pb^{2+}, Sn^{2+}, Eu^{2+}, Ge^+, etc.), and X is halide anions (Cl^-, Br^-, I^-) (Kojima et al. 2009; NREL solar energy chart: https://www.nrel.gov/pv/assets/pdfs/pv-efficiency-chart 2019; Sum and Mathews 2014). In a perovskite unit cell, A cation is situated at the eight corners of the cube, while M-cation is placed at the body center and six numbers of X anions are located at the face centers. AMX_3 belongs to an extended large family of organic–inorganic metal halide perovskites where the $[MX_6]^{4-}$ octahedra can grow three-dimensional (3D), two-dimensional (2D), one-dimensional (1D), or zero-dimensional (0D) crystal structures having the same unit cell as shown in Fig. 2. For example, in $MAPbI_3$ each $[PbI_6]^{4-}$ octahedra is connected with six

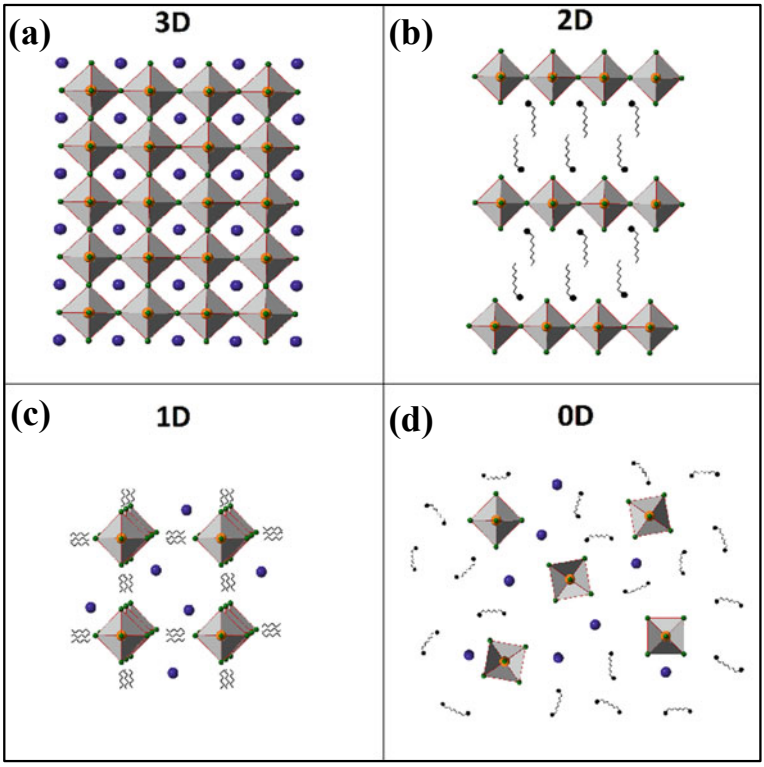

Fig. 2 Schematic representation of **a** 3D, **b** 2D, **c** 1D, and **d** 0D perovskite crystal structure, respectively

neighbors of iodide forming a 3D network while MA^+ is located at the void of the network (see Fig. 2a). In other words, the $[PbI_6]^{4-}$ octahedras are connected three dimensionally in the crystal structure. For the 2D case (see Fig. 2b), longer organic cations like $CH_3(CH_2)_nNH_3^+$ situated at *A*-site where each $[PbI_6]^{4-}$ octahedron is connected with four neighbors iodide anions, forming a 2D network layer that is sandwiched between two $CH_3(CH_2)_nNH_3^+$ layers and the chemical formula becomes A_2PbI_4. It results in multiple quantum well structures from the stacking of these sandwiched layers via van der Waals interaction with the $CH_3(CH_2)_nNH_3^+$ layer as the barrier. In 1D case (see Fig. 2c), each octahedra is attached to two opposite corners with neighboring octrahedras and forming parallel infinite chains (e.g., $(C_{10}H_{21}NH_3)_2PbI_4$). Lastly, for 0D structure (e.g., Cs_4PbI_6), each $[PbI_6]^{4-}$ octrahedra is separated by four Cs^+ ions to form an isolated molecule resembles to a quantum dot array (see Fig. 2d).

The lead halide perovskite structure (AMX_3), in which *A*-site cation, plays a very important role for formation of stable perovskite crystal structure (Park and Seok 2019; Correa-Baena et al. 2017). The stability parameter is characterized the Goldschmidt tolerance factor (t),

$$t = \frac{(r_A + r_X)}{\sqrt{2} \times (r_M + r_X)}$$

where r_A, r_M, and r_X are the ionic radii of the *A*-site cation, metal cation, and halide, anions, respectively. For an example, the ionic radii of I^- and Pb^{2+} ions are 2.03 Å (r_X) and 1.33 Å (r_M), respectively, as represented in Fig. 3, and the radii of *A*-site cation is in the range of 2.3–2.8 Å (r_A). When the perovskite is formed using Cs^+, MA^+, or FA^+ as the *A*-site cations, the optical properties of the perovskites change with the cation result in a red-shifting absorbance onset. In other words, band-gap of the perovskite material changes in this order, MA^+ (1.55 eV) < Cs^+ (1.5 eV) < FA^+ (1.45 eV). However, the volume per $APbI_3$ unit changes from 222, 248, and 256 $Å^3$ for Cs^+, MA^+, and FA^+ cations, respectively. Thus, Cs^+ and MA^+ differ significantly in radial size, but the band-gap changes a little compared to difference between the MA^+ and FA^+ cations.

Halide substitution. The advantage of these metal halide lead halide perovskites is the capability to tune their optoelectronic properties by substitution the halide ions. For an example, the iodine ions in $MAPbI_3$ perovskite structure can be substituted with both Cl^- and Br^- anions (Correa-Baena et al. 2017). Same substitution of the ions can be possible for $MAPbBr_3$ and $MAPbCl_3$ perovskite structures. While halide substitution, the band-gap of the perovskites changes 2.97, 2.24, and 1.53 eV for the $MAPbCl_3$, $MAPbBr_3$, and $MAPbI_3$ perovskite, respectively. At room temperature, $MAPbCl_3$ and $MAPbBr_3$ perovskites are found to be in a cubic structure while the phase changes to a tetragonal structure at lower temperatures. Moreover, $MAPbI_3$ crystallizes to tetragonal crystal structure, whereas $FAPbI_3$ crystallizes to hexagonal δ-phase or cubic α-phase at room temperature as shown in Fig. 4.

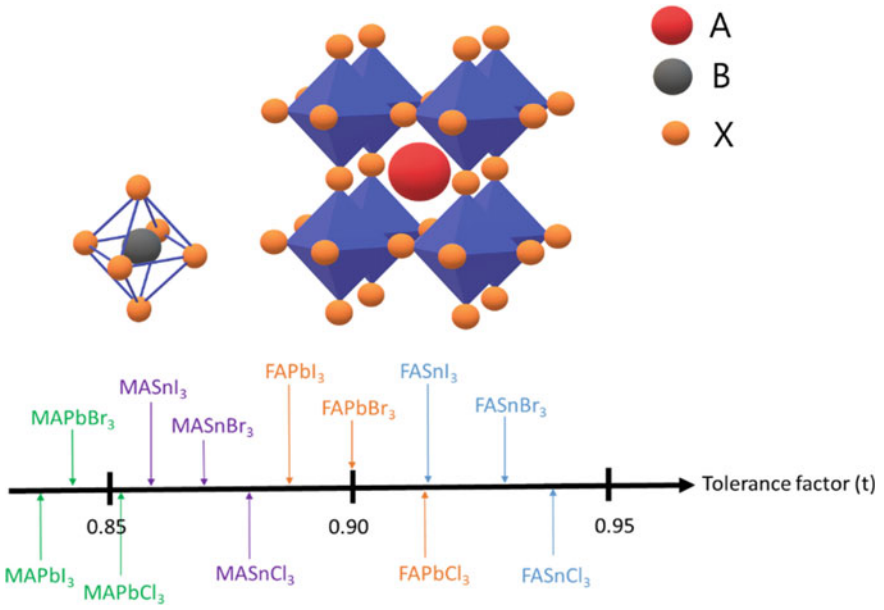

Fig. 3 Tolerance factor of ABX_3 perovskites with the various compositions of A, B, and X-sites

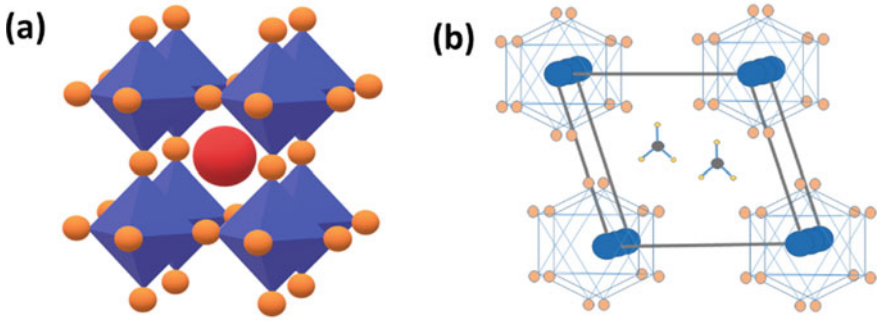

Fig. 4 Crystal structure of **a** cubic α-phase and **b** hexagonal δ-phase of perovskites

Organic cation substitution. Similar to halide substitution, organic cations can also be replaced in the perovskites (Correa-Baena et al. 2017). For an example, MA^+ cations can be exchanged with slightly bigger sized FA^+ cations. The cation exchange in perovskites has very small impact on the optical band-gap or very little change in band-gap observed. DFT computations demonstrate that organic cations do not contribute to the electronic states close to the band edges. However, with cation exchange the crystal lattices changes which results in a slight change in the band-gap.

Organic/inorganic ion mixing. Simultaneous exchange of both organic cations and anions has been done as well. For an example, the performance of $MAPbI_3$ perovskite-based solar cells is not highly efficient (Correa-Baena et al. 2017). On the other hand, $FAPbI_3$ and $CsPbI_3$ perovskite structures (cubic phase) are not stable at room temperature. However, the compositional mixing of MA/FA/Cs/Br/I perovskites has been studied enormously. $FAPbI_3$ perovskite-based photovoltaics appears to give better device performance over $MAPbI_3$, but some MA^+ cations in $FAPbI_3$ perovskites stabilizes the perovskite structure. Introducing Br^- anions in $FAPbI_3$ perovskites allows to tune the band-gap, enhance structural stability, and improve the device performance. Therefore, it is very important to design principle to mix cations and halides to achieve final perovskite compositions that is advantageous while evading their disadvantages.

2.2 *Electronic Structure*

Perovskite is known for the common cluster of compounds with general chemical formula. The electronic band structures of organic–inorganic perovskites can be calculated by using a semiempirical technique based on the extended Huckel theory and an ab initio method based on the Hartree–Fock theory (Sum and Mathews 2014). Another approach is using ultraviolet photoelectron spectroscopy and first principles density functional theory (DFT) band calculations at the room temperature. DFT calculations for 3D $MAPbI_3$ perovskite crystals reveal that the valence band maxima contain Pb 6p–*I* 5p σ antibonding orbital, while the conduction band minima comprise of Pb 6p–*I* 5s σ antibonding and Pb 6p–*I* 5p π antibonding orbitals as represented in Fig. 5. Nevertheless, DFT calculations also show that the A-site cation has a very little influence on the band-gap energy, of which is mainly determined by the $[PbI_4]^{6-}$ network.

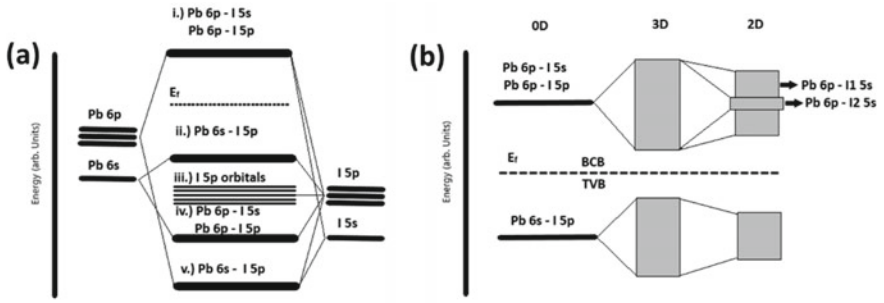

Fig. 5 Bonding energy diagram of **a** $[PbI_4]^{6-}$ cluster, **b** 0D, 3D, 2D band structure of $MAPbI_3$ perovskites

Absorption coefficient. The absorption coefficient of materials is described as the amount of a given color of light is absorbed by the material for a given thickness. Thats means that more light absorbs by a material then its absorption coefficient will be higher. The absorption coefficient is represented by the Greek letter "α". It has units of cm^{-1} because it defines the amount of light absorbed per unit thickness of the material. Since the material absorbance varies with the wavelength of the light, so the absorption coefficient is a function of wavelength/color. For an example, the absorption coefficient of $MAPbI_3$ thin films is around 1.5×10^4 cm^{-1} at 550 nm, that gives the penetration depth is only 0.66 mm for 550 nm light. However, for 700 nm light, the absorption coefficient of $MAPbI_3$ thin films is around 0.5×10^4 cm^{-1} and corresponding penetration depth is around 2 mm (Park 2015). Higher penetration depths led to more incoming light can be absorbed by the perovskite films, which is essential for high-efficiency PSCs.

Balanced charge transport behaviors. The charge transport properties of $MAPbX_3$ perovskites were reported by Xing et al. (2013) and Stranks et al. (2013). Transient spectroscopic analysis reveals that upon absorbing the light perovskites exhibited balanced electron- and hole-transporting behavior. The calculated electron diffusion length for $MAPbI_3$ thin film is around 130 nm while the hole diffusion length is calculated to 100 nm (Xing et al. 2013). However, by doping Cl^- ions in $MAPbI_3$ perovskite, the electron and hole diffusion length enhanced to 1069 nm and 1213 nm, respectively (Stranks et al. 2013). The longer and balanced charge diffusion lengths results in improved solar cells device performance.

3 Perovskite Structure Formation Techniques

3.1 Single Crystals (SCs)

Solution temperature-lowering (STL) method. In this method, the solubility of the lead halide perovskites in acid halide solvents (e.g., HI, HBr, HCl) plays an important role for perovskite crystal growth. The perovskite materials solubility changes significantly with temperature. This mechanism is generally used for perovskite SCs growth. At first perovskite, seed crystals are dipped into an acid halide solvent at certain temperature (see Fig. 6a). Upon lowering the temperature, the saturation of the solute in the solvent takes place and corresponding crystal growth start around the perovskite seed crystals. High-quality $MAPbI_3$ SCs can be grown by this temperature-lowering process. In a glass beaker, $MAPbI_3$ seed crystals are spanned by a stirrer in HI solvent at 65 °C (Dang et al. 2015). By lowering the temperature to 40 °C, saturation of perovskites solute in the HI solvent expedite the crystal formation and finally 10 mm × 10 mm × 8 mm-sized $MAPbI_3$ SCs. These as-synthesized SCs exhibit two natural facets in the directions of (100) and (112) crystal planes. The advantages of this method are that the crystal growths are easily controlled with temperature and high-quality large-size SCs can be obtained.

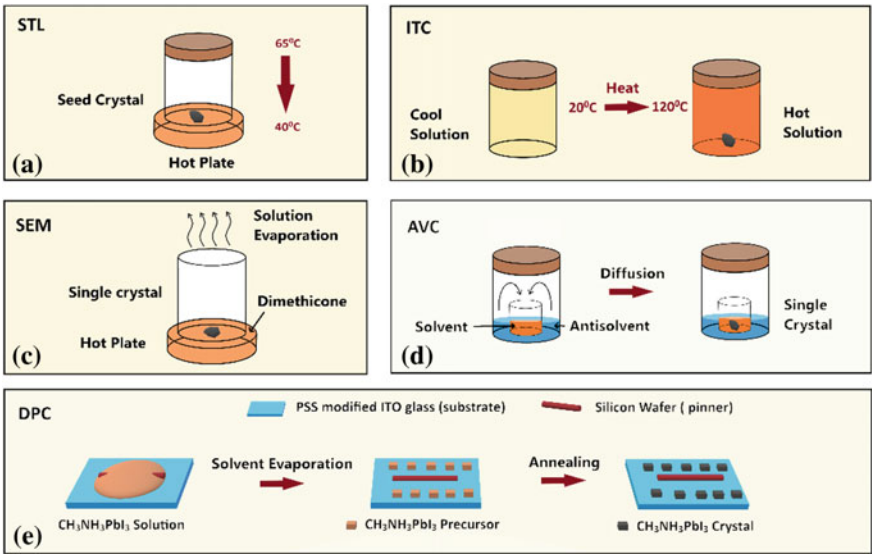

Fig. 6 Schematic illustration of growth of $MAPbI_3$ perovskite single crystals via various synthetic methods as **a** STL, **b** ITC, **c** AVC, **d** SEM, and **e** DPC method, respectively

Inverse temperature crystallization (ITC) method. The ITC crystal growth mechanism is totally opposite to the temperature-lowering method. The perovskite materials whose solubility in a particular solvent are decreasing with increasing the temperature. Several research groups investigated the lead halide perovskites solubility in *N*, *N*-dimethylformamide (DMF), dimethylsulfoxide (DMSO), and γ-butyrolactone (GBL). Interestingly, in these solvents the perovskite crystal structure formation was observed with increase of solution temperature. By this ITC method, mm-sized $MAPbX_3$ and $FAPbX_3$ ($X = Cl^-$, Br^-, I^-) SCs were obtained via using different organic solvents (Saidaminov et al. 2015; Liu et al. 2015a).

Basically, in the solvent mixture organic solvents such as DMF and DMSO are connected with lead halides and form intermediate adducts. The perovskite SCs can be developed by removing the organic solvents at higher temperature (see Fig. 6b). For example, when MAI and PbI_2 are mixed in DMF, an intermediate $MAPbI_3$-DMF adduct phase is formed due to a strong interaction of DMF–MA bonding. In a similar way, $MAPbI_3$-DMSO adduct phase is formed due to the interaction of DMSO–PbI_2 bonding, when MAI and PbI_2 are mixed in DMSO. The $MAPbI_3$ single crystal was obtained by removing the DMF or DMSO solvent via annealing.

Anti-solvent vapor-assisted crystallization (AVC) method. The AVC method is used to grow the perovskite crystals that are highly soluble in a solvent but have very poor solubility in other solvent (Shi et al. 2015). By this method, mm-sized $MAPbX_3$ SCs were obtained by using the anti-solvent dichloromethane (DCM), that is slowly diffused into the solution containing MAX and PbX_2 ($X = Br^-$, I^-) dissolved in DMF or GBA solvents (see Fig. 6c). This growth method for preparation

of the hybrid halide perovskites SCs are highly efficient and applicable. However, it is difficult to develop large-size SCs that is important for large-area optoelectronic device applications.

Slow evaporation method (SEM). This slow evaporation method is a traditional and easy solution-based process for growth of SCs. Liao et al. (2015) have prepared the SCs of hybrid perovskite analogue $(benzylammonium)_2PbX_4$ ($X = Cl^-$, Br^-). In this process, stoichiometric mixture of benzylammonium chloride and $PbCl_2$ was mixed in concentrated HCl aqueous solution. Bulk $(benzylammonium)_2PbX_4$ crystals with the dimensions of 5 mm × 10 mm × 2 mm were obtained via the slow evaporation of DMF solution at 90 °C (see Fig. 6d). The preferred growth of single crystalline planes is extended along the [001] direction. Although this process is highly efficient, sometimes this method is hard to control precisely, that limits the industrial applications.

Droplet-pinned crystallization (DPC) method. Micrometer-sized $MAPbI_3$ single crystalline arrays can be formed using this DPC method (Jiang and Kloc 2013). At first, $MAPbI_3$ precursor solution was drop-casted on PEDOT:PSS-coated indium tin oxide (ITO) glass substrate, on which smaller wafers were placed (see Fig. 6e). Upon annealing, the precursor solvent was evaporated and rectangular-shaped $MAPbI_3$ SCs arrays were formed within some minutes. This method is very useful for growth of micrometer-sized SCs. It also provides a platform to grow single crystalline thin films.

3.2 Thin Films

Perovskites thin films are usually grown using solution process and vapor-phase deposition techniques. Very careful control on several processing parameters, such as the perovskite film thickness, crystallinity, perovskite phase purity, and perovskite film morphology, plays a significant role in achieving high-quality perovskite thin films and corresponding final device performance. The optimized perovskite thin-film processing steps can lead to desired perovskite thin-film thickness, highly crystalline films, uniform morphology, bigger crystal sizes, and less defect states. For solution-processed perovskite thin films, the processing parameters are types of perovskite precursors and solvent mixtures, precursor solubility, spin-coating speed, solvent engineering steps, types of anti-solvents, volume of the anti-solvent, time of anti-solvent injection, post-film thermal annealing temperature and time.

Single-step solution deposition. It is the simplest way to prepare a perovskite thin film via solution-processed spin-coating method. This perovskite thin films formation depends on various components, like substrate on which perovskite film will be deposited, precursors, solvents/mixed solvent and followed by spin-coating parameters. After spin coating, the semiconducting thin film is further annealed for faster crystallization process. The final film crystallinity, thickness, and morphology depend

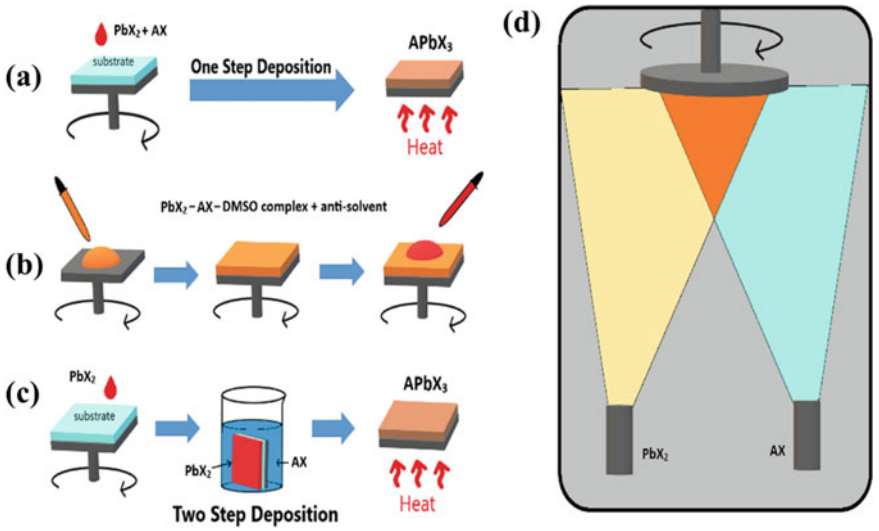

Fig. 7 Schematic illustration of formation of $MAPbI_3$ perovskite thin films via **a** one-step solution deposition process, **b** solvent engineering process, **c** two-step deposition process, and **d** vacuum processing technique, as mentioned in the diagram

on various processing parameters. Single-step perovskite films formation was first introduced by Im et al. in 2011 (Im et al. 2013). In this process, they prepared a precursor solution by mixing an equimolar MAI and PbI_2 powders in γ-butyrolactone (GBL) solvent at 60 °C for 12 h under vigorous stirring. Then the mixed solution was filtered through a 0.45 mm size PVDF filter for final thin-film formation via spin coating (see Fig. 7a). Then they spin-coated the precursor concentrations are in various concentrations of 10.05, 20.13, 30.18, 40.26 to 41.22 wt%. They observed that mesoporous TiO_2 films are better than compact films of TiO_2 for growth of thick uniform perovskite films. On the top of mesoporous TiO_2 film, the precursor solution was dropped and waits for one min to penetrate the solution into a mesoporous TiO_2 layer, which was then spin-coated at 2000 rpm for 40 s in an ambient atmosphere. The spin-coated $MAPbI_3$ film was annealed at different temperatures, and tetragonal crystal structure was formed. With increasing the concentration of the perovskite precursor, the film formation abruptly changes. A yellow-colored perovskite film was obtained for 10.05 wt% of precursor concentration, while it transformed to black color when the wt% concentration increased to 40.26 wt%. The color change of perovskite thin films at different precursor concentrations is ascribed due to higher perovskite precursor concentrations led to enhanced precursor interaction upon annealing and corresponding formation of the black perovskite phase. The UV-vis absorption spectra of films prepared from different concentrations of the perovskite precursor showed an increase in light absorption with higher precursor concentrations. It is also observed that up on annealing from temperature 40–100 °C,

the perovskite film led to an increase in the absorption intensity, however, beyond 100 °C the absorption intensity decreases.

Selection of mixed solvents to dissolve perovskite precursors is also very important for formation of smooth perovskite surface with uniform crystal domains (Kim et al. 2014a). A mixed precursor solution of DMF and GBL was used to dissolve MAI and PbI_2 at 60 °C inside a nitrogen glovebox. The morphology of spin-coated perovskite films hugely differs when the films when spin-coated from different solvents like only DMF, only GBL, and mixed DMF and GBL solvents. The perovskite films formed from GBL solvents show formation of larger crystal grains with poor surface coverage. However, the perovskite films prepared from DMF show an improved morphology but non-uniform crystal dimensions. When the perovskite films developed from mixed solvent of DMF:GBL, the films display a smooth surface morphology with denser packing having uniform crystal dimension of 100 nm. The root-mean-square (RMS) roughness of the perovskite thin film reduces to 6.6 nm (for DMF:GBL) from 24.53 nm (for GBL) and 8.88 nm (for DMF). The crystallization process of perovskites varies from different solvents to solvents due to different evaporation rate of each solvent during spin-coating process. A higher evaporation rate of a solvent could lead to irregular thin-film surface morphology while mixture of different solvents may increase precursor solubility and controls the evaporation rate and resulted in an uniform and compact perovskite film.

Solvent engineering approach. This method is slightly modified compared to conventional single-step solution deposition process where some volume of an anti-solvent is drop-casted on top of perovskite film during spin coating of the perovskite precursor (see Fig. 7b). This solvent engineering process for perovskite preparation was first introduced by Jeon et al. in 2014 (Jeon et al. 2014). Usually, perovskite precursors are dissolved in a mixed solvent of GBL and DMSO. An anti-solvent that does not dissolve the perovskite but is miscible with GBL and DMSO, such as toluene, chlorobenzene, and chloroform, was dropped during the spin coating to facilitate an intermediate complex (MAI–PbI_2–DMSO) film and reduces the growth kinetic for perovskite crystallization process. The intermediate phase is confirmed by X-ray diffraction (XRD) and Fourier-transform infrared spectroscopy (FTIR) analysis (Beckmann 2010). This intermediate thin film was finally annealed at 130 °C and fully converted into perovskite phase. The resulted films are very uniform, dense, and smooth over larger active area.

Two-step deposition: Two-step deposition or sequential deposition technique, in which individual precursor layers, is deposited separately and interacts together to develop a final perovskite thin film (Burschka et al. 2013). At first, lead halide films are grown on the substrate via spin coating and later this film is dipped in MAI in IPA solution, leading to formation of $MAPbI_3$ perovskite thin films (see Fig. 7c). The precursor PbI_2 dissolved in DMF solvent and the solution was spin-coated on top of a mesoporous TiO_2 layer, followed by annealing at 70 °C to form yellow-colored PbI_2 film. This film was then dipped in a 5–10 mg/ml MAI precursor in IPA for several seconds of time, followed by rinsing in IPA and annealing at 70 °C. The yellow PbI_2 films transformed into black-colored films confirmed the formation of

the perovskite phase. The thin-film morphology greatly depends on MAI solvent concentration and dipping time. This procedure is very useful for large-area device fabrication with reproducible high-quality crystalline perovskite film and excellent photovoltaic device performance.

Vacuum processing technique. In vapor deposited technique, the perovskite precursor powders MAI and $PbCl_2$ are placed separately in a thermal boat and simultaneously thermally evaporated on a substrate to form a perovskite film (Liu et al. 2013). Usually, the MAI and $PbCl_2$ precursors were evaporated with a molar ratio of 4:1 in a vacuum of 10^{-5} mbar and resulted in a dark reddish-brown-colored perovskite ($MAPbI_{3-x}Cl_x$) film (see Fig. 7d). The resulted perovskite films show a complete, crystalline, uniform coverage, and larger grain size compared to the conventional solution-processed perovskite. This procedure is also very advantageous for large-area device fabrication.

4 Basic Principle of PSCs

Mainly three key parameters play crucial role for device performance of the PSCs. First, the active perovskite material, the material needs to be designated in such a way that it has optimized band-gap and high-phase stability. However, the band-gap of the perovskites can be tuned in the visible to infrared spectral range by mixing/exchanging the halide anions ($X = Cl^-$, Br^-, I^-) or replacing the cations (MA^+, $C_2H_5NH_3^+$, FA^+, Cs^+, K^+, Rb^+). Second, the surface morphology of the perovskite thin films, uniform top layer, and large crystals formation is very essential for efficient charge transport and good diode characteristics; this is widely governed by precursor/solvent selections and post-processing conditions. Third, selection of proper charge transporting materials and optimizing the energy levels alignment is between the perovskite and the neighboring transport layers in order to enable effective charge transport throughout the device. In this regards, detailed study on the position of conduction band (CB) minimum and valence band (VB) maximum is required for perovskites and transporting materials.

The basic principle of solar cells is to convert the solar energy into electrical energy. The solar energy originates from the Sun, considered as a blackbody with a light spectrum at the temperature of about 5800 K. As the Sunlight passes through the Earth's atmosphere, it is attenuated by light scattering and some part is absorbed via chemical interactions with the atmospheric molecules. The atmosphere absorbs certain wavelengths of light and changing the amount of light reaching the Earth's surface. The water vapor mostly contributes for absorption of Sunlight spectra while molecular nitrogen, oxygen, and carbon dioxide also absorb some parts. The final solar spectrum that reaches to the Earth's surface varies with the light path length covered through the atmosphere. AM 1.5 spectrum with light intensity of 100 mW cm^{-2} are standardized as the measuring conditions for characterization of solar cells (see Fig. 8).

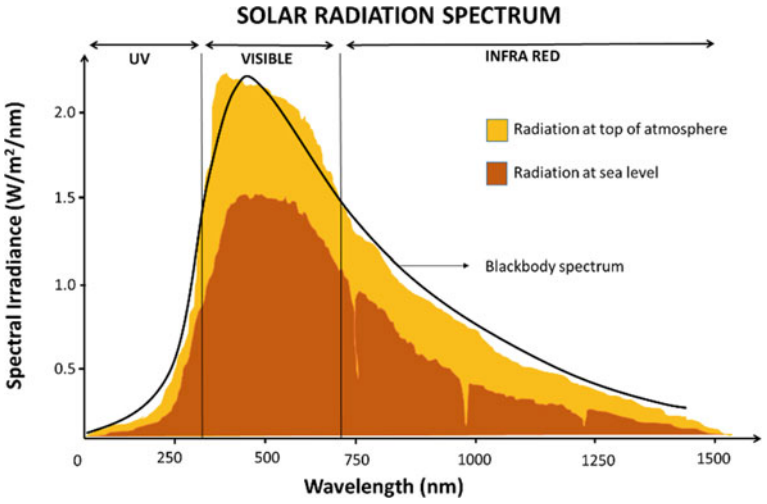

Fig. 8 Spectral power of the AM 1.5 global solar spectrum

4.1 Charge Generation and Transport in Perovskite Materials

For the semiconductor-based photovoltaics, the photons from Sunlight with enough energy can excite the electrons from the valence band to the conduction band across the band-gap and that results in generation of charge carriers. The photogenerated charge carriers can be separated out with proper band alignment of transporting layers such that electrons and holes are moving in opposite directions and store at counter electrodes. This is how solar cells are working under Sunlight. When Sunlight is falling on any absorbing active material, there are two types of loss mechanisms happened that hinder the solar cell efficiency. In a single-junction solar cell, the absorbing material cannot absorb photons having energy less than the band-gap of the active material and the light directly transmit through the material (see Fig. 9a). These low energy photons do not contribute to solar cells device performance. However, the photons having energy higher than the band-gap, absorbed by the active material, and the charge carriers are excited to higher energy states. After a very short time period, these excited charge carries relaxes to band edges of the active material through non-radiative thermalization process (see Fig. 9b). Here the excess energy of the incident photons is losses via this non-radiative process. Finally, the band-gap energy contributes to the device electricity. These two loss mechanisms reduce half of incident solar energy conversion to electrical energy.

Generation of charge carriers. In an ideal semiconductor, the valence and conduction bands are not flat. The band alignment is depending on the *k*-vector in the phase space that describes the momentum of an electron in the semiconductor. So, the energy of an electron is dependent on its momentum because of the periodic crystal structure of the semiconductor. If the maximum energy of the valence band and the

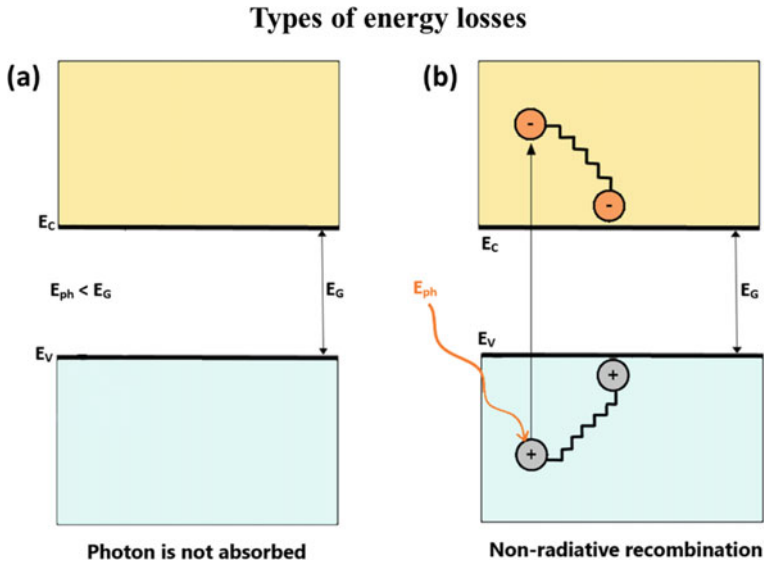

Fig. 9 Schematic representation of two types of energy losses in a solar cell when photon incident on the device. **a** If $E_{ph} < E_G$, the incident photon is not absorbed by the semiconductor. **b** If $E_{ph} > E_G$, a part of photon energy relaxes through thermalization process

minimum energy of the conduction band matches at the same k-vector in the E–k space, an electron can be excited from the valence band to the conduction band without a change in the momentum. Such a semiconductor is called a direct band-gap material. If the maximum energy of the valence band and the minimum energy of the conduction band does not match at same k-vector, so the electron cannot be excited without changing its momentum, such materials are called an indirect band-gap material. The absorption coefficient of a direct band-gap material is much higher than an indirect band-gap material; thus, the absorbing semiconductor can be much thinner for a direct band-gap semiconductor.

In a semiconductor, electrons can only stay at energy levels below the valence band edge (E_v) and above the conduction band edge (E_c). Between these two energy levels no allowed energy states exist for the electrons. Hence, the band-gap energy difference is, $E_g = E_c - E_v$. When the Sunlight with incident photons has energy higher than the band-gap of the semi-conducting material, which are absorbed and subsequently excite electrons from an initial energy level E_i to a higher energy level E_f as shown in Fig. 10a. So, the photons with an energy smaller than E_g incident on the ideal semiconductor, it will not be absorbed by the material. If an electron is excited from E_i energy level to E_f energy level, a void is created at E_i energy level and the void acts like a positive charged particle and is so-called a hole. Therefore, the absorption of a photon leads to formation of an electron–hole pair where electron stays at conduction band and hole stays are at valence band.

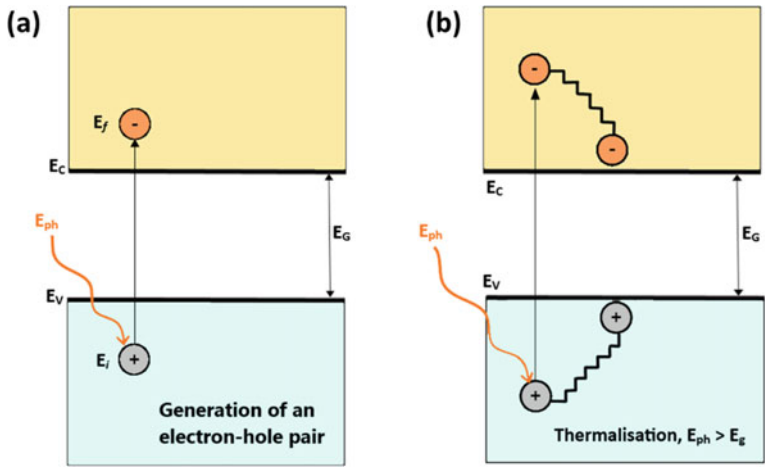

Fig. 10 Schematic representation of **a** absorption of a photon in a semiconductor with band-gap of E_G. The incident photon with energy $E_{ph} = h\gamma$ excites an electron from E_i to E_f in the semiconductor and at E_i a hole is created. **b** If $E_{ph} > E_G$, a part of the energy is thermalized

Separation of the photogenerated charge carriers. The excited electron can stay at the conduction energy level for a very short period of time, which is so-called the lifetime of the electron. The time period is generally in millisecond to microsecond scale. After the lifetime, the electrons will return back to the valence energy level from the conduction energy level and recombine with the holes. The electron–hole recombination energy will be released either as a photon (radiative recombination) or relaxes via lattice vibrations (non-radiative recombination) as shown in Fig. 10b. One can store the energy for further use before the electron–hole recombination process by separating out the electrons and holes via an external circuit and it is so-called solar cells circuit. A solar cell has to be designed such that the electrons and holes can transfer to opposite directions in presence of favorable adjacent energy levels of transporting materials in a very short span of time, i.e., less than the lifetime of the excited electrons. This requirement limits the thickness of the absorber materials.

Collection of the photo-generated charge carriers. Finally, the opposite charge carriers are extracted from the solar cells with electrical contacts and the energy is stored in a battery. Here, the chemical energy of the electron–hole pairs is converted into electrical energy.

4.2 Characterization Processes of PSCs

Power conversion efficiency (PCE). The most important parameter to characterize the solar cells is the PCE, which can be obtained from the current density–voltage

(J–V) characterization. As demonstrated in Fig. 11, under illumination and without external bias, a negative current is flowing through the circuit. The current density under these conditions through the solar cells device is called short-circuit current density (J_{sc}). When a positive bias is applied to the circuit, up to an open-circuit voltage (V_{oc}) a negative current is transporting though the circuit, indicating the power generation by the solar cell. The PCE of a solar cell is defined as the ratio of the maximum power output (P_{out}) to the incident light power (P_{in}), and it is represented by the formula,

$$\mathrm{PCE} = \frac{P_{out}}{P_{in}} = \frac{I_{sc} \times V_{oc} \times \mathrm{FF}}{P_{in}}$$

where the fill factor (FF) can be thought of as the biggest rectangular area (blue area; see Fig. 11) covered under the current voltage curve. It is the quotient of maximum solar power output and the product of V_{oc} and I_{sc}.

External quantum efficiency. Another important parameter to characterize solar cells is the external quantum efficiency (EQE). It is the conversion ratio of the incident photon into electron in a solar cell, which is also known as the incident photon to converted electron (IPCE). The EQE is defined as the ratio of the number of output electrons to the number of incident photons at different wavelengths. EQE of a solar cell is depended on many factors, such as light absorption-co-efficient of the active layer, exciton generation efficiency, exciton dissociation efficiency, and carrier extraction efficiency.

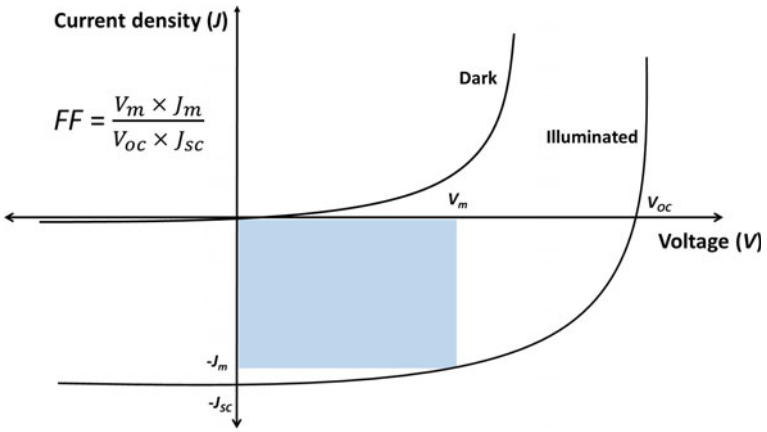

Fig. 11 Schematic representation of J–V characteristics of a solar cell

5 Working Principle of PSCs

5.1 Device Architectures

Selection of the transporting materials with proper band alignment is a crucial part. In PSCs, perovskite layer acted as an absorber layer. Depending upon the electron and hole transport toward light entering electrode, PSCs can be classified into two parts *n-i-p* structure and *p-i-n* structure. One can easily understand this classification by checking the position of transporting layer [*n-i-p*: electron-transporting materials (ETMs) layer placed on top of TCO; and *p-i-n*: hole-transporting materials (HTMs) layer placed on top of TCO]. These two types of solar cells device structures are subclassified into two other parts mainly mesoscopic and planer structure. The mesoscopic structure incorporates a mesoporous layer (in front of light entering window), whereas the planar structure consists of all planar layers of transporting layers. Sometimes PSCs are classified without transporting layers.

Regular *n-i-p* structure. PSCs are often called as solid-state dye sanitized solar cells (SS-DSSCs). PSCs are modified form of conventional DSSC. Here the light absorption was governed by the solid-state perovskite material in DSSCs, and it was fabricated from dyes. Conventional PSCs structure is *n-i-p* (see Fig. 12) type, where the *n*-type metal oxide layer (transporting layer) was deposited on top of the conducting oxide layer. On the top of this *n*-type transporting layer, intrinsic absorber perovskite layer was grown and finally the *p*-type transporting layer and top electrode was deposited in succession. The efficiency of the PSCs mostly depends on the proper selection of transporting materials. Mesoscopic layer (like, TiO_2) was deposited as a transporting layer in front of the light entering window to enhance the charge collection ability from perovskite layer and as a result the PSCs device performance enhanced.

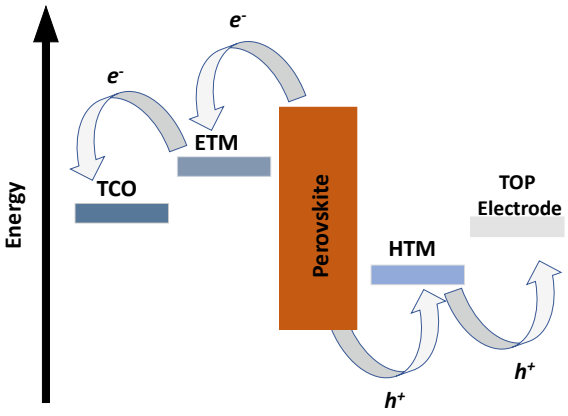

Fig. 12 Schematic energy band diagram of direct *n-i-p* structure

Inverted *p-i-n* structure. Inverted *p-i-n* structure was imported from the organic solar cells. Where the *p*-type hole-transporting layer (HTL) was deposited on top of the TCO and the *n*-type electron-transporting layer (ETL) was deposited under the top electrode. Here the holes and electrons are forced to move in two different directions and collected at different electrodes (see Fig. 13). In this device configuration, mesoscopic and planer PSCs were fabricated in the presence of different perovskite compositions.

Electron-transporting layer-free structure. A compact *p*-type transporting layer was deposited on top of transparent conductive oxide (see Fig. 14a), or on top of perovskite layer (see Fig. 14b) to fabricate electron-transporting layer-free PSCs. On top suitable electrodes are deposited. This type of PSCs is fabricated on planar structure and helps to achieve high PCE by increasing the open-circuit voltage (V_{oc}). Recently, scientists have developed a suitable method for fabricating PSCs without one transporting layer and achieved higher PCE.

The essential requirements of HTM layers in PSCs are due to several advantages such as,

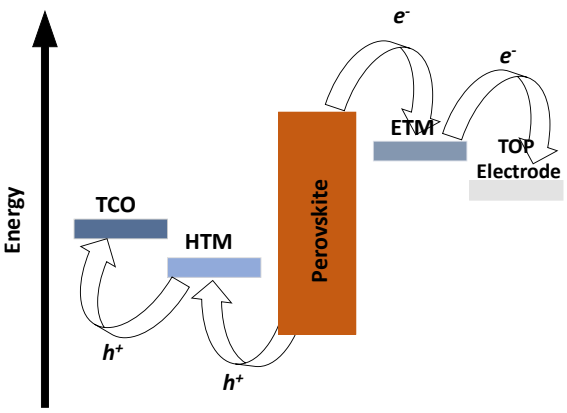

Fig. 13 Schematic energy band diagram of inverted *p-i-n* structure

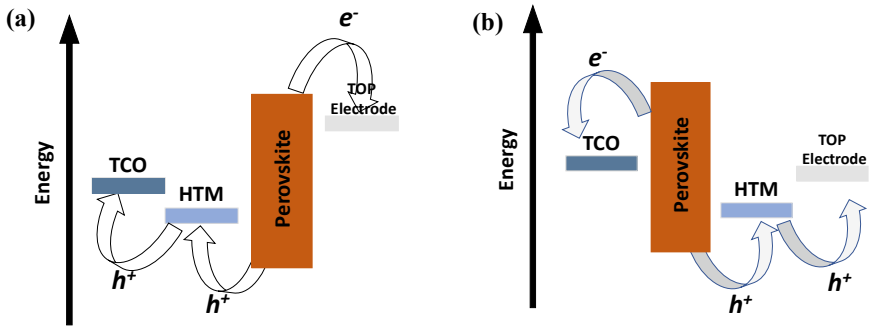

Fig. 14 Schematic energy band diagram of PSC without ETL **a** direct and **b** inverted structure

(1) Suitable band matching with perovskite layer helps to attain high V_{oc} values.
(2) Enhancement of the fill factor (FF) by reducing the series resistance governed by the high hole mobility in the device.
(3) The optical loss in the devices can be minimized by proper selection of low optical absorption of the transporting material in the visible region.

5.2 PSCs with Various HTM Layers and Their Device Performance

The thickness of the transporting layer should be maintained at an optimum value to overcome the resistive losses and allowed better crystalline growth of the perovskite. Some of the PSCs device structures are shown in Fig. 15.

Nanoparticles as HTMs
Nanomaterials are a suitable candidate for large-area optoelectronic industry due to their low production costs and ease synthesis helps. Superior optoelectronic properties such as easy processability, low synthesis cost, tunable band-gap, high mobility serve the nanomaterials as an alternative choice as a transporting layer material for PSCs. Tunable optoelectronic properties of nanomaterials help easy band matching with perovskite. As a result, the use of nanomaterials in the PSCs expected to improve the performance the device indeed. In the previous study, on colloidal QDs have been used in DSSC to get a device performance of 7% as an alternative to molecular dyes (Ip et al. 2012). Here, in this section we will discuss the device performance of in PSCs with various hole-transporting nanomaterials, such as Cu_2ZnSnS_4, WO_3, NiO, CuS nanocrystals (NCs) together with $CuInS_2$. and PbS-based QDs.

Cu_2ZnSnS_4 Nanoparticles (NPs). Earth-abundant Cu_2ZnSnS_4 (CZTS) NPs display some interesting properties such as high hole mobility (6–30 $cm^2\ V^{-1}\ s^{-1}$), ideal band-gap (1.5 eV) and permit them to use as a HTL in PSCs (Chen et al. 2013; Zhou et al. 2013; Walsh et al. 2012; Vanalakar et al. 2015). Wu et al. introduced the CZTS NPs as a transporting material due to the band matching with absorber perovskite layer in which the PCE was reached to 13% (Wu et al. 2015a). In this report, the NPs were synthesized with different reaction times of 20, 30, and 40 min to achieve different sizes such as CZTS-20, CZTS-30, and CZTS-40, and optical absorption was verified with mostly used organic HTM spiro-OMeTAD. After analyzing the SEM images, it was revealed that smooth, uniform, and homogeneous perovskite layer was formed on top of CZTS NPs. When compared with the commonly used spiro-OMeTAD HTM layer, it was found that the CZTS layer improved the interfacial contact between the perovskite layer and the top electrode to reduce the non-radiative recombination at the interfaces. The results suggested that the CZTS NPs can be effectively acts as a low-cost HTM layer as its able to transport holes effectively in PSCs (Fig. 16).

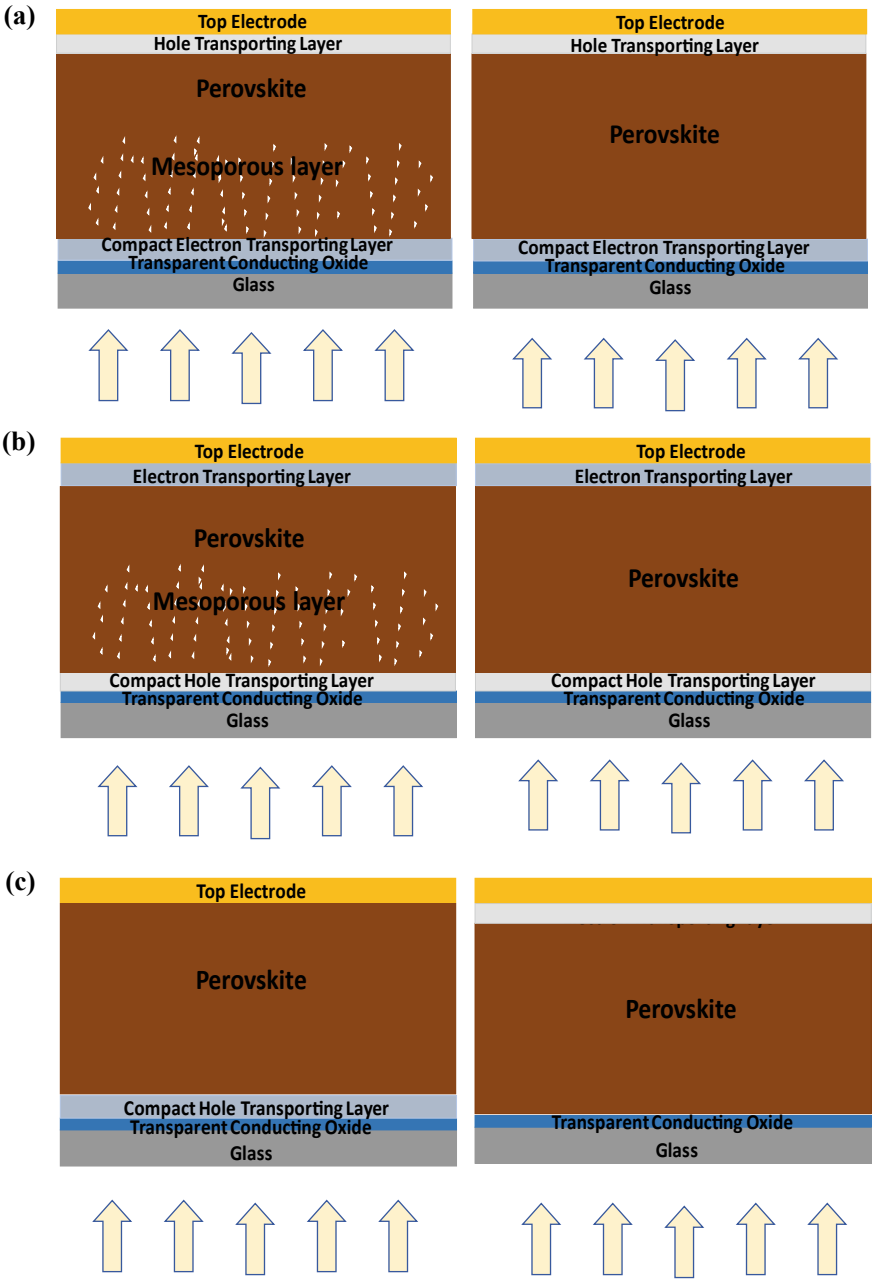

Fig. 15 **a** Left to right, normal *n-i-p* structure of PSCs in mesoporous and planar configuration of ETL. **b** Left to right, normal *p-i-n* structure of PSCs in mesoporous and planar configuration of HTL. **c** Structure of PSC without ETL (left) and without HTL (right)

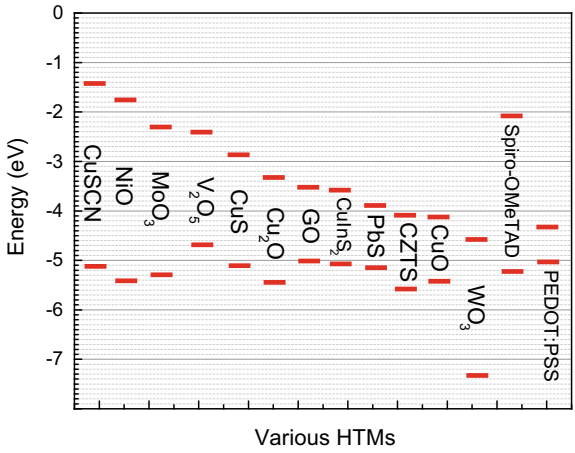

Fig. 16 Schematic energy band position of various HTMs used in PSCs

WO_3 NCs. In 2015, Li et al. had shown the successful use of WO_3 NCs as an efficient inorganic HTL in PSCs (Li 2015). Highly transparent WO_3 NCs layer (87% transparency) allows the incoming photons to be absorbed by the perovskite layer, high work function, and deep energy levels of WO_3 makes them efficient HTM in PSCs. It was also observed that the WO_3-based PSCs were more stable compared to the other organic and nanocrystalline HTLs-based solar cells. It was found that the device performance was considerably well with WO_3 as HTL and a PCE of 7.68% observed (Table 1).

NiO NCs. In 2014, Zhu et al. had successfully demonstrated the use of NiO NCs as an efficient HTL in PSCs. The NiO layer (30–40 nm thick) was grown by conventional sol–gel method and the corresponding solar cells device exhibited a PCE of 9.11% (Zhu et al. 2014). From the photoluminescence (PL) measurements, it was found that the NiO thin films have superior hole extraction ability from the perovskite layer compared to PEDOT:PSS layer.

CuS NPs. Rao et al. also discovered the use of CuS NPs as a hole-transporting material in an inverted perovskite solar cell (Rao et al. 2016). CuS NPs-based solar cells exhibit some interesting features, such as reproducibility, low charge recombination, effective hole extraction, higher stability, and ability to modify work function of ITO layer, found perfect band matching with the perovskite layer. From the SEM images, it was confirmed that the CuS NPs provide good surface coverage on ITO substrate. AFM studies of root-mean square (RMS) roughness suggest that no pinholes were formed in the CuS layer. From the J–V curves, it was discovered that the solar cell device exhibited PCE value of 16.2% and stability of the device boosted up to 250 h.

Copper indium disulfides ($CuInS_2$) colloidal Quantum Dots (QDs). Less toxic suitable band-gap (1.45 eV) with high extinction coefficient in the visible region of $CuInS_2$ QDs enables them to use as an HTM layer in PSCs. Lv et al. introduced $CuInS_2$ as an HTM in PSCs by replacing organic HTMs (Kolny-Olesaik and Weller

Table 1 Performance of perovskite (PVK) solar cells based on various oxides and NCs-based HTMs

Architecture	Cell structure for ***various oxides***	PCE (%)	J_{sc} (mA cm^{-2})	V_{oc} (V)	FF	References	Year
MoS_2 (planar *p-i-n*)	ITO/MoS_2/PVK/TiO_2/Ag	20.53	26.25	0.93	0.84	Kohnehpoushi et al. (2018)	2018
MoS_2 (mesoporous *n-i-p*)	FTO/TiO_2/PVK/MoS_2-QD/Au	20.12	22.81	1.11	0.79	Najafi et al. (2018)	2018
MoS_2 (mesoporous *n-i-p*)	FTO/TiO_2/PVK/MoS_2/spiro-OMeTAD/Au	13.09	21.09	0.93	0.66	Capasso et al. (2016)	2016
CZTS NCs	$MAPbI_3$	13.0	20.5	1.06	0.58	Wu et al. (2015a)	2015
VO_x (planar *p-i-n*)	ITO/VO_x/PVK/PCBM/C60/BCP/Al	11.7	20.8	1.02	0.56	Xiao et al. (2016)	2016
WO_3 (mesoporous *n-i-p*)	FTO/WO_3/TiO_2/PVK/spiro-OMeTAD/Ag	11.24	17.00	0.87	0.76	Mahmood et al. (2015a)	2015
WO_3 (mesoporous *n-i-p*)	FTO/WO_3/Cs_2CO_3/PCBM/PVK/P3HT/Au	10.49	20.4	0.84	0.61	Chen et al. (2016)	2016
NiO NCs	$MAPbI_3$	9.11	16.2	0.88	0.63	Zhu et al. (2014)	2014
WO_x (mesoporous *n-i-p*)	FTO/WO_3/TiO_2/PVK/spiro-OMeTAD/Ag	8.99	21.77	0.71	0.58	Wang et al. (2015a)	2015
$CuInS_2$ quantum dots	$MAPbI_3$	8.38	18.6	0.92	0.48	Lv et al. (2015)	2015
PbS quantum dots	$MAPbI_3$	7.88	12.1	0.86	0.72	Hu et al. (2015)	2015
WO_3 NCs	$MAPbI_3$	7.68	18.1	0.92	0.64	Li (2015)	2015
WO_3 (planar *p-i-n*)	ITO/WO_3/PVK/PCBM/Al	7.68	18.10	0.92	0.64	Li (2015)	2015

(continued)

Table 1 (continued)

Architecture	Cell structure for ***various oxides***	PCE (%)	J_{sc} (mA cm^{-2})	V_{oc} (V)	FF	References	Year
WO_3(mesoporous *n-i-p*)	FTO/WO_3/PVK/spiro-OMeTAD/Au	7.04	18.00	0.66	0.61	Zhang et al. (2016a)	2016
MoS_2 (planar *p-i-n*)	ITO/MoS_2/PVK/PCBM/Al	6.01	12.60	0.84	0.57	Dasgupta et al. (2017)	2017
PbS QDs	$MAPbI_3$	4.88	18.6	0.87	0.49	Li et al. (2015a)	2015
Carbon QDs	$MAPbI_3$	3.0	7.8	0.51	0.74	Paulo et al. (2016)	2016

2013). The use of $CuInS_2$ QDs (VB: 5.00–5.05 eV) improves the hole conduction from perovskite layer (VB: −5.43 eV) due to suitable band matching (Pan et al. 2014). The devices were fabricated by depositing colloidal $CuInS_2$ QDs on top of the $MAPbI_3$-coated TiO_2 films, during testing under suitable light intensity these cells delivered a PCE of 6.57%. The device performance was improved with a PCE of 8.38%, which was achieved by using modified $CuInS_2$ QDs with ZnS shell layer. The ZnS layer helps to reduce the non-radiative carrier recombination at the interface of TiO_2 and HTM layer (Santra et al. 2013).

Lead sulfide (PbS) QDs. Excellent optoelectronic properties of PbS QDs, such as high absorption coefficient, low band-gap, tunable band-gap, large exciton Bohr radius (~18 nm), motivate to implement them as a *p*-type HTM layer in PSCs (Hodes 2013; Snaith 2013). Solution-processed PbS QDs as an inorganic HTM layer in PSCs was successfully demonstrated and attained a PCE of 7.5% (Hu et al. 2015). By varying the band-gap of PbS QDs, the energy level alignments between the perovskite and PbS QDs can easily be tuned to achieve optimized device performance (Tang et al. 2011). Dai et al. have reached device efficiency nearly 8% with a good device stability by using colloidal PbS QDs as an inorganic HTM layer (Li et al. 2015a). This article investigated the solar cells performance by optimizing the PbS QDs layer thickness. Here two-step spin-coating method provides a higher PCE of 7.8%, whereas one-step method contributed lower PCE 4.73%. Enhanced solar cells device performance was achieved due to the low recombination in two-step processed perovskite thin films. From the SEM images of the two-step processed $MAPbI_3$, thin films deposited on TiO_2 layer showed more uniform surface coverage over the one-step process. These results discovered the efficient use of PbS QDs as a low-cost HTM in perovskite/QD hybrid solar cells.

Copper-based HTMs

Copper Iodide (CuI). Inexpensive, stable, wide band-gap, with high conductivity make CuI as a favorable candidate for HTM layer in PSCs. Christians et al., used CuI using the drop casting method and recorded a PCE of 6% (Christians et al. 2014). When compared with the conventional spiro-OMeTED HTM layer, it was found that the electrical conductivity of CuI solar cells was two orders higher and resulted in significant improvement in device performance. The stability test of these solar cell devices was carried out under constant illuminations of 100 mW/cm^2 AM 1.5G for a period of 2 h without encapsulation under ambient conditions. It was found that J_{sc} value remained constant for CuI based solar cells, while there is a decrement of J_{sc} of 10% from initial value was observed for spiro-OMeTAD-based solar cells. CuI HTM-based PSCs exhibited higher V_{oc} value with lower device efficiency compared to the conventional spiro-OMeTAD HTM-based solar cells (Table 2).

Cuprous oxide (Cu_2O) and Copper oxide (CuO). Earth-abundant and easy processable Cu_2O and CuO are typically *p*-type semiconductors, with suitable band alignment matches well with the perovskite ($MAPbI_3$) energy levels. Copper-based oxide materials have shown high hole mobility of 100 $cm^2\ V^{-1}\ s^{-1}$, which makes them suitable as an HTM material (Shao et al. 2010; Bao et al. 2009). Zuo et al. had

Table 2 Performance of various PSCs where CuI was used as HTM layer

Architecture	Cell structure for ***CuI***	PCE (%)	J_{sc} (mA cm^{-2})	V_{oc} (V)	FF	References	Year
Planar *p-i-n* (spin coating)	ITO/CuI/PVK/PCBM/BCP/Ag	16.8	22.6	0.99	0.71	Sun et al. (2016)	2016
Mesoscopic *n-i-p* (spin coating)	FTO/TiO_2/PVK/spiro-OMeTAD:CuI/Ag	16.67	21.52	1.06	0.73	Li et al. (2016a)	2016
Mesoscopic *n-i-p* (thermally evaporated)	FTO/CuI/PVK/PCBM/PEI/Ag	14.3	20.3	1.04	0.68	Wang et al. (2017a)	2017
Planar *p-i-n* (spin coating)	FTO/CuI/PVK/PCBM/Al	13.58	21.06	1.04	0.62	Chen et al. (2015b)	2015
Mesoscopic *n-i-p* (thermally evaporated)	FTO/TiO_2/PVK/CuI/Cu	9.24	22.99	0.85	0.47	Nazari et al. (2017)	2017
Mesoscopic *n-i-p* (doctor blading)	FTO/bl-TiO_2/PVK/CuI/graphite/Cu	7.5	16.7	0.78	0.57	Sepalage et al. (2015)	2015
Mesoscopic *n-i-p* (doctor blading)	FTO/bl-TiO_2/mp-TiO_2/PVK/CuI/Au	6.0	17.8	0.55	0.62	Christians et al. (2014)	2014
Mesoscopic *n-i-p* (spray Coating)	FTO/bl-TiO_2/mp-TiO_2/PVK/CuI/Au	5.6	22.6	0.64	0.39	Huangfu et al. (2015)	2015
Mesoscopic *n-i-p* (thermally evaporated)	FTO/TiO_2/PVK/CuI/Au	4.38	22.8	0.66	0.29	Gharibzadeh et al. (2016)	2016

successfully introduced the copper-based oxide materials as HTMs in PSCs. They have achieved maximum PCE of 13.35% with Cu_2O and 12.16% with CuO considered as inorganic HTMs (Zuo and Ding 2015). Cu_2O and CuO thin films showed smooth surface morphology that was analyzed from AFM study. The RMS values were obtained as of 2.81 nm and 3.32 nm, respectively. Highly crystalline $MAPbI_3$ films were observed on Cu_2O and CuO thin films compared with PEDOT:PSS films. These oxide transporting layers facilitate the charge transport and as a result increase in the device performance (Dong et al. 2015a). Cu_2O solar cells were found more stable compared to PEDOT:PSS-based solar cells. The PCE value of Cu_2O HTM-based solar cells reduced from 11.02 to 9.96%, whereas for PEDOT:PSS HTM-based solar cells declined from 10.11 to 6.79%, when the devices were kept for 70 days in the nitrogen filled glove box. In another study, Yu et al. have reported Cu_2O HTM-based PSCs with maximum PCE of 11.0% (Yu et al. 2016) (Table 3).

Sun et al. had reported a PCE of 17.1% by using CuO_x as an inorganic HTM layer in PSCs and exhibited short-circuited current density of 23.2 mA/cm^2, open-circuit voltage of 0.99 V, and fill factor of 0.74 (Sun et al. 2016). The devices were found to be stable for approximately 200 h. The better device performance of CuO_x-based PSC devices was achieved due to efficient hole transport from perovskite layer to HTM layer. Low contact resistance of CuO_x layer was beneficial for such enhanced device performance. From AFM study, it was discovered that the surface roughness or RMS value of ITO surface was 4.7 nm and the RMS value was decreased to 4.2 nm with addition of CuO_x HTM layer on top of ITO surface that improves the overall surface morphology and prevents short-circuited current leakage inside the device. Rao et al., have reported an output power efficiency of 19.0% where $MAPbI_{3-x}Cl_x$ have been used as an absorber layer and CuO_x used as a HTM layer (Rao et al. 2016). Doping of Cl offers the better surface morphology compared to undoped perovskites thin film and improved the hole mobility which in turn enhanced the device performance. The SEM morphology of $MAPbI_3$ films revealed that the average perovskite particle size was very small and form several grain boundaries, which trigger the non-radiative trap assisted recombination in turn reduced the overall device performance.

Copper thiocyanate (CuSCN). CuSCN is immensely used as an inorganic HTM layer in PSCs due to their some promising characteristics, such as their high optical transparency, high hole mobility of 0.01–0.1 $cm^2\ V^{-1}\ s^{-1}$ and good chemical stability (O'Regan et al. 2000; Tsujimoto et al. 2012; Pattanasattayavong et al. 2013a, b). Qin et al. had reported the fabrication of PSCs with copper thiocyanate (CuSCN) used as an HTM and achieved device PCE of 12.4% (Qin et al. 2014a). Ye et al. found in inverted PSCs with CuSCN HTM that exhibited an average PCE of 16.6% which was better compared to other conventional organic HTM layers used in PSCs (Ye et al. 2015). It was found that the device fabricated from perovskite layer deposited on top of a CuSCN via one-step deposition method was much efficient compared to two-step deposition. In one-step deposition process, the perovskites crystallized slowly and resulted in low surface roughness. The high device performance also signifies the smaller interface contact resistance between the perovskite layer and the CuSCN layer (Table 4).

Table 3 Performance of various copper oxide HTM layer-based PSCs

Architecture	Cell structure for ***copper oxide***	PCE (%)	J_{sc} (mA cm^{-2})	V_{oc} (V)	FF	References	Year
CuO_x planar *p-i-n* (spin coating)	ITO/CuO_x/PVK/PCBM/BCP/Ag	16.8	22.2	1.0	0.76	Sun et al. (2016)	2016
Cu_2O planar *p-i-n* (spin coating)	ITO/Cu_2O/PVK/PCBM/Ca–Al	13.35	16.52	1.07	0.76	Zuo and Ding (2015)	2015
CuO planar *p-i-n* (spin coating)	ITO/CuO/PVK/PCBM/Ca–Al	12.61	15.82	1.06	0.73	Zuo and Ding (2015)	2015
Cu:CrO_x planar *p-i-n* (spin coating)	FTO/Cu-CrO_x/PVK/PCBM/Ag	10.99	16.02	0.98	0.70	Qin et al. (2016)	2016
Cu_2O Mesoscopic *n-i-p* (spin coating)	FTO/TiO_2/PVK/Cu_2O/Au	8.93	15.8	0.96	0.59	Nejand et al. (2016)	2016
Cu_2O planar *p-i-n* (spin coating)	ITO/Cu_2O/PVK/PCBM/Al	8.30	15.60	0.92	0.58	Chatterjee and Pal (2016)	2016
Cu_xO planar *p-i-n* (electro spray)	ITO/Cu_xO/PVK/C60/BCP/Al	5.83	17.22	0.78	0.48	Bu et al. (2017)	2017

Table 4 Performance of various CuSCN HTM layer-based PSCs

Architecture	Cell structure for ***CuSCN***	PCE (%)	J_{sc} (mA cm^{-2})	V_{oc} (V)	FF	References	Year
Mesoscopic *n-i-p* (spin coating)	FTO/TiO_2/PVK:CuSCN/rGO/Au	20.8	23.35	1.13	0.77	Arora et al. (2017)	2017
Mesoscopic *n-i-p* (spin coating)	ITO/TiO_2/PVK/spiro-OMeTAD:CuSCN/Ag	18.02	22.01	1.06	0.77	Li et al. (2016a)	2016
Planar *n-i-p* (spin coating)	ITO/CuSCN/PVK/C60/Ag	17.2	22.3	1.09	0.71	Wijeyasinghe et al. (2017)	2017
Planar *n-i-p* (electro deposition)	ITO/CuSCN/PVK/C60/BCP/Ag	16.6	21.9	1.00	0.76	Ye et al. (2015)	2015
Mesoscopic *n-i-p* (doctor blading)	FTO/bl-TiO_2/mp-TiO_2/PVK/CuSCN/Au	16.6	21.8	1.1	0.69	Madhavan et al. (2016)	2016
Planar *p-i-n* (spin coating)	ITO/CuSCN/PVK/PCBM/PDINO/Al	16.4	21.4	1.05	0.73	Wang et al. (2016a)	2016
Mesoscopic *n-i-p* (spin coating)	FTO/bl-TiO_2/mp-TiO_2/PVK/CuSCN/Au	15.43	20.8	1.06	0.70	Madhavan et al. (2016)	2016
Mesoscopic *n-i-p* spray-coated	FTO/Al_2O_3/CuSCN/Au/PMMA	13.3	21.07	0.98	0.64	Liu et al. (2016a)	2016

(continued)

Table 4 (continued)

Architecture	Cell structure for ***CuSCN***	PCE (%)	J_{sc} (mA cm^{-2})	V_{oc} (V)	FF	References	Year
Mesoscopic *n-i-p* (doctor blading)	FTO/bl-TiO_2/mp-TiO_2/PVK/CuSCN/Au	12.4	19.7	1.026	0.62	Qin et al. (2014a)	2014
Planar *p-i-n* (spin coating)	ITO/CuSCN/PVK/PCBM/Al	12.4	19.1	1.0	0.65	Wang et al. (2016a)	2016
Planar *p-i-n* (spin coating)	ITO/CuSCN/PVK/PCBM/LiF-Ag	10.5	15.76	1.06	0.63	Zhao et al. (2015)	2015
Planar *p-i-n* (spin coating)	ITO/CuSCN/PVK/PCBM/C60/Ag	10.22	12.2	1.07	0.76	Jung et al. (2015a)	2015
Mesoscopic *n-i-p* (spin coating)	FTO/SnO_2/PVK/CuSCN/Au	8.38	18.99	0.96	0.45	Murugadoss et al. (2016)	2016
Mesoscopic *n-i-p* (doctor blading)	FTO/bl-TiO_2/PVK/CuSCN/Au	7.19	18.42	0.97	0.40	Ito et al. (2015)	2015
Mesoscopic *n-i-p* (drop casting)	FTO/bl-TiO_2/PVK/CuSCN/Au	6.4	18.53	0.727	0.617	Chavhan et al. (2014)	2014
Mesoscopic *n-i-p* (spin coating)	FTO/cp-TiO_2/mp-TiO_2/Sb_2S_3/PVK/CuSCN/Au	5.12	17.2	0.57	–	Ito et al. (2014b)	2014
Mesoscopic *n-i-p* (doctor blading)	FTO/bl-TiO_2/mp-TiO_2/PVK/CuSCN/Au	4.85	14.5	0.63	0.53	Ito et al. (2014a)	2014
Mesoscopic *n-i-p* (electro deposition)	FTO/CuSCN/PVK/PCBM/Ag	3.8	8.8	0.67	–	Subbiah et al. (2014)	2014

Nickel oxide (NiO_x). NiO_x is also ambient stable having larger band-gap (5.4 eV), and suitable energy levels match well with energy band to perovskite and make them as a potential candidate for HTM layer in PSCs. Yin et al. observed a higher PCE of 16.47% on a ITO-coated glass substrate compared to those of ITO-PEN (polyethylene naphthalate) substrate solar cells (PCE of 13.43%). Here solution-processed NiO_x was used as a HTM layer in the inverted planar heterojunction (Yin et al. 2016). From the J–V curve and EQE spectra, it was exposed that NiO_x-based device show low recombination than that of PEDOT:PSS which is commonly used HTM in perovskite solar cell. The use of pristine and copper-doped NiO_x as HTMs was represented by Kim et al., publicized the use of pristine and copper-doped NiO_x as HTMs for high performing and stable planar PSCs (Kim et al. 2014b). After careful analysis of J–V curves of Cu:NiO_x HTM-based PSC showed the maximum PCE of 15.40% compared to pristine NiO_x HTM exhibited PCE of 8.94%.

Wei et al. fabricated PSCs using Li–Mg-doped NiO as HTM and Ti(Nb)O_x used as an ETL, showing a highest PCE of 18.3% with a $J_{sc} = 20.4$ mA/cm^2, $V_{oc} = 1.08$ V, FF = 0.83 (Chen et al. 2015a). Introduction of Li^+ and Mg^{2+} into the NiO lattice increased the conductivity and avoid the undesirable shift of valence band (Chen et al. 2015a; Alidoust et al. 2014; Huang et al. 2014; Deng et al. 2012). For the stability test, the devices were kept under dark condition for 1000 h and it was found that the efficiency was reduced to its 97% from the initial value. Same experiment was carried out under 1000 h constant illumination condition, and the device PCE value was reduced to 90% from its initial value (Table 5).

Carbon Materials-based HTMs

Advantageous optoelectronic properties of carbon (*C*) materials, such as carbon nanotubes, graphene, and graphene oxide, as a transporting layer have gained significant attention in the field of organic electronics. It was observed that the carbon material-based solar cells had achieved a maximum PCE of 15.5% with better stability (Aitola et al. 2016). Zheng et al. had reported to achieve a PCE of 12.8% by using graphene sheet doped functionalized thiolated nanographene (TSHBC) as a HTM layer in PSCs and the device improved to an efficiency of 14% (Cao et al. 2015a) (Fig. 17; Table 6).

NiO_x/PEDOT:PSS. Use of hybrid PEDOT:PSS/NiO_x HTL was reported by Park et al. in an inverted planar device architecture and the device exhibited a PCE of 15.1% (Park et al. 2015). The hybrid PEDOT:PSS/NiO_x transporting layer was deposited by spin-coating different concentrations of (0.1, 1.0 and 5.0%) PEDOT:PSS solution on top of NiO_x layer. The device fabricated with 1.0% PEDOT:PSS/NiO_x as HTL displayed highest PCE of 13.9% compared to other compositions. Device with pure PEDOT:PSS (11.8%) and bare NiO_x (12.7%) achieved a lower PCE. From the impedance spectroscopy studies, it was observed that there was a subsequent reduction of internal resistance for PEDOT:PSS/NiO_x HTL based PSCs.

Spiro-OMeTAD. Due to several advantageous features of spiro-OMeTAD HTM layer, such as favorable glass transition temperature ($T_g = 120$ °C), easy solubility, ideal ionization potential, suitable absorption spectrum, and solid-state morphology

Table 5 Performance of various NiO HTM layer-based PSCs

Architecture	Cell structure for ***NiO***	PCE (%)	J_{sc} (mA cm^{-2})	V_{oc} (V)	FF	References	Year
Planar *p-i-n* (spraying)	FTO/NiO_x/$FAPbI_3$/PCBM/TiO_x/Ag	20.65	23.09	1.10	0.81	Xie et al. (2017)	2017
Planar *p-i-n* (spin coating)	ITO/NiO_x/PVK/PCBM/ZrAcac/Al	20.5	–	–	–	Yue et al. (2017)	2017
Planar *p-i-n* spray pyrolysis	FTO/NiO_x/PVK/PCBM/Ag	19.58	22.68	1.12	0.77	Wu et al. (2017)	2017
Planar *p-i-n* (spin coating)	FTO/Cs:NiO_x/PVK/PCBM/ZrAcac/Ag	19.35	21.77	1.12	0.79	Chen et al. (2017a)	2017
Planar *p-i-n* (spin coating)	ITO/NiO_x/PVK/PCBM/ZrAcac/Al	18.69	22.17	1.08	0.78	Chen et al. (2017b)	2017
Planar *p-i-n* (spin coating)	ITO/*Cu*:NiO_x/PVK/PCBM/BCP/Ag	18.66	20.76	1.11	0.81	He et al. (2017)	2017
Planar *p-i-n* (spin coating)	FTO/NiO_x/PVK/PCBM/Ag	18.6	22.8	1.09	0.75	Hu et al. (2017a)	2017
Planar *p-i-n* (spin coating)	ITO/NiO_x/PVK/PCBM/c-HATNA/Bis-C60/Ag	18.21	21.25	1.09	0.79	Zhu et al. (2018)	2018
Planar *p-i-n* (spin coating)	ITO/NiO_x/PVK/PCBM/Al	18.0	21.79	1.12	0.74	Nie et al. (2018)	2108
Planar *p-i-n* (combustion)	ITO/Cu:NiO/PVK/Bis-C60/C60/Ag	17.46	21.60	1.05	0.77	Jung et al. (2015b)	2105
Mesoscopic *p-i-n* (pulsed laser deposition)	ITO/PLD-NiO/PVK/PCBM/LiF-Al	17.3	20.2	1.06	0.81	Park et al. (2015)	2015
Planar *p-i-n* (spin coating)	ITO/NiO_x/PVK/PCBM/Ag	17.2	21.4	1.03	0.78	Kim et al. (2017)	2017

(continued)

Table 5 (continued)

Architecture	Cell structure for ***NiO***	PCE (%)	J_{sc} (mA cm^{-2})	V_{oc} (V)	FF	References	Year
Planar *p-i-n* (electrodeposition)	ITO/NiO_x/PVK/PCBM/Ag	17.1	22.6	1.05	0.72	Park et al. (2017)	2017
Planar *p-i-n* (spin coating)	ITO/NiO_x/PVK/PCBM/Ag	16.55	21.22	1.04	0.75	Ciro et al. (2017)	2017
Planar *p-i-n* (spin coating)	ITO/NiO_x/PVK/PCBM/Ag	16.47	20.58	1.07	0.75	Yin et al. (2016)	2016
Planar *p-i-n* (spin coating)	ITO/NiO_x/PVK/ZnO/Al	16.1	21.01	1.01	0.76	You et al. (2016)	2016
Planar *p-i-n* (spin coating)	FTO/Cu:NiO/PVK/PCBM/Ag	15.40	18.75	1.11	0.72	Kim et al. (2015)	2015
Planar *p-i-n* (vacuum deposition)	ITO/NiO_x/PVK/PCBM/BCP/Ag	15.4	18.6	1.06	0.78	Pae et al. (2018)	2018
Mesoscopic *n-i-p* (drop casting)	FTO/c-TiO_2/m-TiO_2/PVK:NiO-MWCNTs	15.38	22.38	0.90	0.76	Yang et al. (2017)	2017
Planar *p-i-n* (spin coating)	ITO/NiO-PEDOT/PVK/PCBM/Ag	15.1	20.1	1.04	0.72	Park et al. (2015)	2015
Multi-layered *n-i-p* (screen printing)	FTO/bl-TiO_2/mp-TiO_2/PVK/mp-Al_2O_3:PVK/mp-NiO:PVK/C	15.03	21.62	0.92	0.76	Cao et al. (2015b)	2015
Planar *p-i-n* (spray pyrolysis deposition)	FTO/NiMgLiO/PVK/PCBM/Ti(Nb)O_x/Ag	15.00	20.96	1.09	0.67	Chen et al. (2015a)	2015
Multi-layered *n-i-p* (screen printing)	FTO/bl-TiO_2/mp-TiO_2: PVK/mp-ZrO_2: PVK/mp-NiO: PVK/C	14.9	21.36	0.92	0.76	Xu et al. (2015a)	2015
Planar *p-i-n* (spin coating)	FTO/NiO_x/PVK/PCBM/Ag	14.42	17.93	1.09	0.74	Yin et al. (2015)	2015

(continued)

Table 5 (continued)

Architecture	Cell structure for ***NiO***	PCE (%)	J_{sc} (mA cm^{-2})	V_{oc} (V)	FF	References	Year
Mesoscopic *n-i-p* (dip coating)	FTO/c-TiO_2/m-TiO_2/m-ZrO_2: PVK/NiO-NS	14.2	20.4	0.97	0.72	Liu et al. (2015b)	2015
Mesoscopic *p-i-n* (spray pyrolysis deposition)	FTO/NiO/meso-Al_2O_3:PVK/PCBM/BCP/Ag	13.5	18.0	1.04	0.72	Chen et al. (2015c)	2015
Planar *p-i-n* (spin coating)	ITO-PEN/NiO_x-based flexible device/PVK/PCBM/Ag	13.43	18.74	1.04	0.69	Yin et al. (2016)	2016
Planar *p-i-n* (spin coating)	ITO/NiO_x/PVK/PCBM/LiF/Al	13.4	19	1.03	0.69	Kwon et al. (2016)	2016
Mesoscopic *n-i-p* (dip coating)	FTO/c-TiO_2/m-TiO_2/m-ZrO_2:PVK/NiO-NP	12.4	19.5	0.93	0.68	Liu et al. (2015b)	2015
Mesoscopic *p-i-n* (sputtering)	ITO/bl-NiO_x/nc-NiO/PVK/PCBM/BCP/Al	11.6	19.8	0.96	0.61	Wang et al. (2014b)	2014
Multi-layered *n-i-p* (screen printing)	FTO/bl-TiO_2/mp-TiO_2:PVK/mp-NiO:PVK/*C*	11.4	18.2	0.89	0.71	Liu et al. (2015c)	2015
Planar *p-i-n* (spin coating)	FTO/NiO NCs/PVK/PCBM (1.5 wt% PS)/*Al*	10.68	15.62	1.07	0.64	Bai et al. (2015)	2015
Planar *p-i-n* (vacuum thermal evaporation)	ITO/NiO_x/PVK/PCBM/C60/BCP/*Al*	10.6	18	1.06	0.56	Xiao et al. (2016)	2016
Planar *p-i-n* (sputtering)	FTO/NiO/PVK/PCBM/BCP/Au	9.83	15.17	1.10	0.59	Mamun et al. (2017)	2017
Mesoscopic *p-i-n* (spin coating)	ITO/NiO_x/nc-NiO/PVK/PCBM/BCP/Al	9.51	13.24	1.04	0.69	Wang et al. (2014a)	2014
Planar *p-i-n* (spin coating)	FTO/NiO/PVK/PCBM/Au	9.11	16.27	0.88	0.64	Zhu et al. (2014)	2014

(continued)

Table 5 (continued)

Architecture	Cell structure for ***NiO***	PCE (%)	J_{sc} (mA cm^{-2})	V_{oc} (V)	FF	References	Year
Planar *p-i-n* (spin coating)	ITO/NiO/PVK/PCBM/Ag	8.94	14.13	1.08	0.58	Kim et al. (2015)	2015
Planar *p-i-n* (spin coating)	ITO/NiO/PVK/PCBM/BCP/Al	7.8	12.43	0.92	0.68	Jeng et al. (2014)	2014
Planar *p-i-n* e-beam evaporator	ITO/NiO_x/PVK/PCBM/BCP/Al	7.75	13.16	0.90	0.65	Wei-Chih et al. (2015)	2015
Planar *p-i-n* (spin coating)	ITO/NiO/PVK/PCBM/Al	7.6	15.4	1.05	0.48	Hu et al. (2014b)	2014
Planar *p-i-n* (electro deposition)	FTO/NiO/PVK/PCBM/Ag	7.26	14.2	0.79	0.65	Subbiah et al. (2014)	2014
Mesoscopic *n-i-p* (screen printing)	FTO/bl-NiO/nc-NiO/PVK/PCBM/Al	1.50	4.94	0.83	0.35	Tian et al. (2014)	2014
Mesoscopic *n-i-p* (screen printing)	FTO/NiO_x/PVK/Pt/FTO	0.71	9.47	0.21	0.36	Wang et al. (2014c)	2014

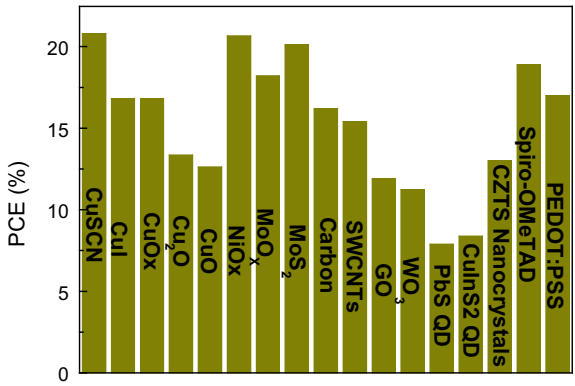

Fig. 17 Graphical representation of PCE value associated, different HTM materials used in perovskite solar cells

introduced them the most commonly used organic HTM layer in PSCs which can provide the high output (Huang et al. 2016a). Spiro-OMeTAD was introduced by Bach et al. in 1998 (Bach et al. 1998) in DSSCs to use them as an efficient heterojunction layer formed with dye absorbers achieved a good PCE. Recently, many researchers extensively utilized the spiro-OMeTAD as HTM layer in solid-state DSSCs. Using spiro-OMeTAD, the PSCs boosted the device PCE up to 22%. The devices fabricated with spiro-OMeTAD suffered low stability toward water, light, and heat due to amorphous nature and the chemical structure spiro-OMeTAD. Pristine and various-doped spiro have been used as a HTM layer in PSCs to overcome the low stability of the devices. These various dopants in the spiro-OMeTAD enhance the electrical conductivity, stability of the device. The first doping effect was employed in spiro-OMeTAD by lithium and antimony-based salts $Li[(CF_3SO_2)_2N]$ (Li-TFSI) and achieved the highest PCE of 7.2% (Burschka et al. 2013). Doping of antimony in spiro-OMeTAD resulted in generation of free charge carriers via oxidization. Generated Li^+ ions inside the system by the ionic lithium improve the device performance, but due to extreme hygroscopic nature of lithium accelerates the decomposition of perovskite and degrades the device performance quickly. The presence of pinhole channels from the bottom to the top across the organic transporting layer spiro-OMeTAD accelerates the degradation processes, the pinholes are generated from the migration of Li-TFSI film, Hawash et al. (2015). Hua et al. (2016) had successfully demonstrated the use of fluorine-doped spiro-OMeTAD and found enhanced stability of PSCs. Improvement of the device performance was observed when non-hygroscopic materials (tetrafluoro-tetra cyanoquinodimethane [F4-TCNQ])-doped spiro-OMeTAD used instead of pristine spiro-OMeTAD. The energy offset between the perovskite and the spiro-OMeTAD has to be small enough in order to achieve a high V_{oc} (Ou et al. 2017). In 2018, Hawash et al. observed that spiro-OMeTAD with various new additives and dopants excels pristine spiro-OMeTAD both in terms of device performance and stability (Hawash et al. 2018) (Fig. 18; Table 7).

PEDOT:PSS mixed polymer-based HTMs. The HOMO energy level of PEDOT film at −5.0 eV facilities the hole extraction from the perovskite layer due to band

Table 6 Performance of various carbon and carbon CNT HTM layer-based PSCs

Architecture	Cell structure for ***carbon***	PCE (%)	J_{sc} (mA cm^{-2})	V_{oc} (V)	FF	References	Year
Carbon mesoporous *p-i-n* (e-beam)	FTO/PEDOT:PSS/$MAPbI_{3-x}Cl_x$/PCBM/C	16.2	23.69	0.96	0.71	Wang et al. (2016b)	2016
Carbon mesoporous *n-i-p* (doctor blading)	FTO/TiO_2/mp-TiO_2/PVK/CuPc nanorods/C	16.1	20.8	1.05	0.74	Zhang et al. (2016c)	2016
Carbon Multi-layered *n-i-p* (screen printing)	FTO/TiO_2/mp-TiO_2/ZrO_2/PVK/C	15.60	21.45	0.94	0.77	Rong et al. (2017)	2017
Carbon mesoporous *n-i-p* (doctor blading)	FTO/TiO_2/mp-TiO_2/PVK/doped-TPDI/C	15.5	20.1	1.03	0.75	Zhang et al. (2015b)	2015
Carbon mesoporous *n-i-p* (doctor blading)	FTO/TiO_2/mp-TiO_2/PVK/Spiro-OMeTAD/C	15.29	20.42	1.12	0.67	Gholipour et al. (2016)	2016
Carbon/graphite multi-layered *n-i-p* (screen printing)	FTO/c-TiO_2/TiO_2/Al_2O_3/NiO/C/PVK	15.03	21.62	0.91	0.76	Cao et al. (2015b)	2015
Carbon mesoporous *n-i-p* (screen printing)	FTO/TiO_2/mp-TiO_2/PVK/Al_2O_3/C	15.0	22.43	0.89	0.75	Tsai et al. (2017)	2017
Carbon multi-layered *n-i-p* (blade coating)	FTO/TiO_2/mp-TiO_2/PVK/ZrO_2/NiO/C/graphite	14.9	21.36	0.92	0.76	Cao et al. (2015b)	2015
Carbon mesoporous *n-i-p* (paint)	FTO/TiO_2/mp-TiO_2/PVK/C	14.58	21.83	1.0	0.67	Chang et al. (2016b)	2016
Carbon mesoporous *n-i-p* (screen printing)	FTO/TiO_2/mp-TiO_2/PVK/C	14.38	21.27	1.04	0.65	Chen et al. (2016f)	2016
Carbon multi-layered *n-i-p* (screen printing)	FTO/TiO_2/mp-TiO_2/ZrO_2/PVK/C	14.35	19.31	1.00	0.74	Hou et al. (2017)	2017

(continued)

Table 6 (continued)

Architecture	Cell structure for ***carbon***	PCE (%)	J_{sc} (mA cm^{-2})	V_{oc} (V)	FF	References	Year
Carbon mesoporous *n-i-p* (screen printing)	FTO/TiO_2/mp-TiO_2/PVK/NiO nanosheets/C	14.2	20.4	0.97	0.72	Liu et al. (2015c)	2015
Carbon Multi-layered *n-i-p* (screen printing)	FTO/m-TiO_2/ZrO_2/*C* (perovskite infiltration)	14.3	21.5	0.86	0.77	Hashmi et al. (2017)	2017
C60 mesoporous *p-i-n* (e-beam)	FTO/PEDOT:PSS/PVK/PCBM/C60	14.0	22.47	0.97	0.64	Mamun et al. (2017)	2017
Carbon multi-layered *n-i-p* (screen printing)	FTO/TiO_2/mp-TiO_2/ZrO_2/PVK/C	13.89	19.21	0.92	0.78	Chen et al. (2016c)	2016
Carbon mesoporous *n-i-p* (hot press)	FTO/TiO_2/PVK/Carbon/Al	13.53	21.30	1.00	0.63	Wei et al. (2015a)	2015
Carbon multi-layered *n-i-p* (screen printing)	FTO/TiO_2/mp-TiO_2/ZrO_2/PVK/C	13.41	22.93	0.87	0.67	Yang et al. (2015b)	2015
Carbon mesoporous *n-i-p* (screen printing)	FTO/TiO_2/mp-TiO_2/PVK/ZrO_2/C	13.24	18.15	0.96	0.76	Chen et al. (2016d)	2016
Carbon multi-layered *n-i-p* (screen printing)	FTO/bl-TiO_2/mp-TiO_2: PVK/mp-ZrO_2: PVK/C	13.14	20.45	0.90	0.72	Liu et al. (2015d)	2015
Carbon multi-layered *n-i-p* (screen printing)	FTO/bl-TiO_2/mp-TiO_2: PVK/mp-ZrO_2:PVK/C	12.84	22.8	0.86	0.66	Liu et al. (2015d)	2015
Carbon mesoporous *n-i-p* (screen printing)	FTO/TiO_2/mp-TiO_2/PVK/Al_2O_3/C	12.3	20.04	0.85	0.72	Chan et al. (2016)	2016
Carbon multi-layered *n-i-p* (printed)	FTO/m-TiO_2/Al_2O_3/NiO_x/C (dip coating PVK)	12.12	17.22	0.95	0.69	Behrouznejad et al. (2017)	2017
Carbon mesoporous *n-i-p* (doctor blading)	FTO/TiO_2/mp-TiO_2/PVK/C	12.02	22.67	1.00	0.53	Nouri et al. (2017)	2017

(continued)

Table 6 (continued)

Architecture	Cell structure for ***carbon***	PCE (%)	J_{sc} (mA cm^{-2})	V_{oc} (V)	FF	References	Year
Carbon multi-layered *n-i-p* (printing)	FTO/m-TiO_2/2D-3D PVK/ZrO_2/C	11.9	23.60	0.86	0.59	Grancini et al. (2017)	2017
Carbon multi-layered *n-i-p* (screen printing)	FTO/bl-TiO_2/mp-TiO_2: PVK/mp-ZrO_2:PVK/C	11.63	18.06	0.89	0.72	Zhang et al. (2015a)	2015
Carbon planar *p-i-n* (inkjet printing)	FTO/TiO_2/PVK/C	11.60	17.20	0.95	0.71	Wei et al. (2014)	2014
Carbon mesoporous *n-i-p* (spin coating)	FTO/TiO_2/PVK/C	11.44	21.43	0.89	0.60	Zhang et al. (2016d)	2016
Carbon multi-layered *n-i-p* (screen printing)	FTO/TiO_2/NiO/PVK/*C*	11.4	18.2	0.89	0.71	Liu et al. (2015c)	2015
Carbon mesoporous *n-i-p*	FTO/TiO_2/mp-TiO2/PVK/mp-ZrO_2/C	11.07	–	–	–	Xu et al. (2017)	2017
Carbon/graphite multi-layered *n-i-p* (screen printing)	FTO/TiO_2/mp-TiO2/Al_2O_3/PVK/C	11.03	15.37	1.04	0.69	Cao et al. (2015c)	2015
Carbon mesoporous *n-i-p* (rolling transfer)	FTO/TiO_2/PVK/C (cathode soot)	11.02	17.00	0.90	0.72	Sepalage et al. (2015)	2015
Carbon mesoporous *n-i-p* (doctor blading)	FTO/TiO_2/mp-TiO_2/PVK/*C*/PDMS	10.8	23.5	0.97	0.47	Liu et al. (2016b)	2016
Carbon/graphite multi-layered *n-i-p* (screen printing)	FTO/d-TiO_2/mp-TiO_2/PVK/ZrO_2/C/graphite	10.64	20.1	0.87	0.61	Rong et al. (2014)	2014
Carbon mesoporous *n-i-p* (blade coating)	FTO/d-TiO_2/W-doped mp-TiO_2/PVK/C	10.53	20.79	0.86	0.59	Xiao et al. (2017)	2017

(continued)

Table 6 (continued)

Architecture	Cell structure for ***carbon***	PCE (%)	J_{sc} (mA cm^{-2})	V_{oc} (V)	FF	References	Year
Carbon mesoporous *n-i-p* (doctor blading)	FTO/TiO_2/mp-TiO_2/PVK/C	10.4	20.1	0.80	0.64	Li et al. (2017b)	2017
Carbon Mesoporous *n-i-p* (screen printing)	FTO/TiO_2/mp-TiO_2/PVK/C	10.19	19.1	0.97	0.55	Chen et al. (2015d)	2015
Carbon mesoporous *n-i-p* (hot press)	FTO/TiO_2/PVK/C/graphite sheet	10.20	18.73	0.95	0.57	Yang et al. (2014)	2014
Carbon mesoporous *n-i-p* (screen printing)	FTO/c-TiO_2/silver contact/mp-TiO_2/PVK/ZrO_2/C	9.53	16.57	0.86	0.67	Wang et al. (2016b)	2016
Carbon mesoporous *n-i-p* (spin coating)	FTO/TiO_2/PVK/C	9.35	15.98	0.90	0.65	Wei et al. (2015b)	2015
Carbon multi-layered *n-i-p* (screen printing)	FTO/TiO_2/mp-TiO_2/ZrO_2/PVK/C	9.10	15.10	0.88	0.68	Hou et al. (2017)	2017
Carbon mesoporous *n-i-p* (doctor blading)	FTO/TiO_2/PVK/C	9.08	21.02	0.80	0.54	Zhou et al. (2014a)	2014
Carbon mesoporous *n-i-p* (doctor blading)	FTO/C-ZnO/PVK/C	8.73	19.98	0.81	0.54	Zhou et al. (2015)	2015
Carbon mesoporous *n-i-p* (doctor blading)	FTO/TiO_2/mp-TiO_2/PVK/Spiro-OMeTAD/C	8.70	18.42	1.08	0.43	Gholipour et al. (2016)	2016
Carbon mesoporous *n-i-p* (spin coating)	FTO/TiO_2/PVK/*C*	8.61	14.20	1.01	0.60	Chen et al. (2014)	2014
Carbon mesoporous *n-i-p* (doctor blading)	FTO/TiO_2/PVK/C	8.31	16.78	0.90	0.55	Zhang et al. (2014)	2014
Carbon multi-layered *n-i-p* (screen printing)	FTO/d-ZnO/PVK/ZnO NR layer/ZrO_2/C	8.23	14.82	0.96	0.58	Wang et al. (2016b)	2016

(continued)

Table 6 (continued)

Architecture	Cell structure for ***carbon***	PCE (%)	J_{sc} (mA cm^{-2})	V_{oc} (V)	FF	References	Year
Carbon mesoporous *n-i-p* printing	FTO/TiO_2/mp-TiO_2/PVK/C	8.09	8.35	1.35	0.72	Chen et al. (2016e)	2016
Carbon multi-layered *n-i-p* (doctor blading)	FTO/TiO_2/mp-TiO_2/porous Al_2O_3/PVK/*C*	8.0	15.1	0.78	0.68	Xu et al. (2014)	2014
Carbon Planar *p-i-n* (doctor blading)	FTO/TiO_2/PVK/*C*	8.07	18.56	0.77	0.56	Zhou et al. (2015)	2015
Carbon mesoporous *n-i-p* (doctor blading)	FTO/TiO_2/mp-TiO_2/PVK/*C*	7.29	18.40	0.81	0.50	Yue et al. (2016)	2016
Carbon multi-layered *n-i-p* (screen printing)	FTO/bl-TiO_2/mp-TiO_2: PVK/mp-ZrO2:PVK/*C*	7.08	15.24	0.87	0.54	Wang et al. (2015b)	2015
Carbon mesoporous *n-i-p* (doctor blading)	FTO/TiO_2/mp-TiO_2/PVK/*C*	6.88	18.3	0.85	0.44	Liu et al. (2016c)	2016
Carbon mesoporous *n-i-p* (doctor blading)	FTO/TiO_2/mp-TiO_2/PVK/boron and phosphorus co doped *C*/Al	6.78	12.35	0.90	0.61	Chen et al. (2017c)	2017
Carbon multi-layered *n-i-p* (screen printing)	FTO/bl-TiO_2/mp-TiO_2: PVK/mp-ZrO_2:PVK/*C*	6.64	12.4	0.88	0.61	Ku et al. (2013)	2013
Carbon multi-layered *n-i-p* (screen printing)	FTO/d-ZnO/PVK/(ZnO/TiO_2 NR layer)/ZrO_2/*C*	5.56	14.19	0.84	0.46	Wang et al. (2016b)	2016
Carbon mesoporous *n-i-p* (screen printing)	FTO/TiO_2/mp-TiO_2/PVK/Al_2O_3/*C*	5.13	19.63	0.46	0.57	Tsai et al. (2016)	2016
Carbon/graphite mesoporous *n-i-p* (printing)	FTO/TiO_2/mp-TiO_2/PVK/C	5.0	5.7	1.29	0.68	Chang et al. (2016a)	2016

(continued)

Table 6 (continued)

Architecture	Cell structure for ***carbon***	PCE (%)	J_{sc} (mA cm^{-2})	V_{oc} (V)	FF	References	Year
Carbon planar *p-i-n* (doctor blading)	ITO/PEN/ZnO/PVK/*C*	4.29	13.38	0.76	0.42	Zhou et al. (2015)	2015
Carbon mesoporous *n-i-p* (soot of burning candle)	FTO/TiO_2/mp-TiO_2/PVK/spiro-OMeTAD/*C*/FTO	4.24	12.30	0.82	0.42	Zhang et al. (2016b)	2016
SWCNTs:spiro-OMeTAD mesoporous *n-i-p* (CVD process)	FTO/TiO_2/PVK/SWCNTs: Spiro-OMeTAD	15.5	20.3	1.1	0.61	Im et al. (2013)	2011
SWCNTs mesoporous *n-i-p* (spin coating)	FTO/TiO_2/mp-Al_2O_3:PVK/SWCNTs/spiro-OMeTAD/Ag	15.4	21.4	1.02	0.71	Habisreutinger et al. (2014b)	2014
SWCNTs Mesoporous *n-i-p* (spin coating)	FTO/TiO_2/mp-Al_2O_3:PVK/SWCNTs:P3HT-PMMA/Ag	15.3	22.71	1.02	0.66	Habisreutinger et al. (2014a)	2014
MWCNTs mesoporous *n-i-p* (drop casting)	FTO/TiO_2/mp-TiO_2/PVK/Al_2O_3/*B*-doped MWNTs	15.23	–	0.92	0.77	(Zheng et al. 2017)	2017
GO mesoporous *n-i-p* (spin coating)	FTO/TiO_2/PVK/graphene oxide/spiro-OMeTAD/*Au*	15.1	20.2	1.04	0.73	Li et al. (2014a)	2014
MWCNTs planar *n-i-p* (spin coating)	FTO/TiO_2/PVK/MWCNT :spiro-OMeTAD/*Au*	15.1	–	–	–	Lee et al. (2015b)	2015
SWCNTs-carbon mesoporous *n-i-p* (spin coating)	FTO/TiO_2/Al_2O_3/PVK/SWCNTs-*C*	14.7	21.26	1.01	0.69	Li et al. (2016b)	2016
SWCNTs mesoporous *n-i-p* Press transfer	FTO/TiO_2/mp-TiO_2/PVK/spiro-OMeTAD/SWCNTs	13.6	20.3	1.1	0.61	Im et al. (2013)	2011

(continued)

Table 6 (continued)

Architecture	Cell structure for ***carbon***	PCE (%)	J_{sc} (mA cm^{-2})	V_{oc} (V)	FF	References	Year
CNTs Mesoporous *n-i-p* (dripping/screen printing)	FTO/b-TiO_2/mp-TiO_2/PVK/CNT/*C*	13.57	18.97	1.00	0.71	Ryu et al. (2017)	2017
SWCNTs/GO/PMMA mesoporous *n-i-p* (spin coating)	FTO/TiO_2/PVK/SWCNTs/GO/PMMA	13.3	19.4	0.95	0.72	Wang et al. (2016c)	2016
Thiolatednano graphene mesoporous *n-i-p* (spin coating)	FTO/TiO_2/PVK/thiolated nanographene	12.81	20.56	0.95	0.66	Kim et al. (2014a)	2014
SWCNTs mesoporous *n-i-p* (screen printing)	FTO/TiO_2/mp-TiO_2/Al_2O_3/NiO/SWNCTs	12.7	20.7	0.95	0.64	Liu et al. (2017b)	2017
MWCNTs mesoporous *n-i-p* (drop cast)	FTO/TiO_2/PVK/MWCNTs	12.67	18.00	0.88	0.80	Wei et al. (2015b)	2015
Graphene planar *p-i-n* (chemical vapor deposition)	FTO/TiO_2/PVK/spiro-OMeTAD/PEDOT:PSS/graphene	12.37	19.17	0.96	19.17	You et al. (2015)	2015
GO planar *n-i-p* (spin coating)	–	11.90	19.18	0.88	0.71	Liu et al. (2015e)	2015
MWCNTs multi-layered *n-i-p* (doctor blading)	FTO/d-TiO_2/(TiO_2/SiO_2)/PVK/*C*	11.6	21.3	0.93	0.59	Cheng et al. (2016)	2016
Multi-layered graphene mesoporous *n-i-p* (spin coating)	FTO/TiO_2/PVK/multi-layered graphene	11.5	16.7	0.94	0.73	Yan et al. (2015)	2015

(continued)

Table 6 (continued)

Architecture	Cell structure for ***carbon***	PCE (%)	J_{sc} (mA cm^{-2})	V_{oc} (V)	FF	References	Year
CNTs planer *p-i-n* (PDMS stamp)	ITO/PEDOT:PSS/PVK/PCBM/CNTs	11.16	19.5	0.97	0.59	Mielczarek and Zakhidov (2014)	2014
GO planar *p-i-n* (spin coating)	ITO/graphene oxide/PVK/PCBM/ZnO/*Al*	11.11	15.59	0.99	0.72	Wu et al. (2014)	2014
rGO planar *p-i-n* (spin coating)	ITO/reduced graphene oxide/PCBM/PCB/*Ag*	10.8	15.4	0.98	0.72	Yeo et al. (2015)	2015
CNTs mesoporous *n-i-p* (transfer)	FTO/TiO_2/mp-TiO_2/PVK/Al_2O_3/CSCNTs/PMMA	10.54	17.22	0.85	0.71	Luo et al. (2016)	2016
CNTs *p-i-n*	ITO/PEDOT:PSS/PVK/PCBM/CNTs	10.5	18.1	0.79	0.73	Jeon et al. (2017)	2017
MWCNTs mesoporous *n-i-p* (spin coating)	FTO/TiO_2/PVK/MWCNTs	10.30	15.60	0.88	0.75	Wei et al. (2015b)	2015
Graphene mesoporous *n-i-p* (doctor blading)	FTO/TiO_2/(PVK/3DHG)/3DHG	10.06	0.89	0.63	18.11	Wei et al. (2017)	2017
SWCNTs/GO mesoporous *n-i-p* (spin coating)	FTO/TiO_2/PVK/SWCNTs/GO	9.8	19.1	0.89	0.57	Liu et al. (2017b)	2017
CNTs film Mesoporous *n-i-p* (attaching)	FTO/TiO_2/PVK/CNT film:spiro-OMeTAD	9.90	18.1	1.00	0.55	Li et al. (2014b)	2014
CNTs mesoporous *n-i-p* (transfer)	FTO/TiO_2/mp-TiO_2/PVK/Al_2O_3/CSCNTs/PMMA	9.37	16.21	0.84	0.69	Luo et al. (2016)	2016
Iodide-r-GO mesoporous *n-i-p* (spin coating)	FTO/TiO_2/PVK/iodide-reduced graphene oxide: spiro-OMeTAD/Au	9.31	16.73	0.91	0.61	Luo et al. (2015)	2015

(continued)

Table 6 (continued)

Architecture	Cell structure for ***carbon***	PCE (%)	J_{sc} (mA cm^{-2})	V_{oc} (V)	FF	References	Year
SWCNTs mesoporous *n-i-p* (chemical vapor deposition)	FTO/TiO_2/PVK/SWCNTs	9.1	20.3	0.97	0.46	Im et al. (2013)	2011
CNTs mesoporous *n-i-p* (transfer)	FTO/TiO_2/mp-TiO_2/PVK/Al_2O_3/CSCNTs/PMMA	8.60	14.91	0.85	0.68	Luo et al. (2016)	2016
CNTs mesoporous *n-i-p* (transfer)	FTO/TiO_2/mp-TiO_2/PVK/Al_2O_3/CSCNTs/PMMA	8.35	15.81	0.82	0.64	Luo et al. (2016)	2016
CNTs mesoporous *n-i-p* (chemical vapor deposition)	*Ti* foil/TiO_2 nanotube/PVK/spiro-OMeTAD: CNTs	8.31	14.36	0.99	0.68	Wang et al. (2015c)	2015
Bamboo-structured CNTs mesoporous *n-i-p* (spin coating)	FTO/TiO_2/PVK/bamboo-structured CNTs:P3HT/Au	8.3	18.75	0.86	0.52	Cai et al. (2015)	2015
CNTs film mesoporous *n-i-p* (attaching)	FTO/TiO_2/PVK/CNTs film	6.87	15.46	0.88	0.51	Li et al. (2014b)	2014
CNTs mesoporous *n-i-p* (transfer)	FTO/TiO_2/mp-TiO_2/PVK/Al_2O_3/CSCNTs/PMMA	6.81	14.43	0.88	0.53	Luo et al. (2016)	2016
Graphene mesoporous *n-i-p* (spin coating)	FTO/TiO_2/PVK bilayer/SG	6.7	14.2	0.54	0.878	Luo et al. (2016)	2016
Single-walled CNTs planar *n-i-p* (chemical vapor deposition)	Single-walled-CNTs/PEDOT:PSS/PVK/PCBM/*Al*	6.32	14.9	0.79	0.54	Jeon et al. (2015a)	2015

(continued)

Table 6 (continued)

Architecture	Cell structure for ***carbon***	PCE (%)	J_{sc} (mA cm^{-2})	V_{oc} (V)	FF	References	Year
Graphene planar *n-i-p* (chemical vapor deposition)	FTO/TiO_2/PVK/spiro-OMeTAD/graphene	6.2	12.56	0.90	0.55	Lang et al. (2015)	2015
Graphite mesoporous *n-i-p* (spin coating)	FTO/TiO_2/PVK/Graphite	6.13	10.30	0.93	0.64	Wei et al. (2015b)	2015
SWCNTs mesoporous *n-i-p* (spin coating)	FTO/TiO_2/PVK/SWCNTs	4.9	10.47	0.73	0.64	Wang et al. (2016c)	2016
CNTs sheet mesoporous *n-i-p* (dip-coated)	Stainless Steel/TiO_2/PVK/spiro-OMeTAD/CNTs sheet	3.3	10.2	0.66	0.48	Qiu et al. (2014)	2014

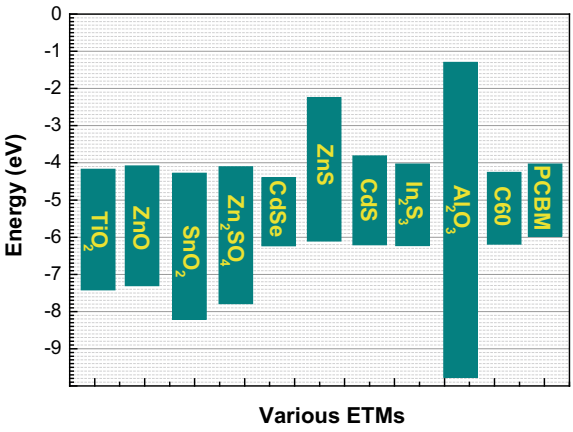

Fig. 18 Schematic energy band position of various ETMs used in PSCs

matching. In 2014, You et al. (2014) had successfully demonstrated the use of poly (3,4-ethylene dioxythiophene) polystyrene sulfonate polymer (PEDOT:PSS) as an HTM to fabricate high-efficiency PSCs at a low temperature, where PEDOT:PSS and PCBM were used as hole and electron transport layers, respectively. The device exhibited a PCE of 11.5% on glass/ITO substrate, while a 9.2% PCE was achieved in a flexible substrate (polyethylene terephthalate/ITO). The successfully grown of conducting poly (3,4-ethylene dioxythiophene) polystyrene sulfonate polymer (PEDOT:PSS) and applys them as a potential HTM in PSCs was demonstrated by Jiang et al. in 2017, (Jiang et al. 2017). They had deposited PEDOT:PSS layer on top of perovskite and showed an excellent PCE of 17.0%. One of the major drawback of PSCs fabricated by depositing PEDOT:PSS on top of perovskite layer is their limited stability in ambient atmosphere, modified by the inverted structure of PSCs, where perovskite layer was deposited on top of PEDOT: PSS layer. In 2017, Luo et al. (2017a) achieved a PCE of 15.34% by using GO-modified PEDOT:PSS. They had found that the device was less effective with the application of PEDOT:PSS (11.90%) layer in PSCs. It was also found that the devices fabricated with GO-modified PEDOT:PSS were much stable as compared to unmodified one and maintained PCE up to 83.5% of the initial PCE value after aging for 39 days. During the spin coating of the GO solution (ethanol in the GO solution), the hydrophilic PSS material can be partially removed from the surface. Energy levels of various HTMs used in PSCs and the highest achieved efficiency presented in Figs. 16 and 17, respectively.

Table 7 Performance of various spiro-OMeTAD HTM layer-based PSCs

Structure type	Device	PCE (%)	J_{sc} (mA cm^{-2})	V_{oc} (V)	FF	References	Year
Planar *p-i-n*	FTO/SnO_2/$FA_{0.83}MA_{0.17}Pb(I_{0.83}Br_{0.17})_3$/SWNTs:spiro-OMeTAD/Ag	18.9	22.10	1.14	0.75	Habisreutinger et al. (2014a)	2014
Planar *p-i-n*	FTO/TiO_2/PSK/Pristine- spiro-OMeTAD/Ag	18.7	22.90	1.12	0.73	Habisreutinger et al. (2014a)	2014
Planar *n-i-p*	FTO/TiO_2/PSK/HT1:HT2:spiro-OMeTAD/Al	18.04	21.40	1.11	0.73	Hua et al. (2016)	2016
Planar *p-i-n*	ITO/TiO_2/PSK/CuSCN: spiro-OMeTAD/Ag	18.02	21.01	1.06	0.77	Li et al. (2016a)	2016
Planar *p-i-n*	FTO/TiO_2/$FA_{0.85}Cs_{0.15}PbI_3$/spiro-OMeTAD with H_2SO_4 acid/Ag	17.7	21.6	1.06	0.78	Li et al. (2017a)	2017
Planar *p-i-n*	FTO/TiO_2/$FA_{0.85}Cs_{0.15}PbI_3$/spiro with H_3PO_4 acid/Ag	17.6	21.90	1.06	0.76	Li et al. (2017a)	2017
Planar *p-i-n*	FTO/TiO_2/$FA_{0.85}Cs_{0.15}PbI_3$/spiro-OMeTAD :CF3PA/Ag	17.5	21.6	1.04	0.78	Li et al. (2017a)	2017
Planar *p-i-n*	ITO/TiO_2/PSK/CuI: spiro-OMeTAD/Ag	16.67	21.52	1.06	0.73	Li et al. (2016a)	2016
Planar *p-i-n*	FTO/TiO_2/PSK/Ni-nanobelts: spiro-OMeTAD/Ag	16.18	21.64	1.02	0.73	Liu et al. (2017a)	2017
Planar *n-i-p*	FTO/TiO_2/PSK/Li-TFSI:tBP: spiro-OMeTAD/Ag	12.66	19.70	0.97	0.64	Di Giacomo et al. (2014)	2014
Planar *n-i-p*	FTO/TiO_2/PSK/F4-TCNQ:spiro-OMeTAD/Ag	10.59	18.72	0.94	0.48	Huang et al. (2016a)	2016

5.3 PSCs with Various ETM Layers and Their Device Performance

In the PSCs, the conventional compact ETL layer was used due to two different reasons, primarily to extract the photogenerated electrons from perovskite layer, and secondly, working as a hole blocking layer. This also indicates that the compact ETL layer should able to hinder the reverse movement of the electrons from the FTO substrate to the perovskite layer. It is important for the ETL layer to have continuous, uniform, and high transparent and thin structure for the better performance of the solar cells. The $MAPbBr_3$ and $MAPbI_3$-based PSCs efficiency were limited to 3.8% while using TiO_2 as an ETM layer. Later scientists have devoted themselves to improve the device performance and achieved an efficiency of more than 15%. Recently, Yang et al. have reported 19.3% efficient PSC using a polyethyleneimine (PEI) thin layer on TiO_2 as ETM fabricated in air (Zhou et al. 2014b) (Table 8).

Recently, metal oxides have gained much attention as a suitable ETL layer due to their good stability, high electron mobility, easy processability, and high transparency. Among various metal oxide materials, TiO_2, Al_2O_3, ZnO, SnO_2, SrO_2, etc., have shown potential in the perovskite cell device performance. TiO_2 is widely used in PSCs as an ETL layer. Ultra-thin TiO_2 could smooth the surface and keep the uniformity where the mesoscopic TiO_2 has better light scattering effect prolonging the incident light path. Park et al. (Lee et al. 2014) studied the effect of the crystal phase and morphology of the TiO_2 for the device performance of PSCs. They have reported that the rutile TiO_2 film was better than the anatase TiO_2 film because of the smooth surface of perovskite capping layer and lower conduction band position of the rutile TiO_2 film than that of the perovskite layer. Mali et al. have reported the use of transporting layer made by two TiO_2 layers, atom layer deposited (ALD) ultra-thin TiO_2 was deposited on top of the surface of one-dimensional TiO_2 nanorod arrays (Mali et al. 2015a). The device structure with 4.8 nm ALD passivated TiO_2 nanorod achieved the output PCE of 13.45%. In this method, it helped the light absorption and avoided the high-temperature processed $TiCl_4$ treatment. It is conventional that the nanorods, nanotubes, and nanofibers have shown better electron transport ability than nanoparticle films because of their directional charge transport properties. The PCE-based on TiO_2 nanorods grown in different method, with water-HCl solution was found to be higher than that with ethanol-HCl solution, which could be attributed to their special orientation, good optical properties, high conductivity, fast charge transfer, and reduced charge recombination (Wu et al. 2015b). TiO_2 is not suitable for flexible devices because it needs to be annealed at high temperature to get better crystallite (Table 9).

Al_2O_3 mesoscopic scaffold was used as an ETL layer and $MAPbCl_{3-x}I_x$ as the light absorber in PSCs (Lee et al. 2012). An optimal thick Al_2O_3 layer was fabricated at low temperature by atomic layer deposition (ALD) method. Introduction of Al_2O_3 layer effectively blocks the electron recombination between the perovskite and fluorine-doped tin oxide (FTO) layer and enhances the electron transport between the junction (Zhang et al. 2017b). It was observed that the perovskite cells with a

Table 8 Performance of various metal oxides used as ETM layer in PSCs

Fabrication method	ETL thickness (nm)	Device structure	PCE (%)	J_{sc} (mA-cm^{-2})	V_{oc} (V)	FF	References	Year
SC/SG	10/50	FTO/TiO_2/ZnO/$MAPbI_3$/spiro-OMeTAD/Au	17.2	20.8	1.08	0.71	Xu et al. (2015b)	2015
PA	40	FTO/c-TiO_2/$MAPbI_3$/spiro-OMeTAD/Au	15.2	20.5	1.06	0.70	Choi et al. (2016)	2016
TO	15	FTO/c-TiO_2/mp-TiO_2: $MAPbI_3$/spiro-OMeTAD/Au	15.1	22.0	1.09	0.63	Ke et al. (2014)	2014
TO	15	FTO/c-TiO_2/mp-TiO_2: $MAPbI_3$/spiro-OMeTAD/Au	15.1	22.0	1.09	0.63	Ke et al. (2014)	2014
TO	20	FTO/c-TiO_2/mp-TiO_2: $MAPbI_3$/spiro-OMeTAD/Au	14.8	21.3	1.09	0.64	Ke et al. (2014)	2014
TO	10	FTO/c-TiO_2/mp-TiO_2: $MAPbI_3$/spiro-OMeTAD/Au	14.6	22.2	1.09	0.60	Ke et al. (2014)	2014
TO	25	FTO/c-TiO_2/mp-TiO_2: $MAPbI_3$/spiro-OMeTAD/Au	14.2	21.1	1.09	0.62	Ke et al. (2014)	2014
ALD	10	FTO/c-TiO_2/$MAPbI_{3-x}Cl_x$/P3HT/Ag	13.6	24.3	0.98	0.57	Lu et al. (2015)	2015
ALD	10	FTO/c-TiO_2/$MAPbI_{3-x}Cl_x$/P3HT/Ag	13.6	24.3	0.98	0.57	Lu et al. (2015)	2015
ED	29	FTO/c-TiO_2/mp-TiO_2: $MAPbI_3$/spiro-OMeTAD/Au	13.6	20.0	1.00	0.68	Su et al. (2015)	2015
SC	60	FTO/c-TiO_2/mp-TiO_2: $MAPbI_3$/spiro-OMeTAD/Au	13.5	21.2	1.09	0.58	Ke et al. (2014)	2014

(continued)

Table 8 (continued)

Fabrication method	ETL thickness (nm)	Device structure	PCE (%)	J_{sc} (mA-cm^{-2})	V_{oc} (V)	FF	References	Year
DC	55	FTO/c-TiO_2/mp-TiO_2: $MAPbI_3$/spiro-OMeTAD/Au	12.8	20.1	0.88	0.73	Hong et al. (2015)	2015
ALD	50	FTO/c-TiO_2/mp-TiO_2: $MAPbI_3$/spiro-OMeTAD/Au	12.6	18.7	0.93	0.72	Wu et al. (2014)	2014
ALD	5	FTO/c-TiO_2/$MAPbI_{3-x}Cl_x$/P3HT/Ag	12.5	23.6	0.95	0.56	Lee et al. (2012)	2012
SC	40	FTO/c-TiO_2/$MAPbI_3$/spiro-OMeTAD/Ag	12.5	18.1	1.03	0.67	Choi et al. (2016)	2016
TO	5	FTO/c-TiO_2/mp-TiO_2: $MAPbI_3$/spiro-OMeTAD/Au	12.3	20.7	1.07	0.56	Ke et al. (2014)	2014
RFMS	60	FTO/c-TiO_2/$MAPbI_3$/spiro-OMeTAD/Ag	12.1	20.6	1.09	0.54	Chen et al. (2015e)	2015
SC	99	FTO/c-TiO2/mp-TiO_2: $MAPbI_3$/spiro-OMeTAD/Au	11.0	18.9	0.83	0.70	Hong et al. (2015)	2015
ED	14	FTO/NS-c-TiO_2/mp-TiO_2 :$MAPbI_3$/spiro-OMeTAD/Au	10.7	17.2	0.97	0.64	Choi et al. (2016)	2016
ALD	20	FTO/c-TiO_2/$MAPbI_{3-x}Cl_x$/P3HT/Ag	10.6	23.2	0.98	0.47	Lu et al. (2015)	2015
SC	60	FTO/c-TiO_2/mp-TiO_2: $MAPbI_3$/spiro-OMeTAD/Au	10.4	17.1	1.02	0.60	Su et al. (2015)	2015
SP	50	FTO/c-TiO_2/mp-TiO_2: $MAPbI_3$/spiro-OMeTAD/Au	8.8	17.4	0.87	0.58	Wu et al. (2014)	2014

(continued)

Table 8 (continued)

Fabrication method	ETL thickness (nm)	Device structure	PCE (%)	J_{sc} (mA-cm^{-2})	V_{oc} (V)	FF	References	Year
SC	n/a	FTO/c-TiO_2/$MAPbI_{3-x}Cl_x$/P3HT/Ag	8.7	18.4	0.92	0.51	Lu et al. (2015)	2015
SG	65	FTO/c-TiO2/$MAPbI_3$/spiro-OMeTAD/Ag	8.4	19.5	0.90	0.48	Wu et al. (2015c)	2015
SG	35	FTO/c-TiO_2/$MAPbI_3$/spiro-OMeTAD/Ag	8.1	14.6	0.93	0.60	Wu et al. (2015c)	
SC	50	FTO/c-TiO_2/mp-TiO_2: $MAPbI_3$/spiro-OMeTAD/Au	6.5	15.3	0.79	0.54	Wu et al. (2014)	2014
SG	25	FTO/c-TiO_2/$MAPbI_3$/spiro-OMeTAD/Ag	4.9	9.5	0.96	0.53	Wu et al. (2015c)	2015
SP/SC	80/22	FTO/TiO_2/SnO_2/$MAPbI_3$/spiro-OMeTAD/Au	2.2	11.2	0.62	0.32	Wang et al. (2015e)	2015
SG	95	FTO/c-TiO_2/$MAPbI_3$/spiro-OMeTAD/Ag	1.5	9.9	0.83	0.19	Wu et al. (2015c)	2015

SG—sol–gel; ALD—atomic layer deposition; TO—thermal oxidation, ALD—atomic layer deposition; ED—electrodeposition; DC—dip coating; NS—nanosheet; RFMS—radio frequency magnetron sputtering; PA—potentiostatic anodization; SC—spin coating; SG—sol–gel; SP—spray pyrolysis; TO—thermal oxidation

Table 9 Performance of PSCs based on TiO_2 as ETM layer in various device structures

Device architecture	Particles size (nm)	PCE (%)	J_{sc} (mA- cm^{-2})	V_{oc} (V)	FF	References	Year
FTO/c-TiO_2/mp-TiO_2:$MAPbI_3$/spiro-OMeTAD/Au	100a	18.4	22.7	1.05	0.77	Yang et al. (2016a)	2016
FTO/c-TiO_2/mp-TiO_2:$MAPbI_3$/spiro-OMeTAD/Au	50	17.2	21.6	1.05	0.76	Do Sung et al. (2015)	2015
FTO/c-TiO_2/mp-TiO_2:$MAPbI_3$/spiro-OMeTAD/Au	50	16.9	21.9	1.02	0.76	Yang et al. (2016a)	2016
FTO/c-TiO_2/mp-TiO_2:$MAPbI_3$/spiro-OMeTAD/Au	65	15.5	21.3	1.01	0.72	Do Sung et al. (2015)	2015
FTO/c-TiO_2/mp-TiO_2:$MAPbI_3$/spiro-OMeTAD/Au	40	15.2	21.5	1.03	0.70	Do Sung et al. (2015)	2015
FTO/c-TiO_2/mp-TiO_2:$MAPbI_3$/spiro-OMeTAD/Au	250a	15.0	19.4	1.05	0.74	Huang et al. (2016b)	2016
FTO/c-TiO_2/mp-TiO_2:$MAPbI_3$/spiro-OMeTAD/Au	30	14.7	20.1	0.99	0.74	Yang et al. (2016a)	2016
FTO/c-TiO_2/mp-TiO_2:$MAPbI_3$/spiro-OMeTAD/Au	30	14.3	21.6	1.00	0.67	Do Sung et al. (2015)	2015
FTO/c-TiO_2/mp-TiO_2:$MAPbI_{2.7}Br_{0.3}$/PTAA/Au	15	12.8	18.8	1.04	0.66	Sarkar et al. (2014)	2014
FTO/c-TiO_2/mp-TiO_2 :$MAPbI_{2.7}Br_{0.3}$/PTAA/Au	10	11.7	18.6	1.00	0.63	Sarkar et al. (2014)	2014

5 nm Al_2O_3 layer revealed a PCE of 16.2%, which is much higher than the device fabricated without Al_2O_3 layer (PCE ~ 11.0%) (Table 10).

In an inverted PSCs, ZnO and SnO_2 are usually used as an ETL layer because of their excellent electron mobility property. Low-temperature synthesized ZnO layer was used as a transporting layer in PSCs and the device exhibited a PCE value of 15.7% (Liu and Kelly 2014). SnO_2 has higher electron mobility and deeper conduction band than TiO_2. It was reported that SnO_2 shows better environmental stability with beneficial for charge transportation from perovskite layer to electron transport layer. SnO_2 layer is generally fabricated at low temperature, and the corresponding solar cells had achieved a PCE of 13%. Such devise showed a good device stability in ambient environment (Song et al. 2015a). A higher device efficiency of 17.2% was achieved by preparing the SnO_2 as a transporting layer. This layer was fabricated by spin coating of $SnCl_2{\cdot}H_2O$ precursor and annealing at 180 °C in the air (Ke et al. 2015a). A high efficiency of 19.9% was achieved by adopting solution-processed SnO_2 that was fabricated at the temperature of 150 °C (Jiang et al. 2016). WO_3 transporting layer are also exhibiting a good stability and higher mobility compared to TiO_2 layer. It was observed that WO_3-based devices are more sensitive to ambient moisture compared to TiO_2-based devices. The WO_3 ETM layer-based PSCs also degrade faster (Gheno et al. 2017). These devices showed better photovoltaic device performance when TiO_2 NPs were covered on WO_3 thin-film surface. Amorphous WO_x:TiO_x composites were fabricated at a relatively low temperature, and they were very effective as a ETL layer in PSCs. The addition of TiO_x and WO_x could raise the Fermi level and simultaneously suppress the non-radiative charge recombination at the perovskite interfaces (Wang et al. 2016d) (Table 11).

Doping in the metal oxides reduces the surface vacancies and other defects and reduces the charge recombination probability, which could exhibit better device performance due to their better electron mobility and suitable energy levels. The oxygen vacancies on TiO_2 surface are not beneficial for charge transport and also detrimental for efficient device performance (Leijtens et al. 2013). A 15% enhancement in short-circuit current density was observed when the device fabricated with Y^{3+}-doped TiO_2 layer. TiO_2 doped with Y^{3+} was used to modify the morphology of the perovskite active layer and improved the electron transfer properties (Qin et al. 2014b). Al-doped TiO_2 shown enhanced conductivity as the doping might remove the oxygen defects from the TiO_2 lattice causes the device stability (Pathak et al. 2014). Mg-doped TiO_2 demonstrated better optical properties and better energy level alignment with the perovskite active layer which provided better electron transportation (Wang et al. 2015). Nitrogen-doped ZnO (N:ZnO) nanorods also enhance the electron mobility and corresponding PSC devices exposed higher PCE (Mahmood et al. 2015b) (Table 12).

Fullerenes and their derivatives. Fullerene and its derivatives are commonly used as an ETL layer in inverted PSCs due to their band matching with perovskite layer and better electron transport ability. C60, phenyl-C60-butyric acid methyl ester (PC61BM), and indene-C60 bisadduct (ICBA) were firstly employed as ETL layers in $MAPbI_3$-based PSCs (Jeng et al. 2013). The open-circuit voltage of corresponding

Table 10 Performance of PSCs based on ZnO as ETM layer in various solar cells

Structure of ZnO ETL	Device structure	PCE (%)	J_{sc} (mA cm^{-2})	V_{oc} (V)	FF	References	Year
Compact	ITO/c-ZnO/$MAPbI_3$/PTAA/Au	17.7	20.1	1.13	0.78	Heo et al. (2016)	2016
Compact	ITO/c-ZnO/$MAPbI_3$/spiro-OMeTAD/Ag	15.7	20.4	1.03	0.75	Wang et al. (2015c)	2015
Compact	PEN/ITO/c-ZnO/$MAPbI_3$/PTAA/Au	15.6	18.7	1.10	0.76	Heo et al. (2016)	2016
Compact	FTO/c-ZnO/$MAPbI_3$/spiro-OMeTAD/Ag	14.2	19.5	1.03	0.71	Hadouchi et al. (2016)	2016
Compact	ITO/c-ZnO/$MAPbI_3$/spiro-OMeTAD/Ag	13.9	19.9	1.07	0.65	Song et al. (2015b)	2015
Nanowall	ITO/mp-ZnO: $MAPbI_3$/spiro-OMeTAD/Ag	13.6	18.9	1.00	0.72	Tang et al. (2016)	2016
Compact	ITO/c-ZnO/$MAPbI_3$/spiro-OMeTAD/MoO_3/Ag	13.4	22.4	1.04	0.57	Liang et al. (2014)	2014
Compact	FTO/c-ZnO/mp-Al_2O_3: $MAPbI_3$/spiro-OMeTAD/Ag	13.1	20.4	0.98	0.66	Dong et al. (2014)	2014
Compact	ITO/c-ZnO/PCBM/$MAPbI_3$/spiro-OMeTAD/MoO_3/Ag	12.2	18.2	1.00	0.67	Kim et al. (2014c)	2014
Nanorod	FTO/c-ZnO/mp-ZnO:$MAPbI_3$/spiro-OMeTAD/Au	11.1	20.1	0.99	0.56	Son et al. (2014)	2014
Compact	ITO/c-ZnO/$MAPbI_3$/spiro-OMeTAD/Ag	10.91	22.6	0.91	0.53	Zhang et al. (2015)	2015
Nanosheet + nanorod	FTO/c-ZnO/mp-ZnO:$MAPbI_3$/spiro-OMeTAD/Ag	10.4	18.0	0.93	0.62	Mahmood et al. (2014)	2014

(continued)

Table 10 (continued)

Structure of ZnO ETL	Device structure	PCE (%)	J_{sc} (mA cm^{-2})	V_{oc} (V)	FF	References	Year
Compact	ITO/c-ZnO/PEI/$MAPbI_3$/spiro-OMeTAD/Au	10.2	16.8	0.88	0.69	Cheng et al. (2015)	2015
Compact	PET/ITO/c-ZnO/$MAPbI_3$/spiro-OMeTAD/Ag	10.2	13.4	1.03	0.74	Wang et al. (2015c)	2015
Nanorod	FTO/c-ZnO/mp-ZnO:$MAPbI_3$/spiro-OMeTAD/Au	8.9	17.0	1.02	0.51	Kumar et al. (2013)	2013
Compact	ITO/c-ZnO/$MAPbI_3$/PTB7-Th/MoO_3/Ag	8.4	14.3	0.86	0.68	Kim et al. (2014c)	2014
Compact	ITO/c-ZnO/PCBM/$MAPbI_3$/spiro-OMeTAD/Au	6.4	16.0	0.88	0.46	Cheng et al. (2015)	2015
Nanorod	PET/ITO/c-ZnO/mp-ZnO:$MAPbI_3$/spiro-OMeTAD/Au	2.6	7.5	0.80	0.43	Kumar et al. (2013)	2013

Table 11 Performance of PSCs based on SnO_2 as ETM layer in various device structures

Material of c-ETL/mp-ETL	Device structure	PCE (%)	J_{sc} (mA cm^{-2})	V_{oc} (V)	FF	References	Year
SnO_2/—	FTO/c-SnO_2/C60-SAM/$MAPbI_3$/spiro-OMeTAD/Au	19.0	21.4	1.13	0.79	Wang et al. (2016e)	2016
SnO_2/—	FTO/c-SnO_2/$MAPbI_3$/spiro-OMeTAD/Au	18.2	22.8	1.10	0.73	Ma et al. (2017)	2017
SnO_2/—	FTO/c-SnO_2/PCBM: $MAPbI_3$/spiro-OMeTAD/Au	17.3	21.5	1.11	0.73	Chen et al. (2017d)	2017
SnO_2/—	FTO/c-SnO_2/$MAPbI_3$/spiro-OMeTAD/Au	17.2	23.3	1.11	0.67	Ke et al. (2015a)	2015
SnO_2/—	FTO/c-SnO_2/$MAPbI_3$/spiro-OMeTAD/Au	16.1	19.5	1.10	0.74	Ke et al. (2015b)	2015
TiO_2/—	FTO/c-TiO_2/$MAPbI_3$/spiro-OMeTAD/Au	15.2	22.5	1.06	0.64	Ke et al. (2015a)	2015
SnO_2/—	FTO/c-SnO_2($TiCl_4$)/$MAPbI_3$/spiro-OMeTAD/Au	14.7	20.0	1.00	0.67	Rao et al. (2015)	2015
—/SnO_2	FTO/mp-SnO_2-TiO_2:$MAPbI_3$/spiro-OMeTAD/Ag	14.2	21.2	1.02	0.66	Han et al. (2015)	2015

(continued)

Table 11 (continued)

Material of c-ETL/mp-ETL	Device structure	PCE (%)	J_{sc} (mA cm^{-2})	V_{oc} (V)	FF	References	Year
TiO_2/TiO_2	FTO/c-TiO_2/mp-TiO_2:$MAPbI_3$/spiro-OMeTAD/Ag	13.9	20.5	0.97	0.72	Dong et al. (2015b)	2015
TiO_2/—	FTO/c-TiO_2($TiCl_4$)/$MAPbI_3$/spiro-OMeTAD/Au	13.4	19.2	1.01	0.69	Rao et al. (2015)	2015
SnO_2/—	ITO/c-SnO_2/$MAPbI_3$/spiro-OMeTAD/Ag	13.0	19.5	1.08	0.62	Song et al. (2015a)	2015
TiO_2/—	FTO/c-TiO_2/$MAPbI_3$/spiro-OMeTAD/Ag	12.3	19.9	1.00	0.62	Song et al. (2015a)	2015
SnO_2/TiO_2	FTO/c-SnO_2/mp-TiO_2:$MAPbI_3$/spiro-OMeTAD/Ag	10.3	31.0	0.86	0.39	Dong et al. (2015b)	2015
SnO_2/SnO_2	FTO/c-SnO_2/mp-SnO_2($TiCl_4$): $MAPbI_3$/spiro-OMeTAD/Au	10.2	17.4	0.93	0.63	Li et al. (2015b)	2015
—/SnO_2	FTO/mp-SnO_2($TiCl_4$) + $MAPbI_3$/spiro-OMeTAD/Au	8.5	17.2	0.80	0.62	Zhu et al. (2015)	2015
SnO_2/—	FTO/c-SnO_2/$MAPbI_3$/CuSCN/Au	8.4	19.0	0.96	0.45	Murugadoss et al. (2016)	2016

Table 12 Performance of PSCs based on WO_3 as ETM layer in various device structures

Material	Device structure	PCE (%)	J_{sc} (mA-cm^{-2})	V_{oc} (V)	FF	References	Year
Fe_2O_3	FTO/c-Fe_2O_3/mp-Fe_2O_3/$MAPbI_3$/spiro-OMeTAD/Au	18.2	22.7	1.01	0.79	Luo et al. (2017b)	2017
Nb_2O_5	FTO/c-Nb_2O_5/$MAPbI_3$/spiro-OMeTAD/Au	17.1	22.9	1.04	0.72	Ling et al. (2015)	2015
CeO_2	FTO/CeO_2/PCBM/MAPbI3/spiro-OMeTAD/Ag	17.0	23.3	1.06	0.69	Wang et al. (2017b)	2017
SiO_2	FTO/c-TiO_2/mp-SiO_2: $MAPbI_{3-x}Cl_x$/spiro-OMeTAD/Ag	16.6	22.2	1.08	0.69	Yu et al. (2016)	2015
WO_3	ITO/c-WO_3/SAMs/$MAPbI_3$/spiro-OMeTAD/Ag	14.9	21.9	1.02	0.67	Hou et al. (2015)	2015
In_2O_3	FTO/c-In_2O_3/PCBM/$MAPbI_3$/spiro-OMeTAD/Au	14.8	20.1	1.08	0.69	Hu et al. (2017b)	2017
SiO_2	FTO/c-TiO_2/mp-SiO_2: $MAPbI_{3-x}Cl_x$/spiro-OMeTAD/Au	13.9	18.3	1.02	0.69	Lee et al. (2016)	2016
Al_2O_3	FTO/c-TiO_2/mp-Al_2O_3 :$MAPbI_2Cl$: spiro-OMeTAD/Ag	12.3	18.0	1.02	0.67	Ball et al. (2013)	2013
CdSe	ITO/CdSe/$MAPbI_3$/spiro-OMeTAD/Ag	11.7	17.4	0.99	0.68	Wang et al. (2014d)	2014
SiO_2	FTO/c-TiO_2/mp-SiO_2: $MAPbI_{3-x}Cl_x$/spiro-OMeTAD/Au	11.5	16.4	1.05	0.66	Hwang et al. (2014)	2014
WO_3	FTO/c-WO_3/NS-mp-WO_3($TiCl_4$): $MAPbI_3$/spiro-OMeTAD/Ag	11.2	17.0	0.87	0.76	Mahmood et al. (2015a)	2015
Fe_2O_3	FTO/c-Fe_2O_3/$MAPbI_3$/spiro-OMeTAD/Au	11.2	20.6	0.90	0.61	Hu et al. (2017b)	2017
CdS	ITO/CdS/$MAPbI_3$/spiro-OMeTAD/Au	11.2	16.1	1.05	0.66	Liu et al. (2015f)	2015
Al_2O_3	FTO/c-TiO_2/mp-Al_2O_3: $MAPbI_2Cl$:spiro-OMeTAD/Ag	10.9	17.8	0.98	0.63	Lee et al. (2012)	2015
ZrO_2	FTO/c-TiO_2/mp-ZrO_2: $MAPbI_3$/spiro-OMeTAD/Ag	10.8	17.3	1.07	0.59	Bi et al. (2013)	2013
Nb_2O_5	FTO/c-Nb_2O_5/mp-Al_2O_3: $MAPbI_{3-x}Cl_x$/spiro-OMeTAD/Au	10.3	12.8	1.13	0.72	Kogo et al. (2015)	2015
In2O_3	FTO/c-In_2O_3/$MAPbI_3$/spiro-OMeTAD/MoO_3/Al	9.9	19.7	0.95	0.53	Dong et al. (2016)	2016

(continued)

Table 12 (continued)

Material	Device structure	PCE (%)	J_{sc} (mA-cm^{-2})	V_{oc} (V)	FF	References	Year
WO_3	FTO/c-WO_3/MAPbIxCl3-x/spiro-OMeTAD/Ag	9.4	22.8	0.74	0.60	Wang et al. (2015a)	2015
WO_3	FTO/c-WO_3/NR-mp-WO_3($TiCl_4$) :$MAPbI_3$/spiro-OMeTAD/Ag	9.1	15.0	0.86	0.70	Mahmood et al. (2015b)	2015
Zn_2SnO_4	FTO/c-Zn_2SnO_4/mp-Zn_2SnO_4: MAPbI3/spiro-OMeTAD/Au	7.7	13.0	0.99	0.59	Mali et al. (2015b)	2015
$SrTiO_3$	FTO/c-TiO_2/mp-$SrTiO_3$: $MAPbI_{3-x}Cl_x$/spiro-OMeTAD/Au	7.6	14.9	0.93	0.55	Bera et al. (2015)	2015
Al_2O_3	FTO/c-TiO_2/mp-Al_2O_3: $MAPbI_2Cl$:spiro-OMeTAD/Au	7.2	12.8	0.93	0.61	Carnie et al. (2013)	2013
Zn_2SnO_4	FTO/c-Zn_2SnO_4/mp-Zn_2SnO_4: $MAPbI_3$/spiro-OMeTAD/Au	7.0	13.8	0.83	0.61	Oh et al. (2015)	2015
WO_3	FTO/c-WO_3/NP-mp-WO_3($TiCl_4$): $MAPbI_3$/spiro-OMeTAD/Ag	6.1	11.0.	0.83	0.67	Mahmood et al. (2015a)	2015
ZnS	ITO/ZnS/$MAPbI_3$/; spiro-OMeTAD/Au	1.0	2.25	0.98	0.44	Liu et al. (2015f)	2015

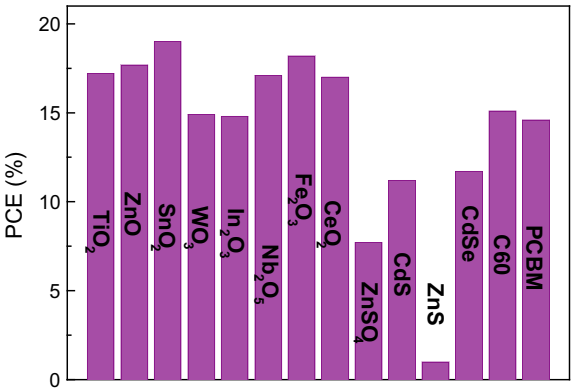

Fig. 19 Graphical representation of PCE values associated with various ETM materials used in perovskite solar cells

PSCs was achieved as 0.55, 0.65, and 0.75 V, respectively. The higher open-circuit voltage was achieved for ICBA because of its higher LUMO level compared to C60 and PC61BM. The PCE of fullerene-based PSCs is mostly related to electron mobility of these transport layers (C60, ICBA, PC61BM) (Liang et al. 2015). High mobility fullerene will beneficial for the charge transportation. Fullerene materials can also passivate the interfacial trap states of perovskite layer and reduce the energy barrier between the electrode and perovskite layer.

The new fullerene derivative C70-DPM-OE was synthesized by phenyl groups of diphenyl methano fullerene (DPM) moiety with oligoether chain (Xing et al. 2016). This oligoether chain can reduce the work function of the metal cathode and passivate the trap states of the perovskite layer. The device fabricated with C70-DPM-OE as an ETL have achieved the PCE of 16% which was much higher than the conventional PC61BM as electron transport layer. Another fullerene pyrrolidine derivative, *N*-methyl-2-pentyl-(Santra et al. 2013) fullerene pyrrolidine (NMPFP) was prepared by a simple solution process (Chen et al. 2019). The NMPFP thin film revealed a higher conductivity than the PC61BM thin film. The device fabricated with NMPFP as an ETL layer exhibited a PCE of 13.83% (Fig. 19; Table 13).

Doping in the fullerenes is a good way to improve the mobility and the device efficiency of PSCs. MAI-doped fullerene C60, exhibited dramatically increased conductivity by over 100 times (Bai et al. 2016). The iodide as a Lewis base anion in the MAI-dopant acted as an electron donor. When the iodide contacts fullerene after solvent drying, the electron density would redistribute from iodide to fullerene. Enhanced free electron density in fullerene presented a higher conductivity. The improved conductivity plays a significant role in boosting the device performance; the perovskite solar cell delivered an efficiency of 19.5% with a high fill factor of 80.6%.

Low-dimensional lead halide perovskites

In recent years, quasi-2D halide perovskites have intensively investigated as active layers in solar cells comparing with the conventional 3D perovskites structures. Smith et al. reported the solar cell from quasi-2D halide perovskites with a device structure

Table 13 Performance of PSCs based on fullerenes as ETM layer in various device structures

Material	Device structure	PCE (%)	J_{sc} (mA-cm^{-2})	V_{oc} (V)	FF	References	Year
TiO_2/IL	ITO/c-TiO_2/c-[BMIM]BF_4/$MAPbI_3$/PTAA/Au	19.6	22.8	1.12	0.77	Yang et al. (2016c)	2016
SnO_2/PCBM	FTO/c-SnO_2/PCBM/$MAPbI_3$/spiro-OMeTAD/Au	19.1	22.61	1.12	0.76	(Ke et al. 2016)	2016
TiO2/IL	FTO/c-TiO_2/c-[EMIM]PF_6/$MAPbI_3$/spiro-OMeTAD/Au	18.5	22.9	1.10	0.74	Wu et al. (2016)	2016
TiO_2/PCBM	ITO/c-TiO_2/PCBM/$MAPbI_3$/spiro-OMeTAD/Au	18.4	22.2	1.11	0.75	Kegelmann et al. (2017)	2017
TiO_2/PCBM	FTO/c-TiO_2/PCBM/$MAPbI_3$/spiro-OMeTAD/Au	17.9	21.0	1.11	0.77	Tao et al. (2015)	2015
TiO_2/graphene	FTO/c-TiO_2/mp-Gr:$MAPbI_3$/spiro-OMeTAD/Au	17.2	22.8	1.05	0.72	Tavakoli et al. (2016)	2016
TiO_2/IL	FTO/c-TiO_2/c-[EMIM]I/$MAPbI_3$/spiro-OMeTAD/Au	17.2	23.7	1.10	0.66	Wu et al. (2016)	2016
Graphene/TiO_2	FTO/c-Gr: TiO_2/Al_2O_3: $MAPbI_{3-x}Cl_x$/spiro-OMeTAD/Au	15.6	21.9	1.04	0.73	Wang et al. (2014e)	2014
PCBM	FTO/PEI/c-PCBM/$MAPbI_3$/PTAA/Au	15.3	21.8	0.98	0.72	Ryu et al. (2015)	2015
C60	ITO/c-C60/$MAPbI_3$/spiro-OMeTAD/Au	15.1	18.9	1.08	0.75	Ke et al. (2015c)	2015
IL	PET/ITO/c-BenMeIM-Cl/$MAPbI_3$/spiro-OMeTAD/Au	15.0	20.6	1.00	0.73	Yang et al. (2016b)	2016

(continued)

Table 13 (continued)

Material	Device structure	PCE (%)	J_{sc} (mA-cm^{-2})	V_{oc} (V)	FF	References	Year
C60	FTO/c-C60/$MAPbI_3$/spiro-OMeTAD/Au	14.5	19.6	1.07	0.69	Wojciechowski et al. (2015)	2015
PCBM	FTO/PCBM/$MAPbI_3$/spiro-OMeTAD/Au	14.6	20.4	1.03	0.69	Ke et al. (2016)	2016
IL	FTO/c-[EMIM]PF_6/$MAPbI_3$/spiro-OMeTAD/Au	14.2	21.6	1.05	0.63	Wu et al. (2016)	2016
PCBM	ITO/c-PC71BM/$MAPbI_3$/spiro-OMeTAD/MoO_3/Ag	13.9	20.5	1.08	0.63	Upama et al. (2017)	2017
PCBM	ITO/c-PC61BM/$MAPbI_3$/spiro-OMeTAD/MoO_3/Ag	12.7	23.9	0.84	0.63	Upama et al. (2017)	2017
IL	FTO/c-[EMIM]I/$MAPbI_3$/spiro-OMeTAD/Au	9.2	15.2	1.03	0.59	Wu et al. (2016)	2016
Graphene	FTO/c-Gr/Al_2O_3: $MAPbI_{3-x}Cl_x$/spiro-OMeTAD/Au	5.9	14.6	0.90	0.48	Wang et al. (2014e)	2014

of FTO/TiO_2/$(PEA)_2(MA)_2[Pb_3I_{10}]$/spiro-OMeTAD/Au and the device showed a PCE of 4.71% (Quan et al. 2016). In this work, the quasi-2D halide perovskite was obtained by mixing $C_6H_5(CH_3)_2NH_3I$ (PEAI), MAI and PbI_2 with a molar ratio of 2:2:3 and form a quasi-2D perovskite structure of $(PEA)_2(MA)_2[Pb_3I_{10}]$. The number of layers ($n$) was determined to be 3. It was observed that the decrease in dimension resulting an increase in the band-gap and exciton binding energy. It was shown that the devices were more stable when fabricated with quasi-2D halide perovskites and remained stable after 46 days, whereas the 3D halide perovskite started to decompose after 4–5 days, as it was evident from the XRD spectra. Improved stability of the perovskites was observed using all-inorganic halide perovskite ($CsPbX_3$), reported by many groups. $CsPbI_3$ having band-gap of 1.73 eV was the suitable for solar cells. Swarnakar et al. had grown α-$CsPbI_3$ perovskite QDs which was found stable for several months in ambient air (Fang et al. 2015). These QDs were also used as active layer in PSCs and deposited on TiO_2/FTO substrates. The $CsPbI_3$ QDs-coated substrates were then immersed in saturated methyl acetate (MeOAc) solution for several times to yield a desired thick perovskite thin film. Such QDs-based solar cells revealed a PCE of 10.77% with a V_{oc} of 1.23 eV and fill factor of 0.65. More recently, Sanehira et al. boosted the PCE up to 13.43% by using $CsPbI_3$ QDs in the device and resulted in enhancement of charge carrier mobility of QD films (Sanehira et al. 2017).

Mixed cations

FA/MA-Cs mixed-cation perovskite

The α-$Cs_xFA_{1-x}PbI_3$ perovskite layer was fabricated via a regular one-step solvent engineering method with different Cs/FA ratios. Such thin films showed comparatively more stable and do not transform from α-phase to δ_H-phase (Li et al. 2016b). $FA_{0.9}Cs_{0.1}PbI_3$ thin-film-based PSCs displayed both the superior stability and efficiency (16.5%) in solar cell devices compared to pure $FAPbI_3$ perovskite (Lee et al. 2015c). Later, Yi et al. had achieved the improved PCE to 18% by replacing both a small fraction of the iodide and bromide anions as $Cs_{0.2}FA_{0.8}PbI_{2.84}Br_{0.16}$. McMeekin et al. also reported a FA/Cs mixed cation perovskite of $FA_{0.83}Cs_{0.17}PbI_3$ with some added bromide achieve a band-gap of 1.75 eV (Yi et al. 2016). The structure of perovskite $FA_{0.83}Cs_{0.17}Pb(I_{0.6}Br_{0.4})_3$ was used in a solar cell and achieved an open-circuit voltage 1.2 volts with PCE of over 17%. The mixed perovskites of $FA_{0.83}Cs_{0.17}Pb(I_{0.6}Br_{0.4})_3$ absorber layer was used in a *p-i-n* solar cell structure where *n*-doped C60 used as an electron collecting layer where 80% of the original efficiency sustained after 650 h under ambient air without encapsulation and stable over 3400 h with encapsulation (Wu et al. 2016). MA cation had also been alloyed with Cs^+ to form the MA/Cs mixed perovskites. Chio et al. represented the use of perovskite containing Cs^+ and MA^+ with [6,6]-phenyl-C60 butyric acid methyl ester (PCBM) as an electron acceptor (Choi et al. 2014). 10% of Cs^+ ions doping in $MAPbI_3$ perovskite improved the efficiency from 5.51 to 7.68%.

Ternary cation perovskite

The successful exhibition of binary cation perovskites with enhanced performance and stability might open a new way to use of ternary cation perovskite using MA^+, FA^+, and Cs^+ cations-based perovskite in solar cells. Saliba et al. first reported the triple cation perovskite with FA/MA/Cs where Cs^+ ions could improve the film quality for FA/MA mixture (Saliba et al. 2016a). 5% CsI was incorporated into the mixed-cation perovskite which was known as $(FAPbI_3)_{0.83}(MAPbBr_3)_{0.17}$ to suppress non-perovskite phase and enhanced the crystallization process with a highly stabilized PCE (21.1%) and stability was reported. The solar cells still maintained an efficiency at 18% after 250 h. Saliba et al. investigated several alkali cations and found the radii of Rb^+ was only slightly smaller than the favorable cations of Cs^+, MA^+, and FA^+. They have successfully alloyed a small amount of RbI (about 5–10%) into Cs/MA/FA mixed-cation perovskite to achieve a record efficiency of 21.6% on small areas and 19.0% on large area (0.5 cm^2) under AM 1.5G. The addition of Rb^+ ions suppresses the formation of unwanted yellow phase of Cs- or FA-based perovskite structures and improves the stability of solar cells. These devices based on Rb/Cs/MA/FA perovskite were found 95% efficient from its initial value after 500 h at 85 °C under continuous illumination, which could meet the industrial standards for reliable solar cells (Saliba et al. 2016b). However, more than 10% RbI addition into the mixed-cation perovskite resulted in a Rb-rich phase and was destructive to the solar cells.

Mixed Cation to stabilize the Pb-Sn alloy metal halide perovskite

Due to the similar electronic structure and the similar ionic radii of Sn^{2+} (1.35 Å) to Pb^{2+} (1.49 Å), tin is a useful candidate for the application of lead-free perovskites. Hao et al. had reported the optical band-gap 1.3 eV in $MASnI_3$ with high absorption at 950 nm, which is ideal for solar cell application (Hao et al. 2014a). It was found that the presence of Pb and Sn in methylammonium iodide perovskite showed a narrower band-gap of 1.3 eV which extend the absorption onset to the near-IR region (Hao et al. 2014b; Ogomi et al. 2014; Im et al. 2015). According to Shockley–Queisser theory, the PCE of approximately 30% can be achieved by replacing 15% Pb^{+2} by Sn^{+2} ions in the perovskite structure (Anaya et al. 2016). Pure Sn-based PSCs had shown relatively low PCE apart from that their tendency of oxidizing to Sn^{+2} to Sn^{+4} state damage the perovskite structure. Zhao and co-workers had found the lesser oxidation probability observed for Sn atom in $FASnI_3$ than in $MASnI_3$ due to the stronger hydrogen bond in $FASnI_3$ (Wang et al. 2016f). Liao et al. had used the mixed cation (FA/MA) and (Sn/Pb) perovskite materials in the inverted device structure by using $FASnI_3$ and $MAPbI_3$ precursor solutions (Liao et al. 2016). The as-fabricated device structure with this perovskite ITO/PEDOT:PSS/$(FASnI_3)_{0.6}(MAPbI_3)_{0.4}$/C60/BCP/Ag showed a PCE of 15.08%. The $MA_{0.5}FA_{0.5}Pb_{0.75}Sn_{0.25}I_3$ PSCs were fabricated using one-step spin-coating method and resulted in a PCE of 14.19% with a great stability (Yang et al. 2016d). The fabricated solar cells maintained PCE of 94% of its initial value after 30 days when kept in an inert atmosphere and retained 80% of initial PCE value after 12 days when exposed to an ambient atmosphere (30–40% R.H.) (Table 14).

Table 14 Performance of PSCs based on various perovskite active layer

Device architecture	Thickness (nm)/E_g (eV)	PCE (%)	J_{sc} (mA cm^{-2})	V_{oc} (V)	FF	References	Year
FTO/c-TiO_2/mp-TiO_2/$Rb_{0.05}Cs_{0.05}(FA_{0.83}MA_{0.17})_{0.90}Pb(I_{0.83}Br_{0.17})_3$/PTAA/Au	~500/1.63	21.8	22.8	1.18	0. 81	Duong et al. (2017)	2017
FTO/c-TiO_2/mp-TiO_2/(FA/MA)$Pb(I/Br)_3$/spiro-OMeTAD/Au	~400c/1.6	20.8	24.6	1.16	73	Bi et al. (2016)	2016
FTO/c-TiO_2/mp-TiO_2/$FA_{4/6}MA_{2/6}Pb(I_{5/6}Br_{1/6})$/spiro-OMeTAD/Au	~400c/1.64	20.67	23.7	1.14	0.76	Jacobsson et al. (2016)	2016
FTO/c-TiO_2/mp-TiO_2/$Rb_{0.05}FA_{0.8}MA_{0.15}PbI_{2.55}Br_{0.45}$/spiro-OMeTAD/Au		19.6	22.5	1.17	0.75	Zhang et al. (2017c)	2017
FTO/c-TiO_2/mp-TiO_2/$Rb_{0.05}Cs_{0.10}FA_{0.85}Pb(I_{0.83}Br_{0.17})_3$/spiro-OMeTAD/Au		19.3	22.3	1.16	0.75	Saliba et al. (2016b)	2016
FTO/c-TiO_2/mp-TiO_2/$Cs_{0.05}(FA_{0.83}MA_{0.17})_{0.95}Pb(I_{0.83}Br_{0.17})_3$/spiro-OMeTAD/Au	500/1.6	19.2 ± 0.91	22.69 ± 0.75	1.132 ± 0.025	0.75 ± 0.18	Saliba et al. (2016a)	2016
FTO/SnO_2/C_{60}/$Cs_{0.17}FA_{0.83}Pb(I_{0.6}Br_{0.4})$/spiro-OMeTAD/Au		18.3	23	1.06	0. 75	Wang et al. (2017c)	2017
ITO/PTAA/$MA_{0.6}FA_{0.4}PbI_3$/ICBA/C60/BCP/Cu	1.55	18.3	23	1.03	0.77	Deng et al. (2016)	2016
FTO/c-TiO_2/mp-TiO_2/$MA_{0.91}Cs_{0.09}PbI_3$/spiro-OMeTAD/Au	~400	18.1	22.57	1.06	0.76	Niu et al. (2017)	2017
FTO/c-TiO_2/mp-TiO_2/$Cs_{0.1}FA_{0.8}MA_{0.1}Pb(I_{0.83}Br_{0.17})_3$/spiro-OMeTAD/Au	~500	18.1	21.5	1.16	0.73	Matsui et al. (2017)	2017
FTO/c-TiO_2/mp-TiO_2/$Rb_x(FAPbI_3)_{1-y}(MAPbBr_3)_y$/PTAA/Au		17.68 ± 0.91	22.86 ± 0.37	1.12 ± 0.01	0.70± 0.19	Duong et al. (2016)	2016

(continued)

Table 14 (continued)

Device architecture	Thickness (nm)/E_g (eV)	PCE (%)	J_{sc} (mA cm^{-2})	V_{oc} (V)	FF	References	Year
FTO/c-TiO_2/mp-TiO_2/$(FAPbI_3)_{0.85}Pb(MABr_3)_{0.15}$/spiro-OMeTAD/Au	mp-TiO_2 with PVSK infiltrared(∼200 nm) + capping layer (∼650 nm)/1.57−1.58	17.6	22.5	1.13	0.69	Sveinbjornsson et al. (2016)	2016
FTO/Nb-TiO_2/$FA_{0.84}MA_{0.16}Pb(I_{0.84}Br_{0.16})$/spiro-OMeTAD/Au	∼500	17.6	23.4	1.00	0.74	Chen et al. (2017f)	2017
ITO/PEDOT:PSS/$MA_{0.80}FA_{0.20}PbI_{3-y}Cl_y$/PC61BM/C60/LiF/Ag	∼280/1.58	17.45	21.55 ± 0.55	1.10 ± 0.01	0.75	Isikgor et al. (2016)	2016
FTO/c-TiO_2/mp-TiO_2/Rb(5%) in$FA_{0.75}(MA_{0.6}Cs_{0.4})_{0.25}PbI_2Br$/PTAA/Au	mp-TiO_2 with PVSK infiltrated (∼180 nm) + capping layer (∼400 nm)/1.73	17.4	18.3	>1.1		Duong et al. (2017)	2017
FTO/c-TiO_2/mp-TiO_2/$Cs_{0.2}FA_{0.8}PbI_{2.84}Br_{0.16}$/spiro-OMeTAD/Au	1.49	17.35	21.9	1.07	0.74	Yi et al. (2016)	2016
FTO/c-TiO_2/mp-TiO_2/$Cs_{0.2}FA_{0.8}PbI_{2.84}Br_{0.16}$/spiro-OMeTAD/Au	1.58	17.35	21.9	1.073	0.74	Yi et al. (2016)	2016
FTO/SnO_2/$Cs_{0.1}FA_{0.8}MA_{0.0.1}Pb(I_{0.83}Br_{0.17})_3$/spiro-OMeTAD/Au		17.3	22.4	1.13	0.68	Matsui et al. (2017)	2017
FTO/c-TiO_2/mp-TiO_2/$Rb_{0.05}FA_{0.95}PbI_3$/spiro-OMeTAD/Au	∼480 (capping layer)/1.53	17.16	23.93	1.07	0.67	Park et al. (2017)	2017
FTO/SnO_2/$PC_{60}BM/FA_{0.83}Cs_{0.17}Pb(I_{0.6}Br_{0.4})_3$/spiro-OMeTAD/Ag	1.74	17.1	19.4	1.2	0.75	McMeekin et al. (2016)	2016
FTO/c-TiO_2/$MA_{0.7}FA_{0.3}PbI_3$/spiro-OMeTAD/Ag	38 ± 9 1.54	17.02	22.03	1.03	0.75	Li et al. (2016d)	2016

(continued)

Table 14 (continued)

Device architecture	Thickness (nm)/E_g (eV)	PCE (%)	J_{sc} (mA cm^{-2})	V_{oc} (V)	FF	References	Year
FTO/c-TiO_2/$Cs_{0.1}FA_{0.9}PbI_3$/spiro-OMeTAD/Ag (Au)	1.55	16.5	23.5	1.06	0.66	Lee et al. (2015a)	2015
FTO/c-TiO_2/C60/$MA_{1-x}FA_xPbI_3$/spiro-OMeTAD/Au	340	16.48	22.51	1.00	0.74	Chen et al. (2017e)	2017
FTO/c-TiO_2/$Cs_xFA_{1-x}PbI_3$/spiro-OMeTAD/Ag		16.4	20.4	1.09	0.74	Liu et al. (2017c)	2017
FTO/c-TiO_2/mp-TiO_2/$Rb_{0.05}FA_{0.95}PbI_3$/spiro-OMeTAD/Au		16.2	23.8	1.03	0.66	Zhang et al. (2017c)	2017
FTO/c-SnO_2/C60-SAM/$Cs_{0.2}FA_{0.8}PbI_3$/spiro-OMeTAD/Au	435	16.18 ± 0.50	21.73 ± 0.51	1.03 ± 0.02	0.72 ± 0.12	Yu et al. (2016)	2016
FTO/c-TiO_2/$Cs_{0.15}FA_{0.85}PbI_3$/spiro-OMeTAD/Ag	1.52	16.1	20.39	1.06	0.74	Li et al. (2016c)	2016
FTO/c-TiO_2/mp-TiO_2/$FAPbI_3$-MABr/spiro-OMeTAD/Au	~450	15.98	22.17	1.07	0.67	Zheng et al. (2016)	2016
FTO/c-TiO_2/mp-TiO_2/$(MAPbI_3)_{1-x}(CsPbBr_3)_x$/spiro-OMeTAD/Au	360	15.9 ± 0.52	20.9 ± 0.42	1.07 ± 0.01	0.71 ± 0.02	Niu et al. (2016)	2016
FTO/c-TiO_2/mp-TiO_2/$MA_xFA_{1-x}PbI_3$/WO_3/Ag	1.57	15.86	20.85	1.04	0.73	Kim et al. (2016)	2016
FTO/c-TiO_2/mp-TiO_2/$Cs_{0.2}FA_{0.8}PbI_3$/spiro-OMeTAD/Au	1.56	15.69	21.5	1.02	70.1	Yi et al. (2016)	2016
FTO/c-TiO_2/mp-TiO_2/$MA_{0.25}FA_{0.75}PbI_3$/spiro-OMeTAD/Ag	300	15.51	21.10	1.03	0.71	Qin et al. (2014b)	2014
FTO/NiO/$Cs_{0.15}FA_{0.85}PbI_3$/PC61BM/PFNBr/Ag		15.38	20.81	1.04	0.71	Huang et al. (2017)	2017

(continued)

Table 14 (continued)

Device architecture	Thickness (nm)/E_g (eV)	PCE (%)	J_{sc} (mA cm^{-2})	V_{oc} (V)	FF	References	Year
ITO/NiO/$FA_{0.83}Cs_{0.17}Pb(I_{0.6}Br_{0.4})_3$/LiF/$PC_{60}BM$/$SnO_2$/ZTO/ITO/LiF/Ag	1.63	14.5	18.7	0.98	0.79	Bush et al. (2017)	2017
FTO/c-TiO_2/mp-TiO_2/(FA/MA)$Pb(I/Br)_3$/spiro-OMeTAD/Au	mp-TiO_2 with PVSK infiltrated (~150 nm) + capping layer (~400 nm)	14.5	21	1.01	0.69	Reyna et al. (2016)	2016
FTO/c-TiO_2/mp-TiO_2/$MA_{0.6}FA_{0.4}PbI_3$/spiro-OMeTAD/Au		14.23	20.87	0.98	69.97	Pellet et al. (2014)	2014
FTO/ZnO/$MA_{0.6}FA_{0.4}PbI_3$/spiro-OMeTAD/Ag	315	13.4	22.39	0.98	0.61	Mahmud et al. (2016)	2016
FTO/c-TiO_2/mp-TiO_2/$MA_{0.6}FA_{0.4}PbI_3$/spiro-OMeTAD/Au	~300/1.53	13.4	18.15	1.03	0.72	Pellet et al. (2014)	2014
ITO/PEDOT:PSS/$MA_{0.6}FA_{0.4}PbI_3$/PC61BM/Ag		13.28 ± 0.37	20.96 ± 0.14	0.98 ± 0.01	0.65 ± 0.12	Chen et al. (2016g)	2016
ITO/PEDOT:PSS/$MA_{0.6}FA_{0.4}PbI_3$/PC61BM/Ca/Ag	~300	13.0	18.95	0.94	0.73	Liu et al. (2015g)	2015
ITO/PEDOT:PSS/$(FAPbI_3)_{0.8}(MAPbBr_3)_{0.2}$/C60/BCP/Ag	280	12	20.6	0.88	0.66	Chen et al. (2016h)	2016
ITO/PEDOT:PSS/$(FAPbI_3)_{0.8}(MAPbBr_3)_{0.2}$/C60/BCP/Ag		11.8 ± 0.20	20.1 ± 0.5	0.87 ± 0.01	0.66 ± 0.12	Matsui et al. (2017)	2017
FTO/c-TiO_2/$MA_{0.13}FA_{0.87}PbI_3$/spiro-OMeTAD/Au	1.52 ± 0.02	8.73	15.7	1	0.56	Wang et al. (2014c)	2014
ITO/PEDOT:PSS/$MA_{0.9}Cs_{0.1}PbI_3$/PC60BM/Al		7.68	10.10	1.05	0.73	Choi et al. (2014)	2014
FTO/c-TiO_2/$(MAPbI_3)(FAPbI_3)$/Au	1.53–1.54	4.0	9.58	0.77	0.54	Aharon et al. (2015)	2015

6 Challenges of PSCs

6.1 Hysteresis

The current–voltage hysteresis behavior in PSCs appeared due to several internal factors, such that (a) hysteresis is mostly depending on the perovskite material, (b) selective contact materials, i.e., HTM, ETM, play crucial roles in this behavior, including the material and the morphology, and (c) the typical charge generation/recombination processes (≈ns) in PSCs (Snaith et al. 2014). These effects cause non-uniform current flow in forward and reverse biasing condition. The shape of measured J–V curves and corresponding device efficiency hugely depends on scan direction, light source, delay in measurement time, and voltage bias conditions before measurement. In last few years, different mechanisms have been proposed to be responsible such hysteresis effects, like, ferroelectricity, charge trapping/detrapping, and ionic migration. Out of them ionic migration seems to appear as dominative factor.

Ferroelectricity. Ferroelectricity of a material depends on the hysteretic swapping of ferroelectric domains in an external electric field. Even though the $MAPbI_3$ perovskite crystal structure possesses centrosymmetric tetragonal space group, however the reorientation of the organic cations and the distortion of the $[PbI_6]^{4-}$ cages can result in a polarization (Sherkar and Jan Anton Koster 2016). Secondly, the ability of the perovskite crystal structure to switch this polarization by an external field can originate the hysteresis effect. Several research groups have confirmed the polarization switching in both amplitude and phase by using piezoelectric force microscopy (PFM) in the perovskite materials (Chen et al. 2015f; Coll et al. 2015).

Charge trapping/detrapping. Generally, the perovskite thin films are grown via low-temperature solution process that creates defects in the perovskite crystal structure, which impact the charge separation/recombination and charge transport through the device (Ono and Qi 2016). Spectroscopic characterization confirms that these traps are mostly accumulated at the interfaces or surface, where the periodic crystalline structure is not liable (Wu et al. 2015d; D'Innocenzo et al. 2014). Such defects can be passivated by several methods and can significantly improve the device performance and decreases the hysteresis. Luminescence characteristics confirmed that oxygen exposure led to a significant reduce the density of the trap state in the perovskite material (Motti et al. 2016). Lewis bases treatment to the perovskite thin films also can reduce the recombination centers and enhance the photoluminescence intensity and lifetime (deQuilettes et al. 2015). It has been observed that by using PCBM or other organic molecules either in grain boundary or an interlayer or mixed as bulk heterojunction structure can able to passivate defect states and correspondingly reduce the hysteresis effect (Meng et al. 2016).

Ionic migration. Several experimental observations point out that the ionic migration through the perovskite thin films is a dominant factor for the origin of hysteresis.

Mobile charge carriers not only impact on the hysteresis effect in J–V curves but also influence the emission properties of the perovskites (e.g., photoluminescence, electroluminescence, blinking), and they induce capacitive effects (Richardson et al. 2016; deQuilettes et al. 2016). In an external electric field, charge carriers move toward the opposite interfaces (perovskite/ETL or perovskite/HTL) (De Bastiani et al. 2016). These accumulations of charge carriers at the interfaces result in change of the internal field and a modulation of interfacial barriers which ultimately results in the hysteretic behavior. For an example, the migrating ions in $MAPbI_3$ are MA^+, I^-, H^+ ions. These ions originate during growth of perovskites at low-temperature fabrication and include vacancies like Schottky defects, interstitial defects, and Frenkel defects (Azpiroz et al. 2015; Yuan and Huang 2016).

Suppression of hysteresis. It is very important to reduce the hysteresis effects in PSCs. It will be very beneficial to not only reduce the hysteresis but also to increase the long-term stability of PSC devices. There are several ways to reduce defect states as: (1) reducing the concentration of defects/ions in the precursor solution, (2) hindering the motion of these ions from the perovskite octahedral crystal structure, and (3) reducing the interfacial barriers and accelerating the interfacial charge-transfer process (Gangishetty et al. 2016). Larger crystal grains possess very few defects that are the source of mobile ions. It has been observed that if the surface recombination in the material is low and diffusion length is long, then the hysteresis is weak. Improved crystallinity, better fabrication process, and improved contacts are going to reduce hysteresis effects. If the perovskite films deposited on mesoporous TiO_2 layers, forms a uniform, compact and dense perovskite grains, leading to negligible hysteresis (Yang et al. 2016e).

6.2 Stability

Moisture. Water molecules are strongly interacting with perovskite molecules as the perovskite structure itself is soluble in water. In the presence of limited humidity at the atmosphere during perovskite thin-film processing time can improve the thin-film morphology and can lead to improve solar cell device performance. However, when the PSCs are exposed to the atmosphere with a relatively high humidity, a detrimental device performance was occurred. So, it is very important to understand the effect of moisture on perovskite materials to achieve highly stable PSCs that can last over a decade. It has been observed that if the $MAPbI_3$ perovskite film is exposed to a warm humid air at room temperature, the perovskite film decomposes into hydroiodic acid (soluble in water), solid PbI_2, and CH_3NH_2 (either released as a gas or dissolved in water) (Frost et al. 2014). This process is irreversible and in results the device degrades. When the films are exposed to cool humid air, then water is slowly incorporated into the crystal and results in homogeneous uniform films throughout the sample. In this case, the process is reversible in films and enhances the performance of solar cells (Hao et al. 2014c). When spiro-OMeTAD is used as

HTM for PSCs, these results in many pinholes that poorly protect the perovskite against the atmospheric water and forms PbIOH as a degradation product (Ono et al. 2015; Chen et al. 2017g). Synthesis of hydrophobic HTMs forms pinhole-free films and improves device performance and stability (Kwon et al. 2014). To improve the moisture stability of PSCs, the encapsulation of the devices is a key for long-term stability.

Heat. Heating in the perovskite thin films can result in the internal crystal structural changes. For an example, $MAPbI_3$ perovskites undergo a reversible crystal-phase transition between tetragonal and cubic symmetry in the temperature range of 54–57 °C (Baikie et al. 2013). Changes to the electronic band structure can modify the band alignment and potentially reduce the photovoltaic performance. Additionally, cycling between the two crystal phases during the day and night cycles is likely to lead to material fatigue and shorter device lifetimes. $CsPbI_3$ is a large band-gap of 2.8 eV at room temperature and has a cubic phase with a band-gap of 1.7 eV at high temperatures (Giesbrecht et al. 2016). $FAPbI_3$ has a band-gap of 2.2 eV also which possess hexagonal structure at room temperature, similar to the PbI_2 lattice, so-called δ-phase. However, depending on the growth temperature, $FAPbI_3$ can also be crystallized in the α-phase with trigonal symmetry (Binek et al. 2015). It is very difficult to find a suitable synthesis route such that the solar cells remain stable at normal operating conditions. To overcome this issue, Cs^+, MA^+, FA^+ and halides were mixed to form cubic structure at room temperature and allow the band-gap tuning, which enhance the device stability of the device.

Mixed-Halide, mixed-cation perovskites. The intrinsic stability of the perovskite crystal structures has been studied immensely with the DFT calculations and experimental observations. It has been observed that $MAPbI_3$ is very unstable in the normal atmospheric conditions while $MAPbCl_3$ is the most stable (Buin et al. 2015). Partially substituting the I^- ions with Br^- or Cl^- ions can improve the stability of the perovskite structure compared to the pure $MAPbI_3$ perovskite material. However, under illumination condition $MAPb(Br_xI_{1-x})_3$ mixed-halide perovskites undergo a reversible phase separation into I^- and Br^- ion-rich domains (Hoke et al. 2015). This creates recombination centers inside the film, which limits the open-circuit voltage. This also leads to a poor photovoltaic device performance and poor long-term stability. However, in a mixed-cation, mixed-halide perovskite ($Cs_yFA_{1-y}Pb(Br_xI_{1-x})_3$), we suppress unwanted halide segregation. Small content between $0.10 < y < 0.30$ of Cs^+ cations inside the perovskite structure shows a high crystallinity and good optoelectronic properties (Rehman et al. 2017). Upon adding, FA^+ cations significantly improve the solar cells performance and good long-term stability under continuous illumination condition. Rb^+ cations are also an alternative cation that further increasing the photovoltaic performance (Saliba et al. 2016c).

Defect states: Another main reason of perovskite instability is the defect chemistry of perovskite structure. Since perovskite materials are ionic in nature, their solution-processed growth process enables formation of defect states. That defect states generally form at the thin-film surfaces or the grain boundaries of perovskite films. Point

defects, such as organic cation (MA/FA) vacancies, and halide anion (I/Br) vacancies, can easily develop in the perovskite structure due to their low formation energies. These defect states create shallow electronic energy levels close to the band edges and resulted in lower device performance in PSCs. Such defects also play a significant role in chemical degradation of the perovskite materials and leads to instability in PSCs (Wang et al. 2016g). Ion vacancies can diffuse into the perovskite crystals and also trigger cations and anions to diffuse at the surfaces and grain boundaries. Therefore, systematic control of defect states is essential during perovskite thin-film growth process that can enhance PSCs device efficient and stability.

There are several strategies to reduce these unwanted defect states in perovskite films (Noel et al. 2014; Abdi-Jalebi et al. 2018; Saidaminov et al. 2018; Yang et al. 2020). Firstly, use of excess MA/FA organic cations during film growth or after the thin-film annealing process can compensate with thermally evaporated organic cations. Secondly, introduction of larger organic molecules: such as phenethylamine, polyethylenimine, and trifluoroethylamine, which are difficult to evaporate. Thirdly, guanidinium, an organic cation that connect with perovskite structure via forming hydrogen bonds, has been used to suppress the formation of iodide vacancies. Fourthly, addition of KI into perovskites passivating iodine vacancies and small ions (Cl and Cd) doped into the perovskite lattice also suppress the formation of halide vacancies via lattice strain relaxation. Such perovskite films exhibited better device efficiency and stability compared to pristine PSCs.

7 Future Outlooks

In the last decade, organometal halide perovskites (OHPs) have emerged as a promising alternative to the existing commercially available solar cells. High photovoltaic efficiency, low materials cost, solution-phase deposition, low-temperature processing steps, and long-range crystallinity sets the OHPs apart from the contemporary emerging solar cell technologies (Petrus et al. 2017). Their performance has rapidly increased from 3.8% in 2009 to 23.7% in 2019, thanks to their high absorption coefficient, high carrier mobility, and long carrier lifetime. The commercial success of the PSCs, however, depends on their long-term stability, high-efficiency large-area module formation, and the toxicity issue related to the use of lead in the perovskite semiconductors (Petrus et al. 2017; Asghar et al. 2017).

Compositional engineering has been applied to a great effect to minimize the crystal strain in the perovskite crystals, which has improved their thermal stability significantly (Jeon et al. 2015b). The use of hydrophobic surfactants in the development of 2D/3D perovskite crystal has increased its moisture resistance considerably in solid films (Grancini et al. 2017). In PSCs, efficiency, stability, and J–V hysteresis are closely correlated. Interfacial defect and bulk recombination through intermediate trap states are adversely affecting the solar cell properties. Interfacial engineering at both ETL/perovskite and HTL/perovskite and grain boundary engineering are believed to be the right research direction toward stable and high-efficiency PSCs

(Grancini et al. 2017). Further, hydrophobic ETL and HTL layer development would act as a deterrent toward moisture ingress to the sensitive perovskite layer. Better encapsulation may also be critical to improve the PSCs device stability and it is very essential to resolve this stability issue for further industrial commercialization (Jena et al. 2019).

Large-area compatible roll-to-roll processing needs to be developed for smooth, reproducible, and pinhole-free deposition of perovskite and other solution-processed layers (ETL/HTL) for large-scale production of PSCs. A significant amount of research efforts have been made in this direction in recent years, resulting in a mini-module with a certified efficiency of 12.1% with an aperture area >36 cm^2 (Chen et al. 2017h). The efficiencies of perovskite solar cell modules are still notably lagging behind the small-area cells. A loss in solar cell performance in large-area modules is observed due to several issues like higher series resistance, lower shunt resistance, non-uniform surface morphology, pinholes, and unavoidable dead area. However, the efficiency gap between small-area cell and large-area modules for PSCs is much larger than the well-established PV technologies, as of today. Challenges in scaling up PSCs involve development of deposition methods for growth of uniform films over larger area and need reliable module design process (laser scribing process, interconnection properties, optimal width of subcells, etc.).

As of date, only lead-based perovskite systems show efficiency exceeding 20%, however, the toxicity of lead is a serious concern for their commercialization. Efforts have been made to replace Pb with nontoxic and earth-abundant alternatives (Shockley and Queisser 1961). Among all the metals, tin (Sn) and germanium (Ge) can form genuine perovskite structure since they both fulfill the coordination, ionic size, and charge balance prerequisites (Ke et al. 2019). Sn-based perovskites are potential candidate to replace Pb-atoms as they exhibit very similar optoelectronic characteristics, such as suitable optical band-gaps, high absorption coefficient, and reasonable charge carrier mobilities. However, Sn has two main oxidation states, +2 and the slightly more stable +4, which makes them even more unstable than Pb-based perovskite systems. Sn-based perovskite systems show higher *p*-doping and higher conductivity arising from the oxidation of Sn^{2+}/Sn^{4+}. The photovoltaic efficiency of Sn-based perovskites has reached 9%; however, the solar cells suffer significantly from low open-circuit voltage and low fill factor.

As the PCE of PSCs approaching their theoretical limits set by the Shockley–Queisser equation for single-junction solar cells, alternative architectural platforms are being explored in the form of the multifunction tandem solar cell. Composition engineering has been utilized to achieve the band-gap tunability of perovskite systems to develop perovskite (high-E_g)/perovskite (low-E_g) tandem solar cells (Zhao et al. 2017). High band-gap perovskite systems are also being explored to develop perovskite/crystalline-Silicon tandem solar cells (Sahli et al. 2018). Four-terminal and monolithic two-terminal tandem architectures have been successfully realized on both perovskite/perovskite and perovskite/crystalline-Silicon tandem solar cells. In the future, a lot more works are expected in this direction to boost the PCE over 30%.

References

Abdi-Jalebi M, Andaji-Garmaroudi Z, Cacovich S, Stavrakas C, Philippe B, Richter JM, Alsari M, Booker EP, Hutter EM, Pearson AP, Lilliu S, Savenije TJ, Rensmo H, Divitini G, Ducati C, Friend RH, Stranks SD (2018) Maximizing and stabilizing luminescence from halide perovskites with potassium passivation. Nature 555(7697):497–501

Aharon S, Dymshits A, Rotem A, Etgar L (2015) Temperature dependence of hole conductor free formamidinium lead iodide perovskite based solar cells. J Mater Chem A 3:9171–9178

Aitola K, Sveinbjoärnssona K, Correa-Baenab JP, Kaskelac A, Abated A, Tianc Y, Johanssona MJE, Graätzel M, Kauppinenc IE, Hagfeldtb A, Boschloo G (2016) Carbon nanotube-based hybrid hole-transporting material and selective contact for high efficiency perovskite solar cells. Energy Environ Sci 9:461–466

Alidoust N, Toroker MC, Keith JA, Carter EA (2014) Significant reduction in NiO band gap upon formation of $Li_xNi_{1-x}O$ alloys: applications to solar energy conversion. Chem Sus Chem 7:195–201

Anaya M, Correa-Baena JP, Lozano G, Saliba M, Anguita P, Roose B, Abate A, Steiner U, Grätzel M, Calvo ME, Hagfeldt A, Miguez H (2016) Optical analysis of $CH_3NH_3Sn_xPb_{1-x}I_3$ absorbers: a roadmap for perovskite-on-perovskite tandem solar cells. J Mater Chem A 4:11214–11221

Andreani LC, Bozzola A, Kowalczewski P, Liscidini M, Redorici L (2018) Silicon solar cells: toward the efficiency limits. Adv Phys-X 4(1):1548305

Aristidou N, Sanchez-Molina I, Chotchuangchutchaval T, Brown M, Martinez L, Rath T, Haque SA (2015) The Role of oxygen in the degradation of methylammonium lead trihalide perovskite photoactive layers. Angew Chem Int Ed 54(28):8208–8212

Arora N, Dar MI, Hinderhofer A, Pellet N, Schreiber F, Zakeeruddin SM, Grätzel M (2017) Perovskite solar cells with CuSCN hole extraction layers yield stabilized efficiencies greater than 20. Science 358:768–771

Asghar MI, Zhang J, Wang H, Lund PD (2017) Device stability of perovskite solar cells—a review. Renew Sustain Energy Rev 77:131–146

Azpiroz JM, Mosconi E, Bisquert J, De Angelis F (2015) Defect migration in methylammonium lead iodide and its role in perovskite solar cell operation. Energy Environ Sci 8(7):2118–2127

Bach U, Lupo D, Comte P, Moser J, Weissortel F, Salbeck J, Spreitzer H, Gratzel M (1998) Solid-state dye-sensitized mesoporous TiO_2 solar cells with high photon-to-electron conversion efficiencies. Nature 395:583

Bai Y, Yu H, Zhu ZL, Jiang K, Zhang T, Zhao N, Yang SH, Yan H (2015) High performance inverted structure perovskite solar cells based on a PCBM:polystyrene blend electron transport layer. J Mater Chem A 3:9098–9102

Bai Y, Dong Q, Shao Y, Deng Y, Wang Q, Shen L, Wang D, Wei W, Huang J (2016) Enhancing stability and efficiency of perovskite solar cells with crosslinkable silane-functionalized and doped fullerene. Nat Commun 7:12806

Baikie T, Fang Y, Kadro JM, Schreyer M, Wei F, Mhaisalkar SG, Graetzel M, White TJ (2013) Synthesis and crystal chemistry of the hybrid perovskite $(CH_3NH_3)PbI_3$ for solid-state sensitized solar cell applications. J Mater Chem A 1(18):5628–5641

Ball JM, Lee MM, Hey A, Snaith HJ (2013) Low-temperature processed meso-superstructured to thin-film perovskite solar cells. Energy Environ Sci 6:1739–1743

Bao Q, Li CM, Liao L, Yang H, Wang W, Ke C, Song Q, Bao H, Yu T, Loh KP, Guo J (2009) Electrical transport and photovoltaic effects of core–shell CuO/C60 nanowire heterostructure. Nanotechnology 20:065203

Beckmann PA (2010) A review of polytypism in lead iodide. Cryst Res Tech 45(5):455–460

Behrouznejad F, Tsai CM, Narra S, Diau EW, Taghavinia N (2017) Interfacial investigation on printable carbon-based mesoscopic perovskite solar cells with NiO_x/C back electrode. ACS Appl Mater Interfaces 9:25204–25215

Bera A, Wu K, Sheikh A, Alarousu E, Mohammed OF, Wu T (2015) Perovskite oxide $SrTiO_3$ as an efficient electron transporter for hybrid perovskite solar cells. J Phys Chem C 118:28494–28501

Bi D, Moon S-J, Haäggman L, Boschloo G, Yang L, Johansson EMJ, Nazeeruddin MK, Graätzel M, Hagfeldt A (2013) Using a two-step deposition technique to prepare perovskite ($CH_3NH_3PbI_3$) for thin film solar cells based on ZrO_2 and TiO_2 mesostructures. RSC Adv 3:18762–18766

Bi D, Tress W, Dar MI, Gao P, Luo J, Renevier C, Schenk K, Abate A, Giordano F, Correa Baena J-P (2016) Efficient luminescent solar cells based on tailored mixed-cation perovskites. Sci Adv 2:e1501170

Binek A, Hanusch FC, Docampo P, Bein T (2015) Stabilization of the trigonal high-temperature phase of formamidinium lead iodide. J Phys Chem Lett 6:1249–1253

Bu IYY, Fu YS, Li JF, Guo TF (2017) Large-area electrospray-deposited nanocrystalline Cu_XO hole transport layer for perovskite solar cells. RSC Adv 7:46651–46656

Buin A, Comin R, Xu J, Ip AH, Sargent EH (2015) Halide-dependent electronic structure of organolead perovskite materials. Chem Mater 27(12):4405–4412

Burschka J, Pellet N, Moon S-J, Humphry-Baker R, Gao P, Nazeeruddin MK, Grätzel M (2013) Sequential deposition as a route to high-performance perovskite-sensitized solar cells. Nature 499(7458):316–319

Bush KA, Palmstrom AF, Yu ZJ, Boccard M, Cheacharoen R, Mailoa JP, McMeekin DP, Hoye RLZ, Bailie CD, Leijtens T (2017) 23.6%-efficient monolithic perovskite/silicon tandem solar cells with improved stability. Nat Energy 2:17009

Cai ML, Tiong VT, Hreid T, Bell J, Wang HX (2015) An efficient hole transport material composite based on poly (3-hexylthiophene) and bamboo-structured carbon nanotubes for high performance perovskite solar cells. J Mater Chem A 3:2784–2793

Cao J, Liu Y-M, Jing X, Yin J, Li J, Xu B, Tan Y-Z, Zheng N (2015a) Well-defined thiolated nanographene as hole-transporting material for efficient and stable perovskite solar cells. J Am Chem Soc 137:10914–10917

Cao K, Zuo Z, Cui J, Shen Y, Moehl T, Zakeeruddin SM, Grätzel M, Wang M (2015b) Efficient screen printed perovskite solar cells based on mesoscopic$TiO_2/Al_2O_3/NiO$/carbon architecture. Nano Energy 17:171–179

Cao K, Cui J, Zhang H, Li H, Song JK, Shen Y, Cheng YB, Wang MK (2015c) Efficient mesoscopic perovskite solar cells based on the $CH_3NH_3PbI_2Br$ light absorber. J Mater Chem A 3:9116–9122

Capasso A, Matteocci F, Najafi L, Prato M, Buha J, Cinà L, Pellegrini V, Carlo AD, Bonaccorso F (2016) Few-layer: MoS_2 flakes as active buffer layer for stable perovskite solar cells. Adv Energy Mater 6:1600920

Carnie MJ, Charbonneau C, Davies ML, Troughton J, Watson TM, Wojciechowski K, Snaith H, Worsley DA (2013) A one-step low temperature processing route for organolead halide perovskite solar cells. Chem Commun 49:7893–7895

Chan CY, Wang YY, Wu GW, Diau EWG (2016) Solvent-extraction crystal growth for highly efficient carbon-based mesoscopic perovskite solar cells free of hole conductors. J Mater Chem A 4:3872–3878

Chang X, Li W, Zhu L, Liu H, Geng H, Xiang S, Liu J, Chen H (2016a) Carbon-based CsPbBr 3 perovskite solar cells: all-ambient processes and high thermal stability. ACS Appl Mater Interfaces 8:33649–33655

Chang X, Li W, Chen H, Zhu L, Liu H, Geng H, Xiang S, Liu J, Zheng X, Yang Y, Yang S (2016b) Colloidal precursor-induced growth of ultra-even $CH_3NH_3PbI_3$ for high-performance paintable carbon-based perovskite solar cells. ACS Appl Mater Interfaces 8:30184–30192

Chatterjee S, Pal AJ (2016) Introducing Cu_2O thin films as a hole-transport layer in efficient planar perovskite solar cell structures. J Phys Chem C 120:1428–1437

Chavhan S, Miguel O, Grande HJ, Gonzalez-Pedro V, Sanchez RS, Barea EM, Mora-Sero I, Tena-Zaera R (2014) Organo-metal halide perovskite-based solar cells with CuSCN as the inorganic hole selective contact. J Mater Chem A 2:12754–12760

Chen SY, Walsh A, Gong XG, Wei SH (2013) Classification of lattice defects in the Kesterite Cu_2ZnSnS_4 and $Cu_2ZnSnSe_4$ Earth-abundant solar cell absorbers. Adv Mater 25:1522–1539

Chen H, Wei Z, Yan K, Yi Y, Wang J, Yang S (2014) Liquid phase deposition of TiO_2 nanolayer affords $CH_3NH_3PbI_3$/nanocarbon solar cells with high open-circuit voltage. Faraday Discuss 176:271–286

Chen W, Wu Y, Yue Y, Liu J, Zhang W, Yang X, Chen H, Bi E, Ashraful I, Graätzel M, Han L (2015a) Efficient and stable large-area perovskite solar cells with inorganic charge extraction layers. Science 350:944–948

Chen WY, Deng LL, Dai SM, Wang X, Tian CB, Zhan XX, Xie SY, Huang RB, Zheng LS (2015b) Low-cost solution-processed copper iodide as an alternative to PEDOT:PSS hole transport layer for efficient and stable inverted planar heterojunction perovskite solar cells. J Mater Chem A 3:19353–19359

Chen W, Wu YZ, Liu J, Qin CJ, Yang XD, Islam A, Cheng YB, Han LY (2015c) Hybrid interfacial layer leads to solid performance improvement of inverted perovskite solar cells. Energy Environ Sci 8:629–640

Chen HN, Wei ZH, Zheng XL, Yang SH (2015d) A scalable electrodeposition route to the low-cost, versatile and controllable fabrication of perovskite solar cells. Nano Energy 15:216–226

Chen C, Cheng Y, Dai Q, Song H (2015e) Radio frequency magnetron sputtering deposition of TiO_2 thin films and their perovskite solar cell applications. Sci Rep 5:17684

Chen B, Shi J, Zheng X, Zhou Y, Zhu K, Priya S (2015f) Ferroelectric solar cells based on inorganic–organic hybrid perovskites. J Mater Chem A 3(15):7699–7705

Chen ST, Roh K, Lee J, Chong WK, Lu Y, Mathews N, Sum TC, Nurmikko A (2016a) A photonic crystal laser from solution based organo-lead iodide perovskite thin films. ACS Nano 10(4):3959–3967

Chen CM, Lin ZK, Huang WJ, Yang SH (2016b) WO_3 nanoparticles or nanorods incorporating Cs_2CO_3/PCBM buffer bilayer as carriers transporting materials for perovskite solar cells. Nanoscale Res Lett 11:464

Chen JZ, Xiong YL, Rong YG, Mei AY, Sheng YS, Jiang P, Hu Y, Li X, Han HW (2016c) Solvent effect on the hole-conductor-free fully printable perovskite solar cells. Nano Energy 27:130–137

Chen J, Rong Y, Mei A, Xiong Y, Liu T, Sheng Y, Jiang P, Hong L, Guan Y, Zhu X, Hou X, Duan M, Zhao J, Li X, Han H (2016d) Hole-conductor-free fully printable mesoscopic solar cell with mixed-anion perovskite $CH_3NH_3PbI_{(3-x)}(BF_4)_x$. Adv. Energy Mater 6:1502009

Chen HN, Zheng XL, Li Q, Yang YL, Xiao S, Hu C, Bai Y, Zhang T, Wong KS, Yang SH (2016e) An amorphous precursor route to the conformable oriented crystallization of CH3NH3PbBr 3 in mesoporous scaffolds: toward efficient and thermally stable carbon-based perovskite solar cells. J Mater Chem A 4:12897–12912

Chen HN, Wei ZH, He HX, Zheng XL, Wong KS, Yang SH (2016f) Solvent engineering boosts the efficiency of paintable carbon-based perovskite solar cells to beyond 14%. Adv Energy Mater 6:1502087

Chen C-C, Chang SH, Chen L-C, Kao F-S, Cheng H-M, Yeh S-C, Chen C-T, Wu W-T, Tseng Z-L, Chuang CL (2016g) Improving the efficiency of inverted mixed-organic-cation perovskite absorber based photovoltaics by tailing the surface roughness of PEDOT: PSS thin film. Sol Energy 134:445–451

Chen LC, Tseng ZL, Huang JK (2016h) A study of inverted-type perovskite solar cells with various composition ratios of $(FAPbI3)_{(1-x)}(MAPbBr\ 3)_x$. Nanomaterials 6:183

Chen W, Liu FZ, Feng XY, Djurisic AB, Chan WK, He ZB (2017a) Cesium doped NiO_x as an efficient hole extraction layer for inverted planar perovskite solar cells. Adv Energy Mater 7:1700722

Chen W, Xu L, Feng X, Jie J, He Z (2017b) Metal acetylacetonate series in interface engineering for full low-temperature-processed, high-performance, and stable planar perovskite solar cells with conversion efficiency over 16% on 1 cm^2 scale. Adv Mater 29:1603923

Chen M, Zha RH, Yuan ZY, Jing QS, Huang ZY, Yang XK, Yang SM, Zhao XH, Xu DL, Zou GDL (2017c) Boron and phosphorus co-doped carbon counter electrode for efficient hole-conductor-free perovskite solar cell. Chem Eng J 313:791–800

Chen Z, Yang G, Zheng X, Lei H, Chen C, Ma J, Wang H, Fang G (2017d) Bulk heterojunction perovskite solar cells based on room temperature deposited hole-blocking layer: suppressed hysteresis and flexible photovoltaic application. J Power Sources 351:123–129

Chen J, Xu J, Xiao L, Zhang B, Dai S, Yao J (2017e) Mixed-Organic-Cation $(FA)_x(MA)_{1-x}PbI_3$ planar perovskite solar cells with 16.48% efficiency via a low-pressure vapor-assisted solution processl. ACS Appl Mater Interfaces 9:2449–2458

Chen B-X, Li W-G, Rao H-S, Xu Y-F, Kuang D-B, Su C-Y (2017f) Large-grained perovskite films via $FA_xMA_{1-x}Pb(I_xBr_{1-x})_3$ single crystal precursor for efficient solar cells. Nano Energy 34:264–270

Chen B-A, Lin J-T, Suen N-T, Tsao C-W, Chu T-C, Hsu Y-Y, Chan T-S, Chan Y-T, Yang J-S, Chiu C-W, Chen HM (2017g) In situ identification of photo-and moisture-dependent phase evolution of perovskite solar cells. ACS Energy Lett 2(2):342–348

Chen H, Ye F, Tang WT, He JJ, Yin MS, Wang YB, Xie FX, Bi EB, Yang XD, Gratzel M, Han LY (2017h) A solvent- and vacuum-free route to large-area perovskite films for efficient solar modules. Nature 550(7674):92

Chen R, Wang W, Bu TL, Ku ZL, Zhong J, Peng Y, Xiao S, You W, Huang F, Cheng Y, Fu Z (2019) Materials and structures for the electron transport layer of efficient and stable perovskite solar cells. Acta Phys-Chim Sin 35:401–407

Cheng Y, Yang Q-D, Xiao J, Xue Q, Li H-W, Guan Z, Yip H-L, Tsang S-W (2015) Decomposition of organometal halide perovskite films on zinc oxide nanoparticles. ACS Appl Mater Interfaces 7:19986–19993

Cheng N, Liu P, Qi F, Xiao YQ, Yu WJ, Yu ZH, Liu W, Guo SS, Zhao XZ (2016) Multi-walled carbon nanotubes act as charge transport channel to boost the efficiency of hole transport material free perovskite solar cells. J Power Sources 332:24–29

Choi H, Jeong J, Kim H-B, Kim S, Walker B, Kim G-H, Kim JY (2014) Cesium-doped methylammonium lead iodide perovskite light absorber for hybrid solar cells. Nano Energy 7:80–85

Choi J, Song S, Horantner MT, Snaith HJ, Park T (2016) Well-defined nanostructured, single-crystalline TiO_2 electron transport layer for efficient planar perovskite solar cells. ACS Nano 10:6029–6036

Christians JA, Fung RCM, Kamat PV (2014) An inorganic hole conductor for organo-lead halide perovskite solar cells. Improved hole conductivity with copper iodide. J Am Chem Soc 136:758–764

Ciro J, Ramirez D, Mejia Escobar MA, Montoya JF, Mesa S, Betancur R, Jaramillo F (2017) Self-functionalization behind a solution-processed NiO_x film used as hole transporting layer for efficient perovskite solar cells. ACS Appl Mater Interfaces 9:12348–12354

Coll M, Gomez A, Mas-Marza E, Almora O, Garcia-Belmonte G, Campoy-Quiles M, Bisquert J (2015) Polarization switching and light-enhanced piezoelectricity in lead halide perovskites. J Phys Chem Lett 6(8):1408–1413

Correa-Baena J-P, Abate A, Saliba M, Tress W, Jacobssonm TJ, Grätzelm M, Hagfeldtm A (2017) The rapid evolution of highly efficient perovskite solar cells. Energy Environ Sci 10:710–727

D'Innocenzo V, Grancini G, Alcocer MJP, Kandada ARS, Stranks SD, Lee MM, Lanzani G, Snaith HJ, Petrozza A (2014) Excitons versus free charges in organo-lead tri-halide perovskites. Nat Comm 5(1):3586

Dang Y, Liu Y, Sun Y, Yuan D, Liu X, Lu W, Liu G, Xia H, Tao X (2015) Bulk crystal growth of hybrid perovskite material $CH_3NH_3PbI_3$. CrystEngComm 17(3):665–670

Dasgupta U, Chatterjee S, Pal AJ (2017) Thin-film formation of 2D MoS_2 and its application as a hole-transport layer in planar perovskite solar cells. Sol Energy Mater Sol Cells 172:353–360

De Bastiani M, Dell'Erba G, Gandini M, D'Innocenzo V, Neutzner S, Kandada ARS, Grancini G, Binda M, Prato M, Ball JM, Caironi M, Petrozza A (2016) Ion migration and the role of preconditioning cycles in the stabilization of the J–V characteristics of inverted hybrid perovskite solar cells. Adv Energy Mater 6(2):1501453

Deng J, Mortazavi M, Medhekar NV, Liu JZ (2012) Band engineering of $Ni_{1-x}Mg_xO$ alloys for photocathodes of high efficiency dye-sensitized solar cells. J Appl Phys 112:123703

Deng Y, Dong Q, Bi C, Yuan Y, Huang J (2016) Air-stable, efficient mixed-cation perovskite solar cells with Cu electrode by scalable fabrication of active layer. Adv Energy Mater 6:1600372

deQuilettes DW, Vorpahl SM, Stranks SD, Nagaoka H, Eperon GE, Ziffer ME, Snaith HJ, Ginger DS (2015) Impact of microstructure on local carrier lifetime in perovskite solar cells. Science 348(6235):683–686

deQuilettes DW, Zhang W, Burlakov VM, Graham DJ, Leijtens T, Osherov A, Bulović V, Snaith HJ, Ginger DS, Stranks SD (2016) Photo-induced halide redistribution in organic–inorganic perovskite films. Nat Comm 7(1):11683

Di Giacomo F, Razza S, Matteocci F, D'Epifanio A, Licoccia S, Brown TM, Di Carlo A (2014) High efficiency $CH_3NH_3PbI_{(3-x)}Cl_x$ perovskite solar cells with poly(3-hexylthiophene) hole transport layer. J Power Sources 251:152–156

Do Sung S, Ojha DP, You JS, Lee J, Kim J, Lee WI (2015) 50 nm sized spherical TiO_2 nanocrystals for highly efficient mesoscopic perovskite solar cells. Nanoscale 7:8898–8906

Dong X, Hu H, Lin B, Ding J, Yuan N (2014) The effect of ALD-Zno layers on the formation of $CH_3NH_3PbI_3$ with different perovskite precursors and sintering temperatures. Chem Commun 50:14405–14408

Dong Q, Fang Y, Shao Y, Mulligan P, Qiu J, Cao L, Huang J (2015a) Electron-hole diffusion lengths >175 μm in solution-grown $CH_3NH_3PbI_3$ single crystals. Science 347:967–970

Dong Q, Shi Y, Wang K, Li Y, Wang S, Zhang H, Xing Y, Du Y, Bai X, Ma T (2015b) Insight into perovskite solar cells based on SnO_2 compact electron-selective layer. J Phys Chem C 119:10212–10217

Dong Q, Liu F, Wong MK, Djurišić AB, Ren Z, Shen Q, Ng A, Surya C, Chan WK (2016): Indium oxide-based perovskite solar cells. In: FH Teherani, DC Look, DJ Rogers (eds), Proceedings SPIE 9749, oxide-based materials and devices VII, vol 9749, p 97491S

Duong T, Mulmudi HK, Shen H, Wu Y, Barugkin C, Mayon YO, Nguyen HT, Macdonald D, Peng J, Lockrey M (2016) Structural engineering using rubidium iodide as a dopant under excess lead iodide conditions for high efficiency and stable perovskites. Nano Energy 30:330–340

Duong T, Wu Y, Shen H, Peng J, Fu X, Jacobs D, Wang E-C, Kho TC, Fong KC, Stocks M (2017) Rubidium multication perovskite with optimized bandgap for perovskite-silicon tandem with over 26% efficiency. Adv Energy Mater 7:1700228

Fang Y, Dong Q, Shao Y, Yuan Y, Huang J (2015) Highly narrowband perovskite single-crystal photodetectors enabled by surface-charge recombination. Nat Photonics 9:679–686

Frost JM, Butler KT, Brivio F, Hendon CH, van Schilfgaarde M, Walsh A (2014) Atomistic origins of high-performance in hybrid halide perovskite solar cells. Nano Lett 14(5):2584–2590

Gangishetty MK, Scott RWJ, Kelly TL (2016) Effect of relative humidity on crystal growth, device performance and hysteresis in planar heterojunction perovskite solar cells. Nanoscale 8(12):6300–6307

Gharibzadeh S, Nejand BA, Moshaii A, Mohammadian N, Alizadeh AH, Mohammadpour R, Ahmadi V, Alizadeh A (2016) Two-step physical deposition of a compact CuI hole-transport layer and the formation of an interfacial species in perovskite solar cells. Chemsuschem 9:1929–1937

Gheno A, Thu Pham TT, Di Bin C, Bouclé J, Ratier B, Vedraine S (2017) Printable WO_3 electron transporting layer for perovskite solar cells: influence on device performance and stability. Sol Energy Mater Sol Cells 161:347–354

Gholipour S, Correa-Baena JP, Domanski K, Matsui T, Steier L, Giordano F, Tajabadi F, Tress W, Saliba M, Abate A, Ali AM, Taghavinia N, Grätzel M, Hagfeldt A (2016) Highly efficient and stable perovskite solar cells based on a low-cost carbon cloth. Adv Energy Mater 6

Giesbrecht N, Schlipf J, Oesinghaus L, Binek A, Bein T, Müller-Buschbaum P, Docampo P (2016) Synthesis of perfectly oriented and micrometer-sized MAPbBr 3 perovskite crystals for thin-film photovoltaic applications. ACS Energy Lett 1(1):150–154

Grancini G, Roldan-Carmona C, Zimmermann I, Mosconi E, Lee X, Martineau D, Narbey S, Oswald F, De Angelis F, Gräetzel M, Nazeeruddin MK (2017) One-year stable perovskite solar cells by 2D/3D interface engineering. Nat Commun 8:15684

Grätzel M (2014) The light and shade of perovskite solar cells. Nat Mater 13(9):838–842

Green MA, Ho-Baillie A, Snaith HJ (2014) The emergence of perovskite solar cells. Nat Photonics 8(7):506–514

Habisreutinger SN, Leijtens T, Eperon GE, Stranks SD, Nicholas RJ, Snaith HJ (2014a) Carbon nanotube/polymer composites as a highly stable hole collection layer in perovskite solar cells. Nano Lett 14:5561–5568

Habisreutinger SN, Leijtens T, Eperon GE, Stranks SD, Nicholas RJ, Snaith HJ (2014b) Enhanced hole extraction in perovskite solar cells through carbon nanotubes. J Phys Chem Lett 5:4207–4212

Hadouchi W, Rousset J, Tondelier D, Geffroy B, Bonnassieux Y (2016) Zinc oxide as a hole blocking layer for perovskite solar cells deposited in atmospheric conditions. RSC Adv 6:67715–67723

Han GS, Chung HS, Kim DH, Kim BJ, Lee J-W, Park N-G, Cho IS, Lee J-K, Lee S, Jung HS (2015) Epitaxial 1D electron transport layers for high-performance perovskite solar cells. Nanoscale 7:15284–15290

Hao F, Stoumpos CC, Cao DH, Chang RPH, Kanatzidis MG (2014a) Lead-free solid-state organic–inorganic halide perovskite solar cells. Nat Photon 8:489–494

Hao F, Stoumpos CC, Chang RPH, Kanatzidis MG (2014b) Anomalous band gap behavior in mixed Sn and Pb perovskites enables broadening of absorption spectrum in solar cells. J Am Chem Soc 136:8094–8099

Hao F, Stoumpos CC, Liu Z, Chang RPH, Kanatzidis MG (2014c) Controllable perovskite crystallization at a gas-solid interface for hole conductor-free solar cells with steady power conversion efficiency over 10%. J Am Chem Soc 136(46):16411–16419

Hashmi SG, Martineau D, Dar MI, Myllymaki TTT, Sarikka T, Ulla V, Zakeeruddin SM, Grätzel M (2017) High performance carbon-based printed perovskite solar cells with humidity assisted thermal treatment. J Mater Chem A 5:12060–12067

Hawash Z, Ono LK, Raga SR, Lee MV, Qi Y (2015) Air exposure induced dopant redistribution and energy level shifts in spin-coated spiro-MeOTAD films. Chem Mater 27:562–569

Hawash Z, Ono LK, Qi Y (2018) Recent advances in spiro-MeOTAD hole transport material and its applications in organic-inorganic halide perovskite solar cells. Adv Mater Interfaces 5:1700623

He Q, Yao K, Wang X, Xia X, Leng S, Li F (2017) Room-temperature and solution-processable Cu-doped nickel oxide nanoparticles for efficient hole-transport layers of flexible large-area perovskite solar cells. ACS Appl Mater Interfaces 9:41887–41897

Heo JH, Lee MH, Han HJ, Patil BR, Yu JS, Im SH (2016) Highly efficient low temperature solution processable planar type $CH_3NH_3PbI_3$ perovskite flexible solar cells. J Mater Chem A 4:1572–1578

Hirst LC, Ekins-Daukes NJ (2011) Fundamental losses in solar cells. Prog Photovolt 19(3):286–293

Hodes G (2013) Perovskite-based solar cells. Science 342:317–318

Hoke ET, Slotcavage DJ, Dohner ER, Bowring AR, Karunadasa HI, McGehee MD (2015) Reversible photo-induced trap formation in mixed-halide hybrid perovskites for photovoltaics. Chem Sci 6(1):613–617

Hong S, Han A, Lee EC, Ko K, Park J, Song H, Han M-H, Han C (2015) A facile and low-cost fabrication of TiO_2 compact layer for efficient perovskite solar cells. Curr Appl Phys 15:574–579

Hou Y, Quiroz COR, Scheiner S, Chen W, Stubhan T, Hirsch A, Halik M, Brabec CJ (2015) Low-temperature and hysteresis-free electron-transporting layers for efficient, regular, and planar structure perovskite solar cells. Adv Energy Mater 5:1501056

Hou XM, Hu Y, Liu HW, Mei AY, Li X, Duan M, Zhang GA, Rong YG, Han HW (2017) Effect of guanidinium on mesoscopic perovskite solar cells. J Mater Chem A 5:73–78

https://www.iea.org/reports/world-energy-outlook-2019

Hu X, Zhang XD, Liang L, Bao J, Li S, Yang WL, Xie Y (2014a) High-performance flexible broadband photodetector based on organolead halide perovskite. Adv Funct Mater 24(46):7373–7380

Hu L, Peng J, Wang WW, Xia Z, Yuan JY, Lu JL, Huang XD, Ma WL, Song HB, Chen W, Cheng YB, Tang J (2014b) Sequential deposition of $CH_3NH_3PbI_3$ on planar NiO film for efficient planar perovskite solar cells. ACS Photonics 1:547–553

Hu L, Wang W, Liu H, Peng J, Cao H, Shao G, Xia Z, Ma W, Tang J (2015) PbS colloidal quantum dots as an effective hole transporter for planar heterojunction perovskite solar cells. J Mater Chem A 3:515–518

Hu C, Bai Y, Xiao S, Zhang T, Meng XY, Ng WK, Yang Y, Wong KS, Chen H, Yang S (2017a) Tuning the A-site cation composition of FA perovskites for efficient and stable NiO-based *p-i-n* perovskite solar cells. J Mater Chem A 5:21858–21865

Hu W, Liu T, Yin X, Liu H, Zhao X, Luo S, Guo Y, Yao Z, Wang J, Wang N, Lin H, Guo Z (2017b) Hematite electron-transporting layers for environmentally stable planar perovskite solar cells with enhanced energy conversion and lower hysteresis. J Mater Chem A 5:1434–1441

Hua Y, Zhang J, Xu B, Liu P, Cheng M, Kloo L, Johansson EMJ, Sveinbjornsson K, Aitola K, Boschloo G, Sun L (2016) Facile synthesis of fluorene-based hole transport materials for highly efficient perovskite solar cells and solid-state dye-sensitized solar cells. Nano Energy 26:108–113

Huang Z, Zeng X, Wang H, Zhang W, Li Y, Wang M, Cheng Y-B, Chen W (2014) Enhanced performance of p-type dye sensitized solar cells based on mesoporous $Ni_{1-x}Mg_xO$ ternary oxide films. RSC Adv 4:60670–60674

Huang L, Hu Z, Xu J, Zhang K, Zhang J, Zhang J, Zhu Y (2016a) Efficient and stable planar perovskite solar cells with a non hygroscopic small molecule oxidant doped hole transport layer. Electrochim Acta 196:328–336

Huang Y, Zhu J, Ding Y, Chen S, Zhang C, Dai S (2016b) TiO_2 sub-microsphere film as scaffold layer for efficient perovskite solar cells. ACS Appl Mater Interfaces 8:8162–8167

Huang J, Xu P, Liu J, You X-Z (2017) Sequential introduction of cations deriving large-grain $Cs_xFA_{1-x}PbI_3$ thin film for planar hybrid solar cells, insight into phase-segregation and thermal-healing behavior. Small 13:1603225

Huangfu M, Shen Y, Zhu G, Xu K, Cao M, Gu F, Wang L (2015) Copper iodide as inorganic hole conductor for perovskite solar cells with different thickness of mesoporous layer and hole transport layer. Appl Surf Sci 357:2234–2240

Hwang SH, Roh J, Lee J, Ryu J, Yun J, Jang J (2014) Size-controlled SiO_2 nanoparticles as scaffold layers in thin-film perovskite solar cells. J Mater ChemA 2:16429–16433

Im J-H, Lee C-R, Lee J-W, Park S-W, Park N-G (2013) 6.5% efficient perovskite quantum-dot-sensitized solar cell. Nanoscale 3(10):4088–4093

Im J, Stoumpos CC, Jin H, Freeman AJ, Kanatzidis MG (2015) Antagonism between spin-orbit coupling and steric effects causes anomalous band gap evolution in the perovskite photovoltaic materials CH3NH3$Sn_{1-x}Pb_xI$3. J Phys Chem Lett 6:3503–3509

International Energy Agency (2019) World Energy Outlook 2017. Technical report, 2017

Ip AH, Thon SM, Hoogland S, Voznyy O, Zhitomirsky D, Debnath R, Levina L, Rollny LR, Carey GH, Fischer A, Kemp KW, Kramer IJ, Ning Z, Labelle AJ, Chou KW, Amassian A, Sargent EH (2012) Hybrid passivated colloidal quantum dot solids. Nat Nanotech 7:577–582

Isikgor FH, Li B, Zhu H, Xu Q, Ouyang J (2016) High performance planar perovskite solar cells with a perovskite of mixed organic cations and mixed halides, $MA_{1-x}FA_xPbI_{3-y}Cl_y$. J Mater Chem A 4:12543–12553

Ito S, Tanaka S, Vahlman H, Nishino H, Manabe K, Lund P (2014a) Carbon-double-bond-free printed solar cells from TiO_2/$CH_3NH_3PbI_3$/CuSCN/Au: structural control and photoaging effects. ChemPhysChem 15:1194–1200

Ito S, Tanaka S, Manabe K, Nishino H (2014b) Effects of surface blocking layer of Sb_2S_3 on nanocrystalline TiO_2 for $CH_3NH_3PbI_3$ perovskite solar cells. J Phys Chem C 118:16995–17000

Ito S, Tanaka S, Nishino H (2015) Lead-halide perovskite solar cells by CH_3NH_3I dripping on PbI_2-CH_3NH_3I-DMSO precursor layer for planar and porous structures using CuSCN hole-transporting material. J Phys Chem Lett 6:881–886

Jacobsson TJ, Correa-Baena J-P, Pazoki M, Saliba M, Schenk K, Gratzel M, Hagfeldt A (2016) Exploration of the compositional space for mixed lead halogen perovskites for high efficiency solar cells. Energy Environ Sci 9:1706–1724

Jena AK, Kulkarni A, Miyasaka T (2019) Halide perovskite photovoltaics: background, status, and future prospects. Chem Rev 119(5):3036–3103

Jeng JY, Chiang YF, Lee MH, Peng SR, Guo TF, Chen P, Wen TC (2013) CH3NH3PbI3 perovskite/fullerene planar-heterojunction hybrid solar cells. Adv Mater 25:3727–3732

Jeng JY, Chen KC, Chiang TY, Lin PY, Tsai TD, Chang YC, Guo TF, Chen P, Wen TC, Hsu YJ (2014) Nickel oxide electrode interlayer in $CH_3NH_3PbI_3$ perovskite/PCBM planar-heterojunction hybrid solar cells. Adv Mater 26:4107–4113

Jeon NJ, Noh JH, Kim YC, Yang WS, Ryu S, Seok SI (2014) Solvent engineering for high-performance inorganic–organic hybrid perovskite solar cells. Nat Mater 13(9):897–903

Jeon I, Chiba T, Delacou C, Guo Y, Kaskela A, Reynaud O, Kauppinen EI, Maruyama S, Matsuo Y (2015a) Single-walled carbon nanotube film as electrode in indium-free planar heterojunction perovskite solar cells: investigation of electron-blocking layers and dopants. Nano Lett 15:6665–6671

Jeon NJ, Noh JH, Yang WS, Kim YC, Ryu S, Seo J, Seok SI (2015b) Compositional engineering of perovskite materials for high-performance solar cells. Nature 517(7535):476

Jeon I, Seo S, Sato Y, Delacou C, Anisimov A, Suenaga K, Kauppinen EI, Maruyama S, Matsuo Y (2017) Perovskite solar cells using carbon nanotubes both as cathode and as anode. J Phys Chem C 121:25743–25749

Jiang H, Kloc C (2013) Single-crystal growth of organic semiconductors. MRS Bull 38(1):28–33

Jiang Q, Zhang L, Wang H, Yang X, Meng J, Liu H, Yin Z, Wu J, Zhang X, You J (2016) Erratum: corrigendum: enhanced electron extraction using SnO_2 for high-efficiency planar-structure $HC(NH_2)2PbI_3$-based perovskite solar cells. Nat Energy 2:16177

Jiang X, Yu Z, Zhang Y, Lai J, Li J, Gurzadyan GG, Yang X, Sun L (2017) High-performance regular perovskite solar cells employing low-cost poly(ethylenedioxythiophene) as a hole-transporting material. Sci Rep 7:42564

Johnston MB, Herz LM (2016) Hybrid perovskites for photovoltaics: charge-carrier recombination, diffusion, and radiative efficiencies. Acc Chem Res 49(1):146–154

Jung JW, Chueh CC, Jen AKY (2015a) High-performance semi transparent perovskite solar cells with 10% power conversion efficiency and 25% average visible transmittance based on transparent CuSCN as the hole-transporting material. Adv Energy Mater 5:1500486

Jung JW, Chueh CC, Jen AK (2015b) A low-temperature, solution-processable, Cu-doped nickel oxide hole-transporting layer via the combustion method for high-performance thin-film perovskite solar cells. Adv Mater 27:7874–7880

Ke W, Fang G, Wang J, Qin P, Tao H, Lei H, Liu Q, Dai X, Zhao X (2014) Perovskite solar cell with an efficient TiO_2 compact film. ACS Appl Mater Interfaces 6:15959–15965

Ke W, Fang G, Liu Q, Xiong L, Qin P, Tao H, Wang J, Lei H, Li B, Wan J, Yang G, Yan Y (2015a) Low-temperature solution-processed tin oxide as an alternative electron transporting layer for efficient perovskite solar cells. J Am Chem Soc 137:6730–6733

Ke W, Zhao D, Cimaroli AJ, Grice CR, Qin P, Liu Q, Xiong L, Yan Y, Fang G (2015b) Effects of annealing temperature of tin oxide electron selective layers on the performance of perovskite solar cells. J Mater Chem A 3:24163–24168

Ke W, Zhao D, Grice CR, Cimaroli AJ, Ge J, Tao H, Lei H, Fang G, Yan Y (2015c) Efficient planar perovskite solar cells using room-temperature vacuum-processed C_{60} electron selective layers. J Mater Chem A 3:17971–17976

Ke W, Zhao D, Xiao C, Wang C, Cimaroli AJ, Grice CR, Yang M, Li Z, Jiang C-S, Al-Jassim M, Zhu K, Kanatzidis MG, Fang G, Yan Y (2016) Cooperative tin oxide fullerene electron selective layers for high-performance planar perovskite solar cells. J Mater Chem A 4:14276–14283

Ke WJ, Stoumpos CC, Kanatzidis MG (2019) "Unleaded" perovskites: Status Quo and future prospects of tin-based perovskite solar cells. Adv Mater 31(47):1803230

Kegelmann L, Wolff CM, Awino C, Lang F, Unger EL, Korte L, Dittrich T, Neher D, Rech B, Albrecht S (2017) It takes two to Tango—double-layer selective contacts in perovskite solar cells for improved device performance and reduced hysteresis. ACS Appl Mater Interfaces 9:17245–17255

Kim H-S, Lee C-R, Im J-H, Lee K-B, Moehl T, Marchioro A, Moon S-J, Humphry-Baker R, Yum J-H, Moser JE, Grätzel M, Park N-G (2012) Lead iodide perovskite sensitized all-solid-state submicron thin film mesoscopic solar cell with efficiency exceeding 9%. Sci Rep 2(1):591

Kim H-B, Choi H, Jeong J, Kim S, Walker B, Song S, Kim JY (2014a) Mixed solvents for the optimization of morphology in solution-processed, inverted-type perovskite/fullerene hybrid solar cells. Nanoscale 6(12):6679–6683

Kim JH, Liang PW, Williams ST, Cho N, Chueh CC, Glaz MS, Ginger DS, Jen AKY (2014b) High-performance and environmentally stable planar heterojunction perovskite solar cells based on a solution-processed copper-doped nickel oxide hole-transporting layer. Adv Mater 27:695–701

Kim J, Kim G, Kim TK, Kwon S, Back H, Lee J, Lee SH, Kang H, Lee K (2014c) Efficient planar-heterojunction perovskite solar cells achieved via interfacial modification of a sol–gel ZnO electron collection layer. J Mater Chem A 2:17291–17296

Kim JH, Liang PW, Williams ST, Cho N, Chueh CC, Glaz MS, Ginger DS, Jen AK (2015) High-performance and environmentally stable planar heterojunction perovskite solar cells based on a solution-processed copper-doped nickel oxide hole-transporting layer. Adv Mater 27:695–701

Kim J, Kim HP, Teridi MAM, Yusoff ARbM, Jang J (2016) Bandgap tuning of mixed organic cation utilizing chemical vapor deposition process. Sci Rep 6:37378

Kim H-S, Seo J-Y, Xie H, Lira-Cantu M, Zakeeruddin SM, Grätzel M, Hagfeldt A (2017) Effect of Cs-incorporated NiO_x on the performance of perovskite solar cells. ACS Omega 2:9074–9079

Kogo A, Numata Y, Ikegami M, Miyasaka T (2015) Nb_2O_5 blocking layer for high open-circuit voltage perovskite solar cells. Chem Lett 44:829–830

Kohnehpoushi S, Nazari P, Nejand BA, Eskandari M (2018) MoS_2: a two-dimensional hole-transporting material for high-efficiency, low-cost perovskite solar cells. Nanotechnology 29:205201

Kojima A, Teshima K, Shirai Y, Miyasaka T (2009) Organometal halide perovskites as visible-light sensitizers for photovoltaic cells. J Am Chem Soc 131(17):6050–6051

Kolny-Olesaik J, Weller H (2013) Synthesis and application of colloidal $CuInS_2$ semiconductor nanocrystals. ACS Appl Mater Interfaces 5:12221–12237

Ku Z, Rong Y, Xu M, Liu T, Han H (2013) Full printable processed mesoscopic $CH_3NH_3PbI_3/TiO_2$ heterojunction solar cells with carbon counter electrode. Sci Rep 3:3132

Kumar MH, Yantara N, Dharani S, Gräetzel M, Mhaisalkar S, Boix PP, Mathews N (2013) Flexible, low-temperature, solution processed ZnO-based perovskite solid state solar cells. Chem Commun 49:11089–11091

Kwon YS, Lim J, Yun H-J, Kim Y-H, Park T (2014) A diketopyrrolopyrrole-containing hole transporting conjugated polymer for use in efficient stable organic–inorganic hybrid solar cells based on a perovskite. Energy Environ Sci 7(4):1454–1460

Kwon U, Kim BG, Nguyen DC, Park JH, Ha NY, Kim SJ, Ko SH, Lee S, Lee D, Park HJ (2016) Solution-processible crystalline NiO nanoparticles for high-performance planar perovskite photovoltaic cells. Sci Rep 6:30759

Lang F, Gluba MA, Albrecht S, Rappich J, Korte L, Rech B, Nickel NH (2015) Perovskite solar cells with large-area CVD-graphene for tandem solar cells. J Phys Chem Lett 6:2745–2750

Lee MM, Teuscher J, Miyasaka T, Murakami TN, Snaith HJ (2012) Efficient hybrid solar cells based on meso-superstructured organometal halide perovskites. Science 338:643–647

Lee JW, Lee TY, Yoo PJ, Grätzel M, Mhaisalkar S, Park NG (2014) Rutile TiO_2-based perovskite solar cells. J Mater Chem A 2:9251–9259

Lee JW, Kim DH, Kim HS, Seo SW, Cho SM, Park NG (2015a) Formamidinium and cesium hybridization for photo- and moisture-stable perovskite solar cell. Adv Energy Mater 5(20):1501310

Lee J, Menamparambath MM, Hwang JY, Baik S (2015b) Hierarchically structured hole transport layers of spiro-OMeTAD and multiwalled carbon nanotubes for perovskite solar cells. Chem Sus Chem 8:2358–2362

Lee JW, Kim DH, Kim HS, Seo SW, Cho SM, Park NG (2015c) Formamidinium and cesium hybridization for photo- and moisture-stable perovskite solar cell. Adv Energy Mater 5:1501310

Lee K, Yoon C, Noh J, Jang J (2016) Morphology-controlled mesoporous SiO_2 nanorods for efficient scaffolds in organo-metal halide perovskite solar cells. Chem Commun 52:4231–4234

Leijtens T, Eperon GE, Pathak S, Abate A, Lee MM, Snaith HJ (2013) Overcoming ultraviolet light instability of sensitized TiO_2 with meso-superstructured organometal tri-halide perovskite solar cells. Nat Commun 4:2885

Li Z (2015) Stable perovskite solar cells based on WO_3 nanocrystals as hole transport layer. Chem Lett 44:1140–1141

Li WZ, Dong HP, Guo XD, Li N, Li JW, Niu GD, Wang LD (2014a) Graphene oxide as dual functional interface modifier for improving wettability and retarding recombination in hybrid perovskite solar cells. J Mater Chem A 2:20105–20111

Li Z, Kulkarni SA, Boix PP, Shi E, Cao A, Fu K, Batabyal SK, Zhang J, Xiong Q, Wong LH, Mathews N, Mhaisalkar SG (2014b) Laminated carbon nanotube networks for metal electrode-free efficient perovskite solar cells. ACS Nano 8:6797–6804

Li Y, Zhu J, Huang Y, Wei J, Liu F, Shao Z, Hu L, Chen S, Yang S, Tang J, Yao J, Dai S (2015a) Efficient inorganic solid solar cells composed of perovskite and PbS quantum dots. Nanoscale 7:9902–9907

Li Y, Zhu J, Huang Y, Liu F, Lv M, Chen SH, Hu LH, Tang JW, Yao JX, Dai SY (2015b) Mesoporous SnO_2 nanoparticle films as electron-transporting material in perovskite solar cells. RSC Adv 5:28424–28429

Li M, Wang Z-K, Yang Y-G, Hu Y, Feng S-L, Wang J-M, Gao X-Y, Liao L-S (2016a) Copper salts doped spiro-OMeTAD for high-performance perovskite solar cells. Adv Energy Mater 6:1601156

Li H, Cao K, Cui J, Liu S, Qiao X, Shen Y, Wang M (2016b) 14.7% efficient mesoscopic perovskite solar cells using single walled carbon nanotubes/carbon composite counter electrodes. Nanoscale 8:6379–6385

Li Z, Yang M, Park J-S, Wei S-H, Berry JJ, Zhu K (2016c) Stabilizing perovskite structures by tuning tolerance factor: formation of formamidinium and cesium lead iodide solid-state alloys. Chem Mater 28:284–292

Li G, Zhang T, Guo N, Xu F, Qian X, Zhao Y (2016d) Ion-exchange-induced 2D–3D conversion of $HMA_{1-x}FA_xPbI_3Cl$ perovskite into a high-quality $MA_{1-x}FA_xPbI_3$ perovskite. Angew Chem, Int Ed 55:13460–13464

Li Z, Tinkham J, Schulz P, Yang M, Kim DH, Berry J, Sellinger A, Zhu K (2017a) Acid additives enhancing the conductivity of spiro-OMeTAD toward high-efficiency and hys-teresis-less planar perovskite solar cells. Adv Energy Mater 7:1601451

Li J, Yao JX, Liao XY, Yu RL, Xia HR, Sun WT, Peng LM (2017b) A contact study in hole conductor free perovskite solar cells with low temperature processed carbon electrodes. RSC Adv 7:20732–20737

Liang L, Huang Z, Cai L, Chen W, Wang B, Chen K, Bai H, Tian Q, Fan B (2014) Magnetron sputtered zinc oxide nanorods as thickness-insensitive cathode interlayer for perovskite planar-heterojunction solar cells. ACS Appl Mater Interfaces 6:20585–20589

Liang PW, Chueh CC, Williams ST, Jen AKY (2015) Roles of fullerene-based interlayers in enhancing the performance of organometal perovskite thin-film solar cells. Adv Energy Mater 5:1402321

Liao W-Q, Zhang Y, Hu C-L, Mao J-G, Ye H-Y, Li P-F, Huang SD, Xiong R-G (2015) A lead-halide perovskite molecular ferroelectric semiconductor. Nat Commun 6(1):7338

Liao W, Zhao D, Yu Y, Shrestha N, Ghimire K, Grice CR, Wang C, Xiao Y, Cimaroli AJ, Ellingson RJ, Podraza NJ, Zhu K, Xiong R-G, Yan Y (2016) Fabrication of efficient low-bandgap perovskite solar cells by combining formamidinium tin iodide with methylammonium lead iodide. J Am Chem Soc 138:12360–12363

Ling X, Yuan J, Liu D, Wang Y, Zhang Y, Chen S, Wu H, Jin F, Wu F, Shi G, Tang X, Zheng J, Liu S (Frank), Liu Z, Ma W (2015) Room-temperature processed Nb_2O_5 as the electron-transporting layer for efficient planar perovskite solar cells. ACS Appl Mater Interfaces 9:23181–23188

Liu D, Kelly TL (2014) Perovskite solar cells with a planar heterojunction structure prepared using room-temperature solution processing techniques. Nat Photonics 8:133–138

Liu M, Johnston MB, Snaith HJ (2013) Efficient planar heterojunction perovskite solar cells by vapour deposition. Nature 501(7467):395–398

Liu Y, Yang Z, Cui D, Ren X, Sun J, Liu X, Zhang J, Wei Q, Fan H, Yu F, Zhang X, Zhao C, Liu S (2015a) Two-inch-sized perovskite CH3NH3PbX3 (X = Cl, Br, I) crystals: growth and characterization. Adv Mater 27(35):5176–5183

Liu ZH, Zhang M, Xu XB, Cai FS, Yuan HL, Bu LL, Li WH, Zhu AL, Zhao ZX, Wang MK, Cheng YB, He HS (2015b) NiO nanosheets as efficient top hole transporters for carbon counter electrode based perovskite solar cells. J Mater Chem A 3:24121–24127

Liu Z, Zhang M, Xu X, Bu L, Zhang W, Li W, Zhao Z, Wang M, Cheng YB, He H (2015c) p-Type mesoscopic NiO as an active interfacial layer for carbon counter electrode based perovskite solar cells. Dalton Trans 44:3967–3973

Liu T, Liu L, Hu M, Yang Y, Zhang L, Mei A, Han H (2015d) Critical parameters inTiO_2/ZrO_2/Carbon-based mesoscopic perovskite solar cell. J Power Sources 293:533–538

Liu T, Kim D, Han H, Yusoff AR, Jang J (2015e) Fine-tuning optical and electronic properties of graphene oxide for highly efficient perovskite solar cells. Nanoscale 7:10708–10718

Liu J, Gao C, Luo L, Ye Q, He X, Ouyang L, Guo X, Zhuang D, Liao C, Mei J, Lau W (2015f) Low-temperature, solution processed metal sulfide as an electron transport layer for efficient planar perovskite solar cells. J Mater Chem A 3:11750–11755

Liu J, Shirai Y, Yang X, Yue Y, Chen W, Wu Y, Islam A, Han L (2015g) High-quality mixed-organic-cation perovskites from a phase-pure non-stoichiometric intermediate $(FAI)_{1-x}$-PbI_2 for solar cells. Adv Mater 27:4918–4923

Liu JW, Pathak SK, Sakai N, Sheng R, Bai S, Wang ZP, Snaith HJ (2016a) Identification and mitigation of a critical interfacial instability in perovskite solar cells employing copper thiocyanate hole-transporter. Adv Mater Interfaces 3:1600571

Liu ZY, Sun B, Shi TL, Tang ZR, Liao GL (2016b) Enhanced photovoltaic performance and stability of carbon counter electrode based perovskite solar cells encapsulated by PDMS. J Mater Chem A 4:10700–10709

Liu Z, Shi T, Tang Z, Sun B, Liao G (2016c) Using a low-temperature carbon electrode for preparing hole-conductor-free perovskite heterojunction solar cells under high relative humidity. Nanoscale 8:7017–7023

Liu T, Yu L, Liu H, Hou Q, Wang C, He H, Li J, Wang N, Wang J, Guo Z (2017a) Ni nanobelts induced enhancement of hole transport and collection for high efficiency and ambient stable mesoscopic perovskite solar cells. J Mater Chem A 5:4292–4299

Liu S, Cao K, Li H, Song J, Han J, Shen Y, Wang M (2017b) Full printable perovskite solar cells based on mesoscopic TiO_2/Al_2O_3/NiO (carbon nanotubes) architecture. Sol Energy 144:158–165

Liu T, Zong Y, Zhou Y, Yang M, Li Z, Game OS, Zhu K, Zhu R, Gong Q, Padture NP (2017c) High-performance formamidinium-based perovskite solar cells via microstructure- mediated δ-to-α phase transformation. Chem Mater 29:3246–3250

Lu H, Ma Y, Gu B, Tian W, Li L (2015) Identifying the optimum thickness of electron transport layers for highly efficient perovskite planar solar cells. J Mater Chem A 3:16445–16452

Luo Q, Zhang Y, Liu CY, Li JB, Wang N, Lin H (2015) Iodide-reduced graphene oxide with dopant-free spiro-OMeTAD for ambient stable and high-efficiency perovskite solar cells. J Mater Chem A 3:15996–16004

Luo Q, Ma H, Zhang Y, Yin XW, Yao ZB, Wang N, Li JB, Fan SS, Jiang KL, Lin H (2016) Cross-stacked super aligned carbon nanotube electrodes for efficient hole conductor-free perovskite solar cells. J Mater Chem A 4:5569–5577

Luo H, Lin X, Hou X, Pan L, Huang S, Chen X (2017a) Efficient and air-stable planar perovskite solar cells formed on graphene-oxide-modified PEDOT:PSS hole transport layer. Nano- Micro Lett 9:39

Luo Q, Chen H, Lin Y, Du H, Hou Q, Hao F, Wang N, Guo Z, Huang J (2017b) Discrete Iron(III) oxide nanoislands for efficient and photostable perovskite solar cells. Adv Funct Mater 1702090:1–9

Lv M, Zhu J, Huang Y, Li Y, Shao Z, Xu Y, Dai S (2015) Colloidal $CuInS_2$ quantum dots as inorganic hole-transporting material in perovskite solar cells. ACS Appl Mater Interfaces 7:17482–17488

Ma J, Zheng X, Lei H, Ke W, Chen C, Chen Z, Yang G, Fang G (2017) Highly efficient and stable planar perovskite solar cells with large-scale manufacture of E-beam evaporated SnO_2 toward commercialization. Sol RRL 1:1700118

Madhavan VE, Zimmermann I, Roldan-Carmona C, Grancini G, Buffiere M, Belaidi A, Nazeeruddin MK (2016) Copper thiocyanate inorganic hole-transporting material for high-efficiency perovskite solar cells. ACS Energy Lett 1:1112–1117

Mahmood K, Swain BS, Amassian A (2014) Double-layered ZnO nanostructures for efficient perovskite solar cells. Nanoscale 6:14674–14678

Mahmood K, Swain BS, Kirmani AR, Amassian A (2015a) Highly efficient perovskite solar cells based on a nanostructured WO_3–TiO_2 core–shell electron transporting material. J Mater Chem A 3:9051–9057

Mahmood K, Swain BS, Amassian A (2015b) 16.1% Efficient hysteresis-free mesostructured perovskite solar cells based on synergistically improved ZnO nanorod arrays. Adv Energy Mater 5:1500568

Mahmud MA, Elumalai NK, Upama MB, Wang D, Wright M, Chan KH, Xu C, Haque F, Uddin A (2016) Single versus mixed organic cation for low temperature processed perovskite solar cells. Electrochim Acta 222:1510–1521

Mali SS, Shim CS, Park HK, Heo J, Patil PS, Hong CK (2015a) Ultrathin atomic layer deposited TiO_2 for surface passivation of hydrothermally grown 1D TiO_2 nanorod arrays for efficient solid-state perovskite solar cells. Chem Mater 27:1541–1551

Mali SS, Su Shim C, Kook Hong C (2015b) Highly porous Zinc Stannate (Zn_2SnO_4) nanofibers scaffold photoelectrodes for efficient methyl ammonium halide perovskite solar cells. Sci Rep 5:11424

Mamun AA, Ava TT, Zhang K, Baumgart H, Namkoong G (2017) New PCBM/carbon based electron transport layer for perovskite solar cells. Phys Chem Chem Phys 19:17960–17966

Matsui T, Seo J-Y, Saliba M, Zakeeruddin SM, Grätzel M (2017) Room-temperature formation of highly crystalline multication perovskites for efficient, low-cost solar cells. Adv Mater 29:1606258

McMeekin DP, Sadoughi G, Rehman W, Eperon GE, Saliba M, Hörantner MT, Haghighirad A, Sakai N, Korte L, Rech B (2016) A mixed-cation lead mixed-halide perovskite absorber for tandem solar cells. Science 351:151–155

Meng L, You J, Guo T-F, Yang Y (2016) Recent advances in the inverted planar structure of perovskite solar cells. Acc Chem Res 49(1):155–165

Mielczarek K, AA (2014) Perovskite based hybrid solar cells with transparent carbon nanotube electrodes, MRS Proc, 1667, Mrss14-1667-b09-82

Morton O (2006) Solar energy: a new day dawning? Silicon Valley sunrise. Nature 443(7107):19–22

Motti SG, Gandini M, Barker AJ, Ball JM, Srimath Kandada AR, Petrozza A (2016) Photoinduced emissive trap states in lead halide perovskite semiconductors. ACS Energy Lett 1(4):726–730

Murugadoss G, Kanda H, Tanaka S, Nishino H, Ito S, Imahoric H, Umeyama T (2016) An efficient electron transport material of tin oxide for planar structure perovskite solar cells. J Power Sources 307:891–897

Najafi L, Taheri B, Martin-Garcia B, Bellani S, Di Girolamo D, Agresti A, Oropesa-Nunez R, Pescetelli S, Vesce L, Calabro E, Prato M, Del Rio Castillo AE, Di Carlo A, Bonaccorso F (2018) MoS_2 quantum dot/graphene hybrids for advanced interface engineering of a $CH_3NH_3PbI_3$ perovskite solar cell with an efficiency of over 20. ACS Nano 12(11):10736–10754

Nazari FAP, Abdollahi Nejand B, Ahmadi V, Payandeh M, Salavati-Niasar M (2017) Physico-chemical interface engineering of CuI/Cu as advanced potential hole-transporting materials/metal contact couples in hysteresis-free ultralow-cost and large-area perovskite solar cells. J Phys Chem C 121:21935–21944

Nejand BA, Ahmadi V, Gharibzadeh S, Shahverdi HR (2016) Cuprous oxide as a potential low-cost hole-transport material for stable perovskite solar cells. Chemsuschem 9:302–313

Nie W, Tsai H, Blancon JC, Liu F, Stoumpos CC, Traore B, Kepenekian M, Durand O, Katan C, Tretiak S, Crochet J, Ajayan PM, Kanatzidis M, Even J, Mohite AD (2018) Critical role of interface and crystallinity on the performance and photostability of perovskite solar cell on nickel oxide. Adv Mater 30:1703879

Niu G, Yu H, Li J, Wang D, Wang L (2016) Controlled orientation of perovskite films through mixed cations toward high performance perovskite solar cells. Nano Energy 27:87–94

Niu G, Li W, Li J, Liang X, Wang L (2017) Enhancement of Thermal Stability for Perovskite Solar Cells through Cesium Doping. RSC Adv 7:17473–17479

Noel NK, Abate A, Stranks SD, Parrott ES, Burlakov VM, Goriely A, Snaith HJ (2014) Enhanced photoluminescence and solar cell performance via Lewis base passivation of organic-inorganic lead halide perovskites. ACS Nano 8(10):9815–9821

Nouri E, Mohammadi MR, Lianos P (2017) Inverted perovskite solar cells basedon lithium-functionalized graphene oxide as an electron-transporting layer. Chem Commun 53:1630–1633

NREL solar energy chart: https://www.nrel.gov/pv/assets/pdfs/pv-efficiency-chart.20190103.pdf

O'Regan B, Schwartz DT, Zakeeruddin SM, Grätzel M (2000) Electrodeposited nanocomposite n–p heterojunctions for solid-state dye-sensitized photovoltaics. Adv Mater 12:1263–1267

Ogomi Y, Morita A, Tsukamoto S, Saitho T, Fujikawa N, Shen Q, Toyoda T, Yoshino K, Pandey SS, Ma T, Hayase S (2014) $CH_3NH_3Sn_xPb_{(1-x)}I_3$ Perovskite Solar Cells Covering up to 1060 nm. J Phys Chem Lett 5:1004–1011

Oh LS, Kim DH, Lee JA, Shin SS, Lee J, Park IJ, Ko MJ, Park N, Pyo SG, Hong KS, Kim JY (2015) Zn_2SnO_4-based photoelectrodes for organolead halide perovskite solar cells. J Phys Chem C 118:22991–22994

Ono LK, Qi Y (2016) Surface and interface aspects of organometal halide perovskite materials and solar cells. J Phys Chem Lett 7(22):4764–4794

Ono LK, Raga SR, Remeika M, Winchester AJ, Gabe A, Qi Y (2015) Pinhole-free hole transport layers significantly improve the stability of MAPbI3-based perovskite solar cells under operating conditions. J Mater Chem A 3(30):15451–15456

Ou QD, Li C, Wang QK, Li YQ, Tang JX (2017) Recent advances in energetics of metal halide perovskite interfaces. Adv Mater Interfaces 4:1600694

Pae SR, Byun S, Kim J, Kim M, Gereige I, Shin B (2018) Improving uniformity and reproducibility of hybrid perovskite solar cells via a low-temperature vacuum deposition process for NiO_x hole transport layers. ACS Appl Mater Interfaces 10:534–540

Pan ZX, Mora-Sero I, Shen Q, Zhang H, Li Y, Zhao K, Wang J, Zhong XH, Bisquert J (2014) High-efficiency "green" quantum dot solar cells. J Am Chem Soc 136:9203–9210

Park NG (2015) Perovskite solar cells: an emerging photovoltaic technology. Mater Today 18:65–72

Park BW, Seok SI (2019) Intrinsic instability of inorganic-organic hybrid halide perovskite materials. Adv Mater 31(20):1805337

Park IJ, Park MA, Kim DH, Park GD, Kim BJ, Son HJ, Ko MJ, Lee DK, Park T, Shin H, Park N-G, Jung HS, Young J (2015a) New hybrid hole extraction layer of perovskite solar cells with a planar *p–i–n* geometry. J Phys Chem 119:27285–27290

Park JH, Seo J, Park S, Shin SS, Kim YC, Jeon NJ, Shin HW, Ahn TK, Noh JH, Yoon SC, Hwang CS, Seok SI (2015b) Efficient $CH_3NH_3PbI_3$ perovskite solar cells employing nanostructured p-type NiO electrode formed by a pulsed laser deposition. Adv Mater 27:4013–4019

Park IJ, Park MA, Kim DH, Park GD, Kim BJ, Son HJ, Ko MJ, Lee D-K, Park T, Shin H, Park N-G, Jung HS, Kim JY (2015c) New hybrid hole extraction layer of perovskite solar cells with a planar *p-i-n* geometry. J Phys Chem C 119:27285–27290

Park IJ, Kang G, Park MA, Kim JS, Seo SW, Kim DH, Zhu K, Park T, Kim JY (2017a) Highly efficient and uniform 1 cm^2 perovskite solar cells with an electrochemically deposited NiO_x hole-extraction layer. Chemsuschem 10:2660–2667

Park YH, Jeong I, Bae S, Son HJ, Lee P, Lee J, Lee C-H, Ko MJ (2017b) Inorganic rubidium cation as an enhancer for photovoltaic performance and moisture stability of $HC(NH_2)_2PbI_3$ perovskite solar cells. Adv Funct Mater 27:1605988

Pathak SK, Abate A, Ruckdeschel P, Roose B, Gödel KC, Vaynzof Y, Santhala A, Watanabe SI, Hollman DJ, Noel N, Sepe A, Wiesner U, Friend R, Snaith HJ, Steiner U (2014) Performance and stability enhancement of dye-sensitized and perovskite solar cells by Al doping of TiO_2. Adv Funct Mater 24:6046–6055

Pattanasattayavong P, Gross NY, Zhao K, Ndjawa GON, Li J, Yan F, O'Regan BC, Amassian A, Anthopoulo TD (2013a) Hole-transporting transistors and circuits based on the transparent inorganic semiconductor copper(I) thiocyanate (CuSCN) processed from solution at room temperature. Adv Mater 25:1504–1509

Pattanasattayavong P, Ndjawa GON, Zhao K, Chou KW, Gross NY, O'Regan BC, Amassian A, Anthopoulos TD (2013b) Electric field-induced hole transport in copper(i) thiocyanate (CuSCN) thin-films processed from solution at room temperature. Chem Commun 49:4154–4156

Paulo S, Stoicaa G, Cambaraua W, Martinez-Ferrerob E, Palomares E (2016) Carbon quantum dots as new hole transport material for perovskite solar cells. Synth Met 222:17–22

Pellet N, Gao P, Gregori G, Yang T-Y, Nazeeruddin MK, Maier J, Grätzel M (2014) Mixed-organic-cation perovskite photovoltaics for enhanced solar-light harvesting. Angew Chem Int Ed 53:3151–3157

Petrus ML, Schlipf J, Li C, Gujar TP, Giesbrecht N, Muller-Buschbaum P, Thelakkat M, Bein T, Huttner S, Docampo P (2017) Capturing the sun: a review of the challenges and perspectives of perovskite solar cells. Adv. Energy Mater 7(16):1700264

Qin P, Tanaka S, Ito S, Tetreault N, Manabe K, Nishino H, Nazeeruddin MK, Grätzel M (2014a) Inorganic hole conductor-based lead halide perovskite solar cells with 12.4% conversion efficiency. Nat Commun 5:3834

Qin P, Domanski AL, Chandiran AK, Berger R, Butt HJ, Darm MI, Moehl T, Tetreault N, Gao P, Ahmad S, Nazeeruddin MK, Grätzel M (2014b) Yttrium-substituted nanocrystalline TiO_2 photoanodes for perovskite based heterojunction solar cells. Nanoscale 6:1508–1514

Qin PL, Lei HW, Zheng XL, Liu Q, Tao H, Yang G, Ke WJ, Xiong LB, Qin MC, Zhao XZ, Fang GJ (2016) Copper-doped chromium oxide hole-transporting layer for perovskite solar cells: interface engineering and performance improvement. Adv Mater Interfaces 3:1500799

Qiu L, Deng J, Lu X, Yang Z, Peng H (2014) Integrating perovskite solar cells into a flexible fiber. Angew Chem Int Ed Engl 53:10425–10428

Quan LN, Yuan M, Comin R, Voznyy O, Beauregard EM, Hoogland S, Buin A, Kirmani AR, Zhao K, Amassian A, Kim DH, Sargent EH (2016) Ligand-stabilized reduced-dimensionality perovskites. J Am Chem Soc 138:2649–2655

Rao H-S, Chen B-X, Li W-G, Xu Y-F, Chen H-Y, Kuang D-B, Su C-Y (2015) Improving the extraction of photogenerated electrons with SnO_2 nanocolloids for efficient planar perovskite solar cells. Adv Funct Mater 25:7200–7207

Rao H, Sun W, Ye S, Yan W, Li Y, Peng H, Liu Z, Bian Z, Huang C (2016a) Solution-Processed CuS NPs as an inorganic hole-selective contact material for inverted planar perovskite solar cells. ACS Appl Mater Interfaces 8:7800–7805

Rao H, Ye S, Sun W, Yan W, Li Y, Peng HT, Liu Z, Bian Z, Li Y, Huang C (2016b) A 19.0% efficiency achieved in CuO_x-based inverted $CH_3NH_3PbI_{3-x}Cl_x$ solar cells by an effective Cl doping method. Nanoenergy 27:51–57

Rehman W, McMeekin DP, Patel JB, Milot RL, Johnston MB, Snaith HJ, Herz LM (2017) Photovoltaic mixed-cation lead mixed-halide perovskites: links between crystallinity, photo-stability and electronic properties. Energy Environ Sci 10(1):361–369

Reyna Y, Salado M, Kazim S, Pérez-Tomas A, Ahmad S, Lira-Cantu M (2016) Performance and stability of mixed $FAPbI_{3(0.85)}MAPbBr_{3(0.15)}$ halide perovskite solar cells under outdoor conditions and the effect of low light irradiation. Nano Energy 30:570–579

Richardson G, O'Kane SEJ, Niemann RG, Peltola TA, Foster JM, Cameron PJ, Walker AB (2016) Can slow-moving ions explain hysteresis in the current–voltage curves of perovskite solar cells? Energy Environ Sci 9(4):1476–1485

Rong Y, Ku Z, Mei A, Liu T, Xu M, Ko S, Li X, Han H (2014) Hole-conductor-free mesoscopic $TiO_2/CH_3NH_3PbI_3$ heterojunction solar cells based on anatase nanosheets and carbon counter electrodes. J Phys Chem Lett 5:2160–2164

Rong Y, Hou X, Hu Y, Mei A, Liu L, Wang P, Han H (2017) Synergy of ammonium chloride and moisture on perovskite crystallization for efficient printable mesoscopic solar cells. Nat Commun 8:14555

Ryu S, Seo J, Shin SS, Kim YC, Jeon NJ, Noh JH, Il Seok S (2015) Fabrication of metal-oxide-free $CH_3NH_3PbI_3$ perovskite solar cells processed at low temperature. J Mater Chem A 3:3271–3275

Ryu J, Lee K, Yun J, Yu H, Lee J, Jang J (2017) Paintable carbon-based perovskite solar cells with engineered perovskite/carbon interface using carbon nanotubes dripping method. Small 13:1701225

Sahli F, Werner J, Kamino BA, Brauninger M, Monnard R, Paviet-Salomon B, Barraud L, Ding L, Leon JJD, Sacchetto D, Cattaneo G, Despeisse M, Boccard M, Nicolay S, Jeangros Q, Niesen B, Ballif C (2018) Fully textured monolithic perovskite/silicon tandem solar cells with 25.2% power conversion efficiency. Nat Mater 17(9):820

Saidaminov MI, Abdelhady AL, Murali B, Alarousu E, Burlakov VM, Peng W, Dursun I, Wang L, He Y, Maculan G, Goriely A, Wu T, Mohammed OF, Bakr OM (2015) High-quality bulk hybrid perovskite single crystals within minutes by inverse temperature crystallization. Nat Commun 6(1):7586

Saidaminov MI, Kim J, Jain A, Quintero-Bermudez R, Tan H, Long G, Tan F, Johnston A, Zhao Y, Voznyy O, Sargent EH (2018) Suppression of atomic vacancies via incorporation of isovalent small ions to increase the stability of halide perovskite solar cells in ambient air. Nat Energy 3(8):648–654

Saliba M, Matsui T, Seo J-Y, Domanski K, Correa-Baena J-P, Nazeeruddin MK, Zakeeruddin SM, Tress W, Abate A, Hagfeldt A (2016a) Cesium-containing triple cation perovskite solar cells: improved stability, reproducibility and high efficiency. Energy Environ Sci 9:1989–1997

Saliba M, Matsui T, Domanski K, Seo J-Y, Ummadisingu A, Zakeeruddin SM, Correa-Baena J-P, Tress WR, Abate A, Hagfeldt A, Grätzel M (2016b) Incorporation of rubidium cations into perovskite solar cells improves photovoltaic performance. Science 354:206–209

Saliba M, Matsui T, Domanski K, Seo J-Y, Ummadisingu A, Zakeeruddin SM, Correa-Baena J-P, Tress WR, Abate A, Hagfeldt A, Grätzel M (2016c) Incorporation of rubidium cations into perovskite solar cells improves photovoltaic performance. Science 354(6309):206–209

Sanehira EM, Marshall AR, Christians JA, Harvey SP, Ciesielski PN, Wheeler LM, Schulz P, Lin LY, Beard MC, Luther JM (2017) Enhanced mobility $CsPbI_3$ quantum dot arrays for record-efficiency, high-voltage photovoltaic cells. Sci Adv 3:eaao4204

Santra PK, Nair PV, Thomas KG, Kamat PV (2013) $CuInS_2$-sensitized quantum dot solar cell. Electrophoretic deposition, excited-state dynamics, and photovoltaic performance. J Phys Chem Lett 4:722–729

Sarkar A, Jeon NJ, Noh JH, Seok SI (2014) Well-organized mesoporous TiO_2 photoelectrodes by block copolymer-induced Sol-Gel assembly for inorganic-organic hybrid perovskite solar cells. J Phys Chem C 118:16688–16693

Sepalage GA, Meyer S, Pascoe A, Scully AD, Huang F, Bach U, Cheng Y-B, Spiccia L (2015) Copper (I) iodide as hole-conductor in planar perovskite solar cells: probing the origin of J-V hysteresis. Adv Funct Mater 25:5650–5661

Shao S, Liu F, Xie Z, Wang L (2010) High-efficiency hybrid polymer solar cells with inorganic P- and N-type semiconductor nanocrystals to collect photogenerated charges. J Phys Chem C 114:9161

Sherkar TS, Jan Anton Koster L (2016) Can ferroelectric polarization explain the high performance of hybrid halide perovskite solar cells? Phys Chem Chem Phys 18(1):331–338

Shi D, Adinolfi V, Comin R, Yuan M, Alarousu E, Buin A, Chen Y, Hoogland S, Rothenberger A, Katsiev K, Losovyj Y, Zhang X, Dowben PA, Mohammed OF, Sargent EH, Bakr OM (2015) Low trap-state density and long carrier diffusion in organolead trihalide perovskite single crystals. Science 347(6221):519–522

Shockley W, Queisser HJ (1961) Detailed balance limit of efficiency of p-n junction solar cells. J Appl Phys 32(3):510–519

Smecca E, Numata Y, Deretzis I, Pellegrino G, Boninelli S, Miyasaka T, La Magna A, Alberti A (2016) Stability of solution-processed $MAPbI_3$ and $FAPbI_3$ layers. Phys Chem Chem Phys 18(19):13413–13422

Snaith HJ (2013) Perovskites: the emergence of a new era for low-cost, high-efficiency solar cells. J Phys Chem Lett 4:3623–3630

Snaith HJ, Abate A, Ball JM, Eperon GE, Leijtens T, Noel NK, Stranks SD, Wang JT-W, Wojciechowski K, Zhang W (2014) Anomalous hysteresis in perovskite solar cells. J Phys Chem Lett 5(9):1511–1515

Son DY, Im JH, Kim HS, Park NG (2014) 11% efficient perovskite solar cell based on ZnO nanorods: an effective charge collection system. J Phys Chem C 118:16567–16573

Song J, Zheng E, Bian J, Wang XF, Tian W, Sanehira Y, Miyasaka T (2015a) Low-temperature SnO_2-based electron selective contact for efficient and stable perovskite solar cells. J Mater Chem A 3:10837–10844

Song J, Bian J, Zheng E, Wang X-F, Tian W, Miyasaka T (2015b) Efficient and environmentally stable perovskite solar cells based on ZnO electron collection layer. Chem Lett 44:610–612

Stranks SD, Eperon GE, Grancini G, Menelaou C, Alcocer MJP, Leijtens T, Herz LM, Petrozza A, Snaith HJ (2013) Electron-hole diffusion lengths exceeding 1 micrometer in an organometal trihalide perovskite absorber. Science 342(6156):341–344

Stylianakis MM, Maksudov T, Panagiotopoulos A, Kakavelakis G, Petridis K (2019) Inorganic and hybrid perovskite based laser devices: a review. Materials 12(6):859

Su T-S, Hsieh T-Y, Hong C-Y, Wei T-C (2015) Electrodeposited ultrathin TiO_2 blocking layers for efficient perovskite solar cells. Sci Rep 5:16098

Subbiah AS, Halder A, Ghosh S, Mahuli N, Hodes G, Sarkar SK (2014) Inorganic hole conducting layers for perovskite-based solar cells. J Phys Chem Lett 5:1748–1753

Sum TC, Mathews N (2014a) Advancements in perovskite solar cells: photophysics behind the photovoltaics. Energy Environ Sci 7(8):2518–2534

Sum TC, Mathews N (2014b) Advancements in perovskite solar cells: photophysics behind the photovoltaics. Energy Environ Sci 7:2518–2534

Sun W, Li Y, Ye S, Rao H, Yan W, Peng HT, Li Y, Liu Z, Wang S, Chen Z, Xiao L, Bian Z, Huang C (2016a) High-performance inverted planar heterojunction perovskite solar cells based on a solution-processed $CuOx$ hole transport layer. Nanoscale 8:10806–10813

Sun W, Ye S, Rao H, Li Y, Liu Z, Xiao L, Chen Z, Bian Z, Huang C (2016b) Room-temperature and solution-processed copper iodide as the hole transport layer for inverted planar perovskite solar cells. Nanoscale 8:15954–15960

Sveinbjornsson K, Aitola K, Zhang J, Johansson MB, Zhang X, Correa-Baena J-P, Hagfeldt A, Boschloo G, Johansson EMJ (2016) Ambient air-processed mixed-ion perovskites for high-efficiency solar cell. J Mater Chem A 4:16536–16545

Tainter GD, Hörantner MT, Pazos-Outón LM, Lamboll RD, Āboliņš H, Leijtens T, Mahesh S, Friend RH, Snaith HJ, Joyce HJ, Deschler F (2019) Long-range charge extraction in back-contact perovskite architectures via suppressed recombination. Joule 3(5):1301–1313

Tan ZK, Moghaddam RS, Lai ML, Docampo P, Higler R, Deschler F, Price M, Sadhanala A, Pazos LM, Credgington D, Hanusch F, Bein T, Snaith HJ, Friend RH (2014) Bright light-emitting diodes based on organometal halide perovskite. Nat Nanotechnol 9(9):687–692

Tang J, Kemp KW, Hoogland S, Jeong KS, Liu H, Levina L, Furukawa M, Wang X, Debnath R, Cha D, Chou KW, Fischer A, Amassian A, Asbury JB, Sargent EH (2011) Colloidal-quantum-dot photovoltaics using atomic-ligand passivation. Nat Mater 10:765

Tang J-F, Tseng Z-L, Chen L-C, Chu S-Y (2016) ZnO nanowalls grown at low-temperature for electron collection in high-efficiency perovskite solar cells. Sol Energy Mater Sol Cells 154:18–22

Tao C, Neutzner S, Colella L, Marras S, Srimath Kandada AR, Gandini M, De Bastiani M, Pace G, Manna L, Caironi M, Bertarelli C, Petrozza A (2015) 17.6% stabilized efficiency in low-temperature processed planar perovskite solar cells. Energy Environ Sci 8:2365–2370

Tavakoli MM, Tavakoli R, Hasanzadeh S, Mirfasih MH (2016) Interface engineering of perovskite solar cell using a reduced-graphene scaffold. J Phys Chem C 120:19531–19536

Tian H, Xu B, Chen H, Johansson EM, Boschloo G (2014) Solid-state perovskite-sensitized p-type mesoporous nickel oxide solar cells. Chemsuschem 7:2150–2153

Tsai HH, Nie WY, Blancon JC, Toumpos CCS, Asadpour R, Harutyunyan B, Neukirch AJ, Verduzco R, Crochet JJ, Tretiak S, Pedesseau L, Even J, Alam MA, Gupta G, Lou J, Ajayan PM, Bedzyk MJ, Kanatzidis MG, Mohite AD (2016a) High-efficiency two-dimensional Ruddlesden-Popper perovskite solar cells. Nature 536(7616):312–316

Tsai CM, Wu HP, Chang ST, Huang CF, Wang CH, Narra S, Yang YW, Wang CL, Hung CH, Diau EWG (2016b) Role of tin chloride in tin-rich mixed-halide perovskites applied as mesoscopic solar cells with a carbon counter electrode. ACS Energy Lett 1:1086–1093

Tsai CM, Wu GW, Narra S, Chang HM, Mohanta N, Wu HP, Wang CL, Diau EWG (2017) Control of preferred orientation with slow crystallization for carbon-based mesoscopic perovskite solar cells attaining efficiency 15%. J Mater Chem A 5:739–747

Tsujimoto K, Nguyen DC, Ito S, Nishino H, Matsuyoshi H, Konno A, Asoka Kumara GR, Tennakone K (2012) TiO_2 surface treatment effects by Mg^{2+}, Ba^{2+}, and Al^{3+} on Sb_2S_3 extremely thin absorber solar cells. J Phys Chem C 116:13465–13471 (2012)

Upama MB, Elumalai NK, Mahmud MA, Wang D, Haque F, Gonçales VR, Gooding JJ, Wright M, Xu C, Uddin A (2017) Role of fullerene electron transport layer on the morphology and optoelectronic properties of perovskite solar cells. Org Electron 50:279–289

Vanalakar SA, Agawane GL, Shin SW, Suryawanshi MP, Gurav KV, Jeon KS, Patil PS, Jeong CW, Kim JY, Kim JH (2015) A review on pulsed laser deposited CZTS thin films for solar cell applications. J Alloys Compd 619:109–121

Walsh A, Chen SY, Wei SH, Gong XG (2012) Kesterite thin-film solar cells: advances in materials modelling of Cu2ZnSnS4. Adv Energy Mater 2:400–409

Wang H, Kim DH (2017) Perovskite-based photodetectors: materials and devices. Chem Soc Rev 46(17):5204–5236

Wang KC, Jeng JY, Shen PS, Chang YC, Diau EW, Tsai CH, Chao TY, Hsu HC, Lin PY, Chen P, Guo TF, Wen TC (2014a) p-type mesoscopic nickel oxide/organometallic perovskite heterojunction solar cells. Sci Rep 4:4756

Wang KC, Shen PS, Li MH, Chen S, Lin MW, Chen P, Guo TF (2014b) Low-temperature sputtered nickel oxide compact thin film as effective electron blocking layer for mesoscopic $NiO/CH_3NH_3PbI_3$ perovskite heterojunction solar cells. ACS Appl Mater Interfaces 6:11851–11858

Wang H, Zeng X, Huang Z, Zhang W, Qiao X, Hu B, Zou X, Wang M, Cheng YB, Chen W (2014c) Boosting the photocurrent density of p-type solar cells based on organometal halide perovskite-sensitized mesoporous NiO photocathodes. ACS Appl Mater Interfaces 6:12609–12617

Wang L, Fu W, Gu Z, Fan C, Yang X, Li H, Chen H (2014d) Low temperature solution processed planar heterojunction perovskite solar cells with a CdSe nanocrystal as an electron transport/extraction layer. J Mater Chem C 2:9087–9090

Wang JTW, Ball JM, Barea EM, Abate A, Alexander-Webber JA, Huang J, Saliba M, Mora-Sero I, Bisquert J, Snaith HJ, Nicholas RJ (2014e) Low-temperature processed electron collection layers of graphene/TiO_2 nanocomposites in thin film perovskite solar cells. Nano Lett 14:724–730

Wang K, Shi Y, Dong Q, Li Y, Wang S, Yu X, Wu M, Ma T (2015a) Low-temperature and solution-processed amorphous WO_X as electron-selective layer for perovskite solar cells. J Phys Chem Lett 6:755–759

Wang H, Hu XY, Chen HX (2015b) The effect of carbon black in carbon counter electrode for $CH_3NH_3PbI_3/TiO_2$ heterojunction solar cells. RSC Adv 5:30192–30196

Wang XY, Li Z, Xu WJ, Kulkarni SA, Batabyal SK, Zhang S, Cao AY, Wong LH (2015c) TiO_2 nanotube arrays based flexible perovskite solar cells with transparent carbon nanotube electrode. Nano Energy 11:728–735

Wang J, Qin M, Tao H, Ke W, Chen Z, Wan J, Qin P, Xiong L, Lei H, Yu H, Fang G (2015d) Performance enhancement of perovskite solar cells with Mg-doped TiO_2 compact film as the hole-blocking layer. Appl Phys Lett 106:121104

Wang H, Sayeed BA, Wang T (2015e) Perovskite solar cells based on nanocrystalline SnO_2 material with extremely small particle sizes. Aust J Chem 68:1783–1788

Wang BB, Zhang ZG, Ye SY, Gao L, Yan TH, Bian ZQ, Huang CH, Li YF (2016a) Solution-processable cathode buffer layer for high-performance ITO/CuSCN-based planar heterojunction perovskite solar cell. Electrochim Acta 218:263–270

Wang BX, Liu TF, Zhou YB, Chen X, Yuan XB, Yang YY, WP Liu, Wang JM, Han HW, Tang YW (2016b) Hole-conductor-free perovskite solar cells with carbon counter electrodes based on ZnO nanorod arrays. Phys Chem Chem Phys 18:27078–27082

Wang F, Endo M, Mouri S, Miyauchi Y, Ohno Y, Wakamiya A, Murata Y, Matsuda K (2016c) Highly stable perovskite solar cells with an all-carbon hole transport layer. Nanoscale 8:11882–11888

Wang K, Shi Y, Li B, Zhao L, Wang W, Wang X, Bai X, Wang S, Hao C, Ma T (2016d) Amorphous Inorganic Electron-selective layers for efficient perovskite solar cells: feasible strategy towards room-temperature fabrication. Adv Mater 28:1891–1897

Wang C, Zhao D, Grice CR, Liao W, Yu Y, Cimaroli A, Shrestha N, Roland PJ, Chen J, Yu Z, Liu P, Cheng N, Ellingson R, Zhao X, Yan Y (2016e) Low-temperature plasma-enhanced atomic layer deposition of tin oxide electron selective layers for highly efficient planar perovskite solar cells. J Mater Chem A 4:12080–12087

Wang F, Ma J, Xie F, Li L, Chen J, Fan J, Zhao N (2016f) Organic cation-dependent degradation mechanism of organotin halide perovskites. Adv Funct Mater 26:3417–3423

Wang S, Jiang Y, Juarez-Perez EJ, Ono LK, Qi Y (2016g) Accelerated degradation of methylammonium lead iodide perovskites induced by exposure to iodine vapour. Nat Energy 2(1):16195

Wang HX, Yu Z, Jiang X, Li JJ, Cai B, Yang XC, Sun LC (2017a) Efficient and stable inverted planar perovskite solar cells employing CuI as hole-transporting layer prepared by solid–gas transformation. Energy Technol 5:1836–1843

Wang X, Deng L-L, Wang L-Y, Dai S-M, Xing Z, Zhan X-X, Lu X-Z, Xie S-Y, Huang R-B, Zheng L-S (2017b) Cerium oxide standing out as an electron transport layer for efficient and stable perovskite solar cells processed at low temperature. J Mater Chem A 5:1706–1712

Wang Z, McMeekin DP, Sakai N, van Reenen S, Wojciechowski K, Patel JB, Johnston MB, Snaith HJ (2017c) Efficient and air-stable mixed-cation lead mixed-halide perovskite solar cells with n-doped organic electron extraction layers. Adv Mater 29:1604186

Wang R, Mujahid M, Duan Y, Wang ZK, Xue JJ, Yang Y (2019) A review of perovskites solar cell stability. Adv Funct Mater 29(47):1808843

Wei Z, Chen H, Yan K, Yang S (2014) Inkjet printing and instant chemical transformation of a $CH_3NH_3PbI_3$/nanocarbon electrode and interface for planar perovskite solar cells. Angew Chem Int Ed Engl 53:13239–13243

Wei HY, Xiao JY, Yang YY, Lv ST, Shi JJ, Xu X, Dong J, Luo YH, Li DM, Meng QB (2015a) Free-standing flexible carbon electrode for highly efficient hole-conductor-free perovskite solar cells. Carbon 93:861–868

Wei ZH, Chen HN, Yan KY, Zheng XL, Yang SH (2015b) Hysteresis-free multi-walled carbon nanotube-based perovskite solar cells with a high fill factor. J Mater Chem A 3:24226–24231

Wei W, Hu BY, Jin FM, Jing ZZ, Li YX, Blanco AAG, Stacchiola DJ, Hu YH (2017) Potassium-chemical synthesis of 3D graphene from CO_2 and its excellent performance in HTM-free perovskite solar cells. J Mater Chem A 5:7749–7752

Wei-Chih L, Kun-Wei L, Tzung-Fang G, Jung L (2015) Perovskite-based solar cells with nickel-oxidized nickel oxide hole transfer layer. IEEE Trans Electron Devices 62:1590–1595

Wijeyasinghe N, Regoutz A, Eisner F, Du T, Tsetseris L, Lin YH, Faber H, Pattanasattayavong P, Li JH, Yan F, McLachlan MA, Payne DJ, Heeney M, Anthopoulos TD (2017) Copper (I) thiocyanate (CuSCN) hole-transport layers processed from aqueous precursor solutions and their application in thin-film transistors and highly efficient organic and organometal halide perovskite solar cells. Adv Funct Mater 27:1701818

Wojciechowski K, Leijtens T, Siprova S, Schlueter C, Hoärantner MT, Wang JTW, Li CZ, Jen AKY, Lee TL, Snaith HJ (2015) C_{60} as an efficient n-type compact layer in perovskite solar cells. J Phys Chem Lett 6:2399–2405

Wu Z, Bai S, Xiang J, Yuan Z, Yang Y, Cui W, Gao X, Liu Z, Jin Y, Sun B (2014a) Efficient planar heterojunction perovskite solar cells employing graphene oxide as hole conductor. Nanoscale 6:10505–10510

Wu Y, Yang X, Chen H, Zhang K, Qin C, Liu J, Peng W, Islam A, Bi E, Ye F, Yin M, Zhang P, Han L (2014b) Highly compact TiO_2 layer for efficient hole-blocking in perovskite solar cells. Appl Phys Express 7:52301

Wu Q, Xue C, Li Y, Zhou P, Liu W, Zhu J, Dai S, Zhu C, Yang S (2015a) Kesterite Cu_2ZnSnS_4 as a low-cost inorganic hole-transporting material for high-efficiency perovskite solar cells. ACS Appl Mater Interfaces 7:28466–28473

Wu WQ, Huang F, Chen D, Cheng YB, Caruso RA (2015b) Thin films of dendritic anatase titania nanowires enable effective hole-blocking and efficient light-harvesting for high-performance mesoscopic perovskite solar cells. Adv Funct Mater 25:3264–3272

Wu R, Yang B, Xiong J, Cao C, Huang Y, Wu F, Sun J, Zhou C, Huang H, Yang J (2015c) Dependence of device performance on the thickness of compact TiO_2 layer in perovskite/TiO_2 planar heterojunction solar cells. J Renew Sustain Energy 7:043105

Wu X, Trinh MT, Niesner D, Zhu H, Norman Z, Owen JS, Yaffe O, Kudisch BJ, Zhu XY (2015d) Trap states in lead iodide perovskites. J Am Chem Soc 137(5):2089–2096

Wu Q, Zhou W, Liu Q, Zhou P, Chen T, Lu Y, Qiao Q, Yang S (2016) Solution-processable ionic liquid as an independent or modifying electron transport layer for high-efficiency perovskite solar cells. ACS Appl Mater Interfaces 8:34464–34473

Wu Y, Xie F, Chen H, Yang X, Su H, Cai M, Zhou Z, Noda T, Han L (2017) Thermally stable $MAPbI_3$ perovskite solar cells with efficiency of 19.19% and area over 1 cm^2 achieved by additive engineering. Adv Mater 29:1701073

Xiao MD, Gao M, Huang FZ, Pascoe AR, Qin TS, Cheng YB, Bach U, Spiccia L (2016) Efficient perovskite solar cells employing inorganic interlayers. Chemnanomat 2:182–188

Xiao YQ, Cheng N, Kondamareddy KK, Wang CL, Liu P, Guo SS, Zhao XZ (2017) W-doped TiO_2 mesoporous electron transport layer for efficient hole transport material free perovskite solar cells employing carbon counter electrodes. J Power Sources 342:489–494

Xie FX, Chen CC, Wu YZ, Li X, Cai ML, Liu X, Yang XD, Han LY (2017) Vertical recrystallization for highly efficient and stable formamidinium-based inverted-structure perovskite solar cells. Energy Environ Sci 10:1942–1949

Xing G, Mathews N, Sun S, Lim SS, Lam YM, Grätzel M, Mhaisalkar S, Sum TC (2013) Long-range balanced electron- and hole-transport lengths in organic-inorganic $CH_3NH_3PbI_3$. Science 342(6156):344–347

Xing Y, Sun C, Yip HL, Bazan GC, Huang F, Cao Y (2016) New fullerene design enables efficient passivation of surface traps in high performance *p-i-n* heterojunction perovskite solar cells. Nano Energy 26:7–15

Xu X, Zhang H, Cao K, Cui J, Lu J, Zeng X, Shen Y, Wang M (2014) Lead methylammonium triiodide perovskite-based solar cells: an interfacial charge-transfer investigation. Chem Sus Chem 7:3088–3094

Xu X, Liu Z, Zuo Z, Zhang M, Zhao Z, Shen Y, Zhou H, Chen Q, Yang Y, Wang M (2015a) Hole selective NiO contact for efficient perovskite solar cells with carbon electrode. Nano Lett 15:2402–2408

Xu X, Zhang H, Shi J, Dong J, Luo Y, Li D, Meng Q (2015b) Highly efficient planar perovskite solar cells with a TiO_2/ZnO electron transport bilayer. J Mater Chem A 3:19288–19293

Xu L, Wan F, Rong Y, Chen H, He S, Xu X, Liu G, Han H, Yuan Y, Yang J, Gao Y, Yang B, Zhou C (2017) Stable monolithic hole-conductor-free perovskite solar cells using TiO_2 nanoparticle binding carbon films. Org Electron 45:131–138

Yan K, Wei Z, Li J, Chen H, Yi Y, Zheng X, Long X, Wang Z, Wang J, Xu J, Yang S (2015) High-performance graphene-based hole conductor-free perovskite solar cells: Schottky junction enhanced hole extraction and electron blocking. Small 11:2269–2274

Yang YY, Xiao JY, Wei HY, Zhu LF, Li DM, Luo YH, Wu HJ, Meng QB (2014) An all-carbon counter electrode for highly efficient hole-conductor-free organo-metal perovskite solar cells. RSC Adv 4:52825–52830

Yang WS, Noh JH, Jeon NJ, Kim YC, Ryu S, Seo J, Seok SI (2015a) High-performance photovoltaic perovskite layers fabricated through intramolecular exchange. Science 348(6240):1234–1237

Yang Y, Ri K, Mei AY, Liu LF, Hu M, Liu TF, Li X, Han HW (2015b) The size effect of TiO_2 nanoparticles on a printable mesoscopic perovskite solar cell. J Mater Chem A 3:9103–9107

Yang IS, You JS, Do Sung S, Chung CW, Kim J, Lee WI (2016a) Novel spherical TiO_2 aggregates with diameter of 100 nm for efficient mesoscopic perovskite solar cells. Nano Energy 20:272–282

Yang D, Yang R, Ren X, Zhu X, Yang Z, Li C, Liu SF (2016b) Hysteresis-suppressed high-efficiency flexible perovskite solar cells using solid-state ionic-liquids for effective electron transport. Adv Mater 28:5206–5213

Yang D, Zhou X, Yang R, Yang Z, Yu W, Wang X, Li C, Liu SF, Chang RPH (2016c) Surface optimization to eliminate hysteresis for record efficiency planar perovskite solar cells. Energy Environ Sci 9:3071–3078

Yang Z, Rajagopal A, Chueh C-C, Jo SB, Liu B, Zhao T, Jen AKY (2016d) Stable low-bandgap Pb–Sn binary perovskites for tandem solar cells. Adv Mater 28:8990–8997

Yang D, Zhou X, Yang R, Yang Z, Yu W, Wang X, Li C, Liu S, Chang RPH (2016e) Surface optimization to eliminate hysteresis for record efficiency planar perovskite solar cells. Energy Environ Sci 9(10):3071–3078

Yang YL, Chen HN, Zheng XL, Meng XY, Zhang T, Hu C, Bai Y, Xiao S, Yang SH (2017) Ultrasound-spray deposition of multi-walled carbon nanotubes on NiO nanoparticles-embedded perovskite layers for high-performance carbon-based perovskite solar cells. Nano Energy 42:322–333

Yang Y, Wu J, Wang X, Guo Q, Liu X, Sun W, Wei Y, Huang Y, Lan Z, Huang M, Lin J, Chen H, Wei Z (2020) Suppressing vacancy defects and grain boundaries via Ostwald Ripening for high-performance and stable perovskite solar cells. Adv Mater 32(7):1904347

Ye S, Sun W, Li Y, Yan W, Peng H, Bian Z, Liu Z, Huang C (2015) CuSCN-based inverted planar perovskite solar cell with an average PCE of 15.6%, Nano Lett 15:3723–3728

Yeo JS, Kang R, Lee S, Jeon YJ, Myoung N, Leek CL, Kim DY, Yun JM, Seo YH, Kim SS, Na SI (2015) Highly efficient and stable planar perovskite solar cells with reduced graphene oxide nanosheets as electrode interlayer. Nano Energy 12:96–104

Yi C, Luo J, Meloni S, Boziki A, Ashari-Astani N, Grätzel C, Zakeeruddin SM, Röthlisberger U, Grätzel M (2016) Entropic stabilization of mixed A-cation ABX_3 metal halide perovskites for high performance perovskite solar cells. Energy Environ Sci 9:656–662

Yin XT, Que MD, Xing YL, Que WX (2015) High efficiency hysteresis-less inverted planar heterojunction perovskite solar cells with a solution-derived NiO_x hole contact layer. J Mater Chem A 3:24495–24503

Yin X, Chen P, Que M, Xing Y, Que W, Niu C, Shao J (2016) Highly efficient flexible perovskite solar cells using solution-derived NiO*x* hole contacts. ACS Nano 10:3630–3636

Yoshikawa K, Yoshida W, Irie T, Kawasaki H, Konishi K, Ishibashi H, Asatani T, Adachi D, Kanematsu M, Uzu H, Yamamoto K (2017) Exceeding conversion efficiency of 26% by heterojunction interdigitated back contact solar cell with thin film Si technology. Sol Energy Mater Sol 173:37–42

You J, Hong Z, Yang Y, Chen Q, Cai M, Song T-B, Chen C-C, Lu S, Liu Y, Zhou H, Yang Y (2014) Low-temperature solution-processed perovskite solar cells with high efficiency and flexibility. ACS Nano 8:1674–1680

You P, Liu Z, Tai Q, Liu S, Yan F (2015) Efficient semi transparent perovskite solar cells with graphene electrodes. Adv Mater 27:3632–3638

You J, Meng L, Song TB, Guo TF, Yang YM, Chang WH, Hong Z, Chen H, Zhou H, Chen Q, Liu Y, De Marco N, Yang Y (2016) Improved air stability of perovskite solar cells via solution-processed metal oxide transport layers. Nat Nanotechnol 11:75–81

Yu W, Li F, Wang H, Alarousu E, Chen Y, Lin B, Wang L, Hedhili MN, Li Y, Wu K, Wang X, Mohammed OF, Wu T (2016a) Ultrathin Cu_2O as an efficient inorganic hole transporting material for perovskite solar cells. Nanoscale 8:6173–6179

Yu X, Chen S, Yan K, Cai X, Hu H, Peng M, Chen B, Dong B, Gao X, Zou D (2016b) Enhanced photovoltaic performance of perovskite solar cells with mesoporous SiO_2 scaffolds. J Power Sources 325:534–540

Yu Y, Wang C, Grice CR, Shrestha N, Chen J, Zhao D, Liao W. Cimaroli AJ, Roland PJ, Ellingson RJ (2016) Improving the performance of formamidinium and cesium lead triiodide perovskite solar cells using lead thiocyanate additives. ChemSusChem 9:3288–3297

Yuan Y, Huang J (2016) Ion migration in organometal trihalide perovskite and its impact on photovoltaic efficiency and stability. Acc Chem Res 49(2):286–293

Yue GQ, Chen D, Wang P, Zhang J, Hu ZY, Zhu YJ (2016) Low-temperature prepared carbon electrodes for hole-conductor-free mesoscopic perovskite solar cells. Electrochim Acta 218:84–90

Yue SZ, Liu K, Xu R, Li MC, Azam M, Ren K, Liu J, Sun Y, Wang ZJ, Cao DW, Yan XH, Qu SC, Lei Y, Wang ZG (2017) Efficacious engineering on charge extraction for realizing highly efficient perovskite solar cells. Energy Environ Sci 10:2570–2578

Zhang F, Yang X, Wang H, Cheng M, Zhao J, Sun L (2014) Structure engineering of hole-conductor free perovskite-based solar cells with low-temperature-processed commercial carbon paste as cathode. ACS Appl Mater Interfaces 6:16140–16146

Zhang LJ, Liu TF, Liu LF, Hu M, Yang Y, Mei AY, Han HW (2015a) The effect of carbon counter electrodes on fully printable mesoscopic perovskite solar cells. J Mater Chem A 3:9165–9170

Zhang F, Yang X, Cheng M, Li J, Wang W, Wang H, Sun L (2015b) Engineering of hole-selective contact for low temperature-processed carbon counter electrode-based perovskite solar cells. J Mater Chem A 3:24272–24280

Zhang J, Juárez-Pérez EJ, Mora-Seró I, Viana B, Pauporté T (2015c) Fast and low temperature growth of electron transport layers for efficient perovskite solar cells. J Mater Chem A 3:4909–4915

Zhang J, Shi C, Chen J, Ying C, Wu N, Wang M (2016a) Pyrolysis preparation of WO_3 thin films using ammonium metatungstate DMF/water solution for efficient compact layers in planar perovskite solar cells. J Semicond 37:033002

Zhang NN, Guo YJ, Yin X, He M, Zou XP (2016b) Spongy carbon film deposited on a separated substrate as counter electrode for perovskite-based solar cell. Mater Lett 182:248–252

Zhang FG, Yang XC, Cheng M, Wang WH, Sun LC (2016c) Boosting the efficiency and the stability of low-cost perovskite solar cells by using CuPc nanorods as hole transport material and carbon as counter electrode. Nano Energy 20:108–116

Zhang CX, Luo YD, Chen XH, Chen YW, Sun Z, Huang SM (2016d) Effective improvement of the photovoltaic performance of carbon-based perovskite solar cells by additional solvents. Nano-Micro Lett 8:347–357

Zhang LQ, Yang XL, Jiang Q, Wang PY, Yin ZG, Zhang XW, Tan HR, Yang Y, Wei MY, Sutherland BR, Sargent EH, You JB (2017a) Ultra-bright and highly efficient inorganic based perovskite light-emitting diodes. Nat Commun 8:15640

Zhang J, Hultqvist A, Zhang T, Jiang L, Ruan C, Yang L, Cheng Y, Edoff M, Johansson EMJ (2017b) Al_2O_3 underlayer prepared by atomic layer deposition for efficient perovskite solar cells. Chemsuschem 10:3810–3817

Zhang M, Yun JS, Ma Q, Zheng J, Lau CFJ, Deng X, Kim J, Kim D, Seidel J, Green MA (2017c) High-efficiency rubidium-incorporated perovskite solar cells by gas quenching. ACS Energy Lett 2:438–444

Zhao K, Munir R, Yan B, Yang Y, Kim T, Amassian A (2015) Solution-processed inorganic copper (I) thiocyanate (CuSCN) hole transporting layers for efficient *p-i-n* perovskite solar cells. J Mater Chem A 3:20554–20559

Zhao DW, Yu Y, Wang CL, Liao WQ, Shrestha N, Grice CR, Cimaroli AJ, Guan L, Ellingson RJ, Zhu K, Zhao XZ, Xiong RG, Yan YF (2017) Low-bandgap mixed tin-lead iodide perovskite absorbers with long carrier lifetimes for all-perovskite tandem solar cells. Nat. Energy 2(4):17018

Zheng X, Wu C, Jha SK, Li Z, Zhu K, Priya S (2016) Improved phase stability of formamidinium lead triiodide perovskite by strain relaxation. ACS Energy Lett 1:1014–1020

Zheng X, Chen H, Li Q, Yang Y, Wei Z, Bai Y, Qiu Y, Zhou D, Wong KS, Yang S (2017) Boron doping of multiwalled carbon nanotubes significantly enhances hole extraction in carbon-based perovskite solar cells. Nano Lett 17:2496–2505

Zhou HP, Hsu WC, Duan HS, Bob B, Yang WB, Song TB, Hsu CJ, Yang Y (2013) CZTS nanocrystals: a promising approach for next generation thin film photovoltaics. Energy Environ Sci 6:2822–2838

Zhou H, Shi Y, Dong Q, Zhang H, Xing Y, Wang K, Du Y, Ma T (2014a) Hole-conductor-free, metal-electrode-free $TiO_2/CH_3NH_3PbI_3$ heterojunction solar cells based on a low-temperature carbon electrode. J Phys Chem Lett 5:3241–3246

Zhou H, Chen Q, Li G, Luo S, Song TB, Duan HS, Hong Z, You J, Liu Y, Yang Y (2014b) Interface engineering of highly efficient perovskite solar cells. Science 345:542–546

Zhou H, Shi Y, Wang K, Dong Q, Bai X, Xing Y, Du Y, Ma T (2015) Low-temperature processed and carbon-based $ZnO/CH_3NH_3PbI_3/C$ planar heterojunction perovskite solar cells. J Phys Chem C 119:4600–4605

Zhu Z, Bai Y, Zhang T, Liu Z, Long X, Wei Z, Wang Z, Zhang L, Wang J, Yan F, Yang S (2014) High-performance hole-extraction layer of sol–gel-processed NiO nanocrystals for inverted planar perovskite solar cells. Angew Chem Int Ed 126:12571–12575

Zhu Z, Zheng X, Bai Y, Zhang T, Wang Z, Xiao S, Yang S (2015) Mesoporous SnO_2 single crystals as an effective electron collector for perovskite solar cells. Phys Chem Chem Phys 17:18265–18268

Zhu Z, Zhao D, Chueh C-C, Shi X, Li Z, Jen AKY (2018) Highly efficient and stable perovskite solar cells enabled by all-crosslinked charge-transporting layers. Joule 2:168–183

Zuo C, Ding L (2015) Solution-processed Cu_2O and CuO as hole transport materials for efficient perovskite solar cells. Small 11:5528–5532

Zuo CT, Bolink HJ, Han HW, Huang JS, Cahen D, Ding LM (2016) Advances in perovskite solar cells. Adv Sci 3(7):1500324